Near-Infrared Integral Field Spectroscopy of RW Aurigae A

A thesis in fulfilment of the requirements for the degree

Master of Science of Experimental Physics
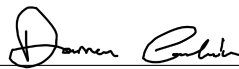
in the

Author:

Darren Cashin

Supervisor:

Dr. Emma Whelan

Preface

I declare that this thesis is my own work and has not been submitted in any form for another degree or diploma at any university or other institution of tertiary education.

Information derived from the published or unpublished work of others has been acknowledged in the text and a list of references is given.

Darren Cashin

Maynooth University

August 17, 2022

Acknowledgement

"If you solve one problem every day, you soon won't have many problems to solve."

- James Murphy, Maynooth University (2021).

Summary

Near-Infrared observations of the classical T Tauri star RW Aurigae A taken using the OH-Suppressing Infrared Spectrograph (OSIRIS) on the KECK telescope have been used to investigate the morphology & kinematics of the jet, finding an extended knot from the main body of the blue jet. Diagnostics have been performed, with the extinction being found to be higher than previous measurement ($A_v = 4.6$). The jets' mass-loss rates have been found to be 1.022 $\times 10^{-9}$ $M_\odot$/year and 1.544 $\times 10^{-9}$ $M_\odot$/year for the blue and red jet, respectively. The mass accretion rate has been measured to be 8.93 $\times 10^{-9}$ $M_\odot$/year using the Brγ emission line, having determined that it is not a constituent of the jet. The wiggle for the RW Aur jet has been fit with a precession and orbital model, both pointing to a brown dwarf companion with mass between 0.07 — 0.23 $M_\odot$ similar to independently derived results for RW Aur A and for other protostellar systems where wiggling has been used.

Contents

List of Figures

List of Tables

Table of Accronyms

BC .... Broad Component

CTTS .... Classical T Tauri Star

ESO ...... European Space Agency

FWHM ... Full Width Half Max

GMC ..... Giant Molecular Cloud

HVC ..... High Velocity Component

IFS .... Integral Field Spectroscopy

LVC ...... Low Velocity Component

MHD ..... Magnetohydrodynamics

NC .... Narrow Component

NIR ...... Near-Infrared

OSIRIS ... OH Suppressing Infra-red Imaging Spectrograph

PVD ..... Position Velocity Diagram

TTS ...... T Tauri Star

VLT ...... Very Large Telescope

WTTS .... Weak T Tauri Star

1　Introduction

The interstellar gas, which is the building block of stars, is composed of neutral atomic hydrogen and various other elements. This gas is extremely sparse with a mean density of 1 atom cm^{-3}. However, this gas is *not* evenly distributed, with a tendency for the gas to form gas clouds with an average radius of 7.5 pc, a mass of $1000 M_\odot$, and with a mean density of 10 atoms cm^{-3}.

The transition from interstellar gas cloud to star is shrouded in uncertainty. It is known for certain that our sun is kept in equilibrium between the outward forces of the nuclear reactions within its core and its own gravity, keeping it together. It is therefore reasonable to assume that the forces of gravity that works on the star is that which created them in the first place. For the gas to collapse it requires that the gravitational energy of the gas is larger than the gas' thermal energy,

$$|E_g| > E_{th} \tag{1.1}$$

assuming a spherical core of mass M, temperature T and radius R is given by:

$$\frac{3}{5}\frac{GM}{R} > \frac{3}{2}\frac{M}{\mu m_H}kT \tag{1.2}$$

where all symbols carry their usual meaning. This inequality is usually referenced in terms of the Jeans mass M_J; the gravitational collapse of the gas cloud begins when the core mass M is greater than the Jeans mass.

$$M > M_J = \left(\frac{3}{4\pi\rho}\right)^{\frac{1}{2}} \left(\frac{3kT}{2G\mu m_H}\right)^{\frac{3}{2}} \simeq 6M_\odot \left(\frac{T^3}{n}\right) \tag{1.3}$$

here n is the number density $n = \rho/\mu m_H$. In the case of a normal gas cloud of $T = 10$ K and $n \geq 50$ cm^{-3}, it is found we have an M_J of $\simeq 100$ $M_\odot$ and a free fall time

$t_{\text{ff}} \simeq 10^5$ years. Once gravitational collapse has occurred, the protostar goes through a plethora of changes before becoming a main sequence star (Figure 1.1). Due to its proximity to us, the Taurus Auriga molecular cloud is the subject of intensive studies. This relative closeness makes it a perfect laboratory to observe the star formation process, with hundreds of protostars (Luhman et al. (2009) & Kenyon et al. (2008)) in various stages of their evolution (Kenyon et al. (1994), Park & Kenyon (2002) and references there in); these evolutionary stages are described below.

Class 0: Immediately after gravitational collapse has occurred, the protostar is considered a Class 0 object, with the central protostar being surrounded by a dense envelope of gas and dust (Tobin et al. 2015). It is here the formation of the circumstellar disk is thought to begin. In Class 0 sources, the mass of the protostar is lower than that of its surrounding envelope, given by: $M_\star < M_{\text{envelope}}$ (Andre et al. 1993), with a cold blackbody spectrum of $\sim 10 - 30$ K. In the case of Class 0 stars, they commonly drive powerful bipolar outflows (Erkal, Nisini, Coffey, Bacciotti, Hartigan, Antoniucci, Giannini, Eislöffel & Manara 2021), Tafalla et al. (2000) and references there in). During their relatively short lifespan of $\sim 10^4$ years (Andre et al. 1993), Class 0 objects undergo systemic changes linked to the accumulation of material. Compared to later stages of their evolutionary trees, Class 0 objects are much less well understood when compared to their descendants (due to their embedded nature (Boss & Yorke 1990)).

Class I: Class I protostars are ones that are coming to the end of the stage of their development in which the majority of the mass accretion has occurred (Johns-Krull et al. (2009) and references there in). Extensive surveys of 52 Class I objects in a variety of star forming regions by Doppmann et al. (2005) bolster this idea of an earlier evolutionary object, in which the later evolution Class II object is born (Johns-Krull et al. (2009) and Prato et al. (2009)). As a general rule, the outflows associated with Class I objects are generally less powerful compared to Class 0 outflows of a similar

luminosity (Bontemps et al. (1996) and Gargaud (2011)).

Class II: Class II objects are similar to that of Class I, with a few noticeable differences; The rotation of Class II objects is noticeably slower (Covey et al. 2006), possibly caused by magnetic braking caused by the disk itself (Montmerle et al. 2000) or accretion-driven winds causing the change in angular momentum (Prato et al. (2009), Gargaud (2011) and Matt & Pudritz (2005)).

The mass accretion has now slowed dramatically compared to that of Class 0 ($\sim 10^{-6}$ — 10^{-5} M$_\odot$/year) and Class I ($\sim 10^{-7}$ — 10^{-6} M$_\odot$/year). It is in this stage when planet formation is thought to occur, as there is still enough material in the circumstellar disk to facilitate planet formation (Cazzoletti et al. (2019) and Gargaud (2011)) and it is where Classical T Tauri Stars lie in their evolutionary journey.

1.1   Physical Characteristics of T Tauri Stars

T Tauri stars (TTS) are low-mass pre-main sequence late-type stars (heated through gravitational contraction and having not yet begun to burn at their cores), TTS have two main classifications: Classical T Tauri stars (CTTS) and Weak Emission T Tauri stars (WTTS). CTTS have a K0 or later spectral type, and have an equivalent Hα line width of greater than 10 Å. CTTSs show excess IR emission from circumstellar discs and excess UV and optical emission from the accretion of disc material. Once a CTTS has lost its disk (due to accretion or other mechanisms) and accretion no longer occurs, it is considered a WTTS (Johnstone et al. (2013) and Grankin (2016)). TTS have two distinguishing features compared to other stars, an emission line spectrum and their irregular variabilities (Edwards et al. 1994). In comparison to a standard star, which is composed of absorption lines such as the Fraunhofer lines (that we see in the Sun's spectrum) in TTS we observe emission of elements such as iron and hydrogen which allow us to make calculations on the characteristics of the star. Although most
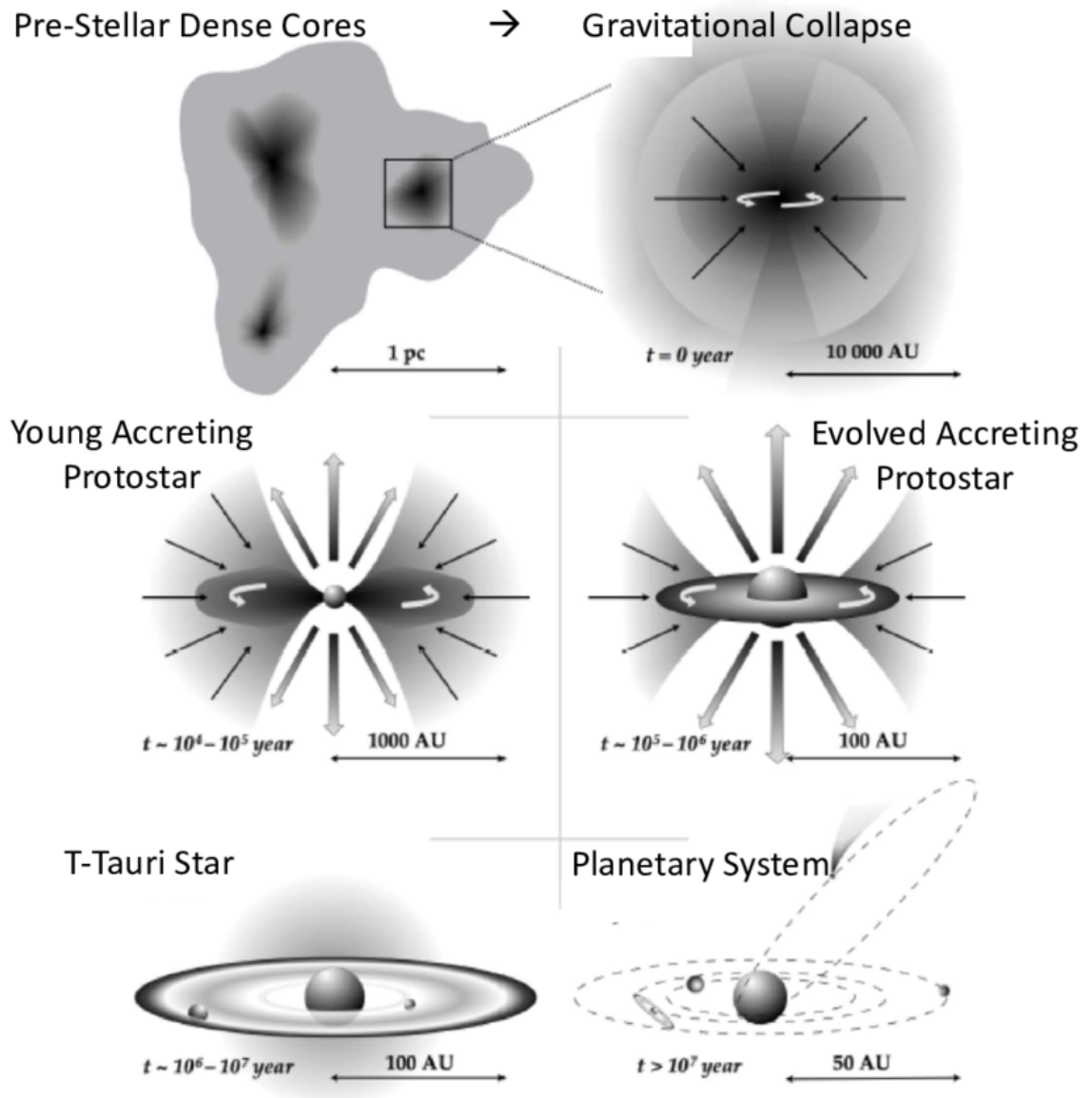
Figure 1.1: Evolutionary stages for the formation of low-mass stars (Colzi (2021) and references therein). The young accreting protostar is considered a Class 0 object, with the evolved accreting protostar being a Class I and finally the T Tauri star being the Class II.

stars display a variability, these are generally periodic in nature. Whereas in TTS, the periodicity is often irregular.TTS are dwarf class stars with G, K and M spectral types and lie above the main sequence. On the Hertzsprung-Russell diagram, however, they are scattered in position despite their masses being fairly uniform. Reviews of the properties of CTTS have shown evidence that typically their mass lies in the range of 0.5-1.5$M_\odot$ (Telleschi et al. (2007), Kuhi (1966) and Herbig (1967)). Estimations of the effective temperature of a number of TTS show that they lie within 3×10^3 and 5×10^3 K (Grankin (2016), Kitamura et al. (2002) and Herbig (1962)). This is in agreement with the theoretical models of newly formed stars with similar masses (Bertout et al. (2007) and Glasby (1974)).

1.2   Mass Accretion in Classical T Tauri Stars

In CTTS, the accretion of material from the circumstellar disk onto the star typically lasts for a few million years. To gain key information regarding the disk structure and evolution, as well as planet formation and migration, studying the mass accretion rate ($\dot{M}$) is imperative. The structure of the disk itself is affected by the rate at which the mass flows onto the central protostar (Whelan et al. 2015), which in turn is determined by the rate of gravitational energy release (Alencar 2007). In Figure 1.2, a diagram demonstrating the accretion disk is shown, with the flow column highlighted.

If we regard the accretion disk to be a simple viscous disk, the rate material is removed from the disk is given by the mass accretion rate onto the central star. To account for the loss of angular momentum due to the accreting material, the disk itself must expand. The rate of angular momentum transfer and the accretion rate are proportional to the viscosity of the disk itself (Calvet et al. 2004). In a protoplanetary disk that has an evolving viscosity, one would expect for there to be a correlation between $\dot{M}$ and the mass of the disk itself (Hartmann et al. 1998), this correlation was found to be
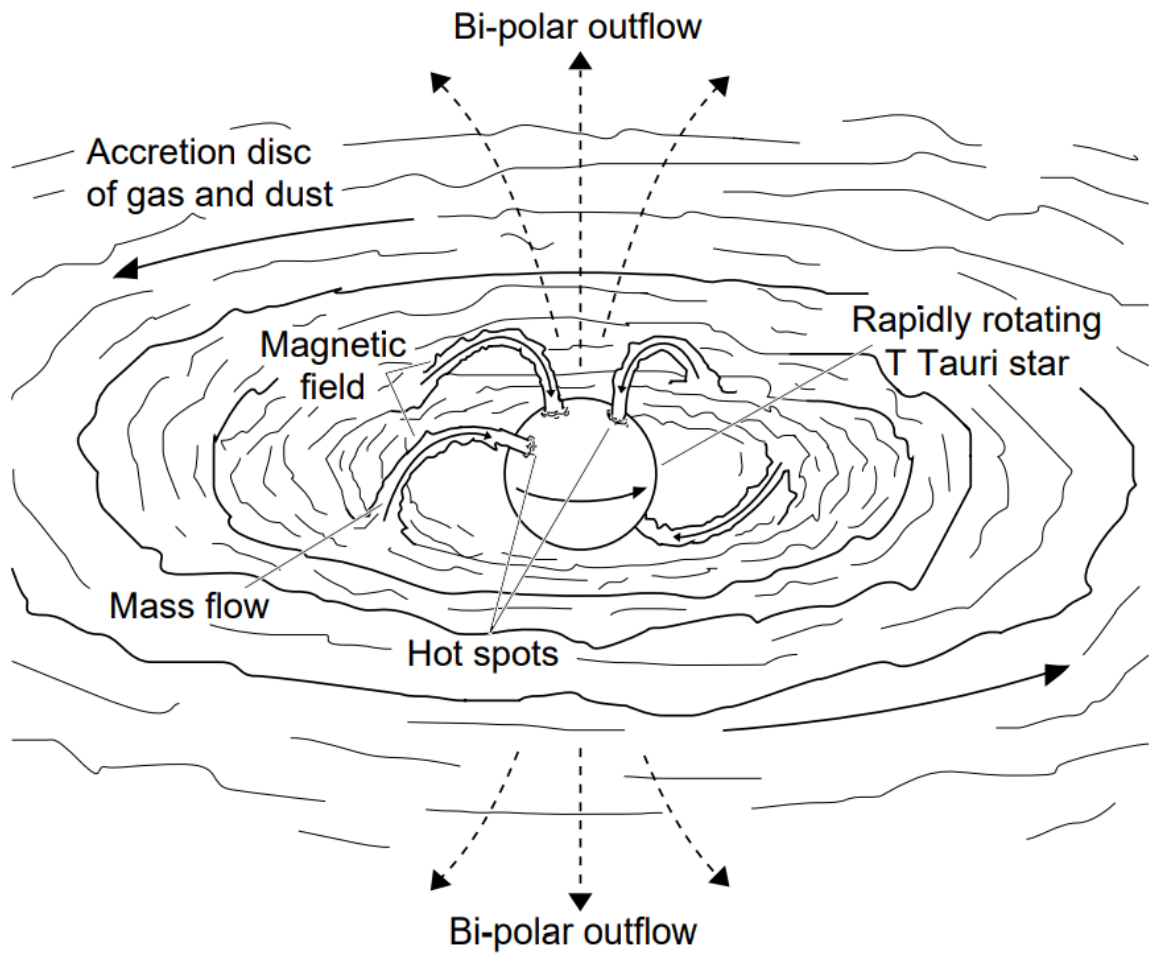
Figure 1.2: Diagram of a Classical T Tauri star (Percy (2011) and references therein).

statistically significant (under the assumption that the total disk mass is proportional to the disk dust mass) by Manara et al. (2016). The mass accretion phase typically lasts for ≤ 2.5 Myr (Mamajek (2009) and references therein), this time period is also thought to be the time period in which large planetesimals and giants planets first form (Lisse et al. (2022) and references there in).

1.3   Jets from Classical T Tauri Stars

Jets and outflows are frequently observed coming from young stars (Whelan et al. (2014) and Whelan (2014)); this raises the question of whether they are foundational to the star formation process, or, if they are simply a byproduct. Modern theory and observations make use of jets to explain a number of the outstanding issues observed in the star formation process (Frank et al. 2014). In a CTTS, it is thought jets are one of the main drivers in the loss of excess angular momentum, the efficiency, and the degree of collimation strongly favours magneto-hydrodynamical processes being involved in the ejection process (Nisini et al. (2018) and Dyda et al. (2015)). This outlet, for angular momentum, is used to explain the accretion rates that are maintained in the star formation process of protostars (Frank et al. 2014).

The opening angle of a jet is typically around a few degrees, while the typical lengths of jets can range from a localised jet with lengths of a few hundred au to jets that extend out several hundred parsecs (Reipurth & Bally 2001). The width of a jet increases with distance from the source, however, the jet stays within 3-5 times the FWHM of the local jet. The timescales of these jets range from 5-10 years for distances less than 1000 au and for larger scales between $10^2 - 10^3$ years. Jets are highly supersonic in nature with $v_{\mathrm{jet}}/c_{\mathrm{s}} \sim 20$-30, as a result, any small variations in the velocity of the jet generates a shock front in the beam that heats and excites the gas (Bacciotti 2005). Angular momentum from the disk is transferred by the outflow and jet driving regions

via magnetic fields that are coupled with neutral gas in the environment.

In protostellar jets and outflows, the high velocity (HVC) and low velocity components (LVC) originate from different regions. The LVC outflows are driven by the outer region of the circumstellar disk, while, the HVC are driven near an inner edge of the disk and are associated with collimated micro-jets (Hartigan & Morse 2007). The LVC spectral line profile can be described as a combination of two Gaussian profiles (a "narrow component," NC, and a "broad component," BC) (Whelan et al. 2021).

In the context of the driving mechanism of protostellar jets, the central debate is between two main models; one where winds arise close to the radius of magnetospherical truncation on the disk ($\leq$ 0.1 au) 'X-Wind' and the other where winds arise over a broad range of radii in the disk, from 0.1 to 10 au, called 'Disk-Winds'. These winds are not mutually exclusive, with both being driven magnetocentrifugally from open field lines anchored on rapidly rotating circumstellar disks (Fang et al. (2018) and Shang et al. (2007)). In disk wind models, it is predicted that most of the mass is lost within a few au from the central star (Pelletier & Pudritz 1992). This is supported by measurements of the BC and NC of a number of samples finding that the BC has a larger $\dot{M}_{wind}/\dot{M}_{acc}$ than the NC (Fang et al. 2018).

Magnetohydrodynamic (MHD) simulations of an axisymmetric jets formation by Fendt (2009) demonstrated quantitatively that the magnetic field has a defining impact on the process in which the jet is formed via providing a central pressure - magnetically, providing angular momentum and additional magnetic flux in the jet's launching region. If we consider the typical case of an inclined magnetic field, the magnetosphere disturbs the outflow, triggering an *observable* time variation in the outflow rate! For Class 0 — II objects to produce strong jets such as those observed, it is required that there are collimating disk winds with a reasonable mass load. Using spectro-astrometry Whelan et al. (2021) demonstrated for the first time, in the case of RU Lupi, that the NC is

tracing a wide angled MHD disk wind, ruling out a photoevaporative wind. This result
was supported by previous spectro-astrometric studies using CO emission. They note
that more observations are required to determine if this property is unique to RU Lupi
or is seen in other TTS.

In CTTS, such as DG Tau, their jets have structures resembling that of an onion,
such that each layer gets progressively faster the further in we observe it, with these
velocities reaching into the hundreds of kms^{-1}. In the optical wave band, the outer
layers are traced by molecular lines, such as H_2, with the inner layers typically being
traced by Hα and some forbidden lines, such as [OI] and [SII]. (Bacciotti et al. (2000),
Lavalley-Fouquet et al. (2000), Agra-Amboage et al. (2011), Günther (2013), Günther
et al. (2019)).

1.3.1   Knots and Wiggles

When images are taken, at a sufficient angular resolution, knots, and wiggles become
pronounced in nearly all jets. In the context of jets, knots are regions of high density in
comparison to their neighbouring regions, while wiggles are variations in the position of
the jet's centroid as it travels from its launching site. Knots and wiggles appear very
close to stars, in the case of RW Aurigae this is less than 20 au from the star itself. The
origin of a wiggle depends on the system itself; the first type of wiggling observed is due
to a precession in the jet caused by interactions of an unseen binary with the accretion
disk (Raga et al. 1993), with the second being orbital motion of the protostar that
drives the jet (Masciadri & Raga 2002), or, a combination of both (Lee et al. (2010)
and Raga et al. (2009)).

Measurements of the wiggling of DO Tau's asymmetric jet by Erkal, Dougados, Coffey,
Cabrit, Bacciotti, Garcia-Lopez, Fedele & Chrysostomou (2021), demonstrate the ability
to not only determine scenarios for the system (the origin of the jet being an unseen

companion), it also allows further constraining on the *possible* makeup of the system, namely, the possibility of the wiggling being caused by an inclined massive companion (6 — 12 M_{Jup}) or the outflow itself causing a warp in the accretion disk and thus a precession of the disk rotation axis and associated jet axis.

1.3.2   Shocks in Jets

In protostellar jets, there are two types of shocks observed. The first observed is a jump shock or J-type shock which are formed in regions with a weak magnetic field allowing for changes to occur suddenly. The front of the shock region is followed by a distinct cooling region. The other type of shock is a continuous or C-type shock. These are found in regions with higher magnetic fields, opposed to J-type shocks the ions are gradually heated (Buckle et al. 1999).

1.4   RW Aurigae

RW Aur A (HD 240764) is an extremely bright CTTS (V_{max} = 10.1 mag (Herbig & Bell 1988)) with mass of $1.3M_\odot \pm 0.2M_\odot$ (Woitas et al. (2001) and White & Ghez (2001)) located in the star forming region of Taurus-Auriga, it is often quoted as a triple system with component A separated by 1.4" from B and C (Alencar et al. 2005). However, later observations were unable to detect component C, this is despite the expected flux of C being well above the detecting limit, resulting in it being determined that RW Aur C was a false detection (Ghez et al. (1993) and White & Ghez (2001)).

RW Aur (Figure 1.3) is the photometric prototype star for CTTS (Percy 2011), with it being well established that there is large variation in the intensity and profile of emission and absorption features (Dodin et al. (2019), Petrov & Kozack (2007), Alencar et al. (2005), Grinin et al. (1985), Mundt & Giampapa (1982), Hartmann (1982), Appenzeller & Wolff (1982) and Gahm (1970)). Observations by López-Martín et al.

(2003) determined two modes of time variability; one irregular and asymmetric on the timescale of ≤3-10 years, with the other being more regular with a period of ∼20 years. RW Aur A has undergone two dimming events recently, the first one recorded by Rodriguez et al. (2013) had a dimming of ∼2 mags and a duration of ∼180 days, while the second dimming event occurred in 2014 with a dimming of ∼3 mags and lasted ∼ 1 year (Petrov et al. (2015) and Shenavrin et al. (2015)). RW Aur shows dramatic variability in its narrow and broad emission lines that can be explained by a single-lined spectroscopic binary (a brown dwarf companion) with a period of 2.77 days. (Gahm et al. (1999), Petrov et al. (2001) and Alencar et al. (2005)). Measurements taken using CHANDRA (Günther et al. 2018) measured the Fe abundance to be magnitudes above solar, which is in direct contrast to previous sub-solar measurements, as a result, they speculate that a breakup of planetesimals or a terrestrial plant could be the cause due to accretion onto the central star, further supporting the existence of an unseen companion close to RW Aur A. This is corroborated further by evidence of a Vesta sized planetesimal in the accretion disk (Lisse et al. 2022).

Using long-slit spectroscopy, Hirth et al. (1994) discovered that RW Aur A drives a spectacular asymmetric bipolar jet, with the asymmetry likely being caused by environmental effects and not due to the jet engine itself (Melnikov et al. 2009). The RW Aur jet is of particular interest due to it having one of the highest accretion rates ($\approx 2 - 10 \times 10^{-7}$ $M_\odot$/year) among CTTS, making it up to 100 times larger than a typical jet. Along with its high accretion rate, the RW Aur jet has a remarkably well-collimated appearance, with previous measurements of the opening angle in the optical band constraining it to be $\leq 6°$ (Woitas et al. (2002), Dougados et al. (2000), Hirth et al. (1994)). The spectacular nature of the RW Aur jet has made it the subject of intense observations over the years, observations of the [Fe II] spectra show highly blue and red shifted velocities demonstrating that this emission must be associated with fast flowing gas along the RW Aur outflow axis and the narrow line widths pointing to

low shock velocities (Davis et al. 2003). Despite the asymmetric nature of the RW Aur jet, measurements of the mass outflow rates for the blue and red lobe have found them to be similar, indicating that the asymmetries observed are likely caused by different environmental conditions (such as inhomogeneity in the local magnetic fields) and not by the central engine (which likely has a constraining symmetry on both sides of the system) (Melnikov et al. 2009).
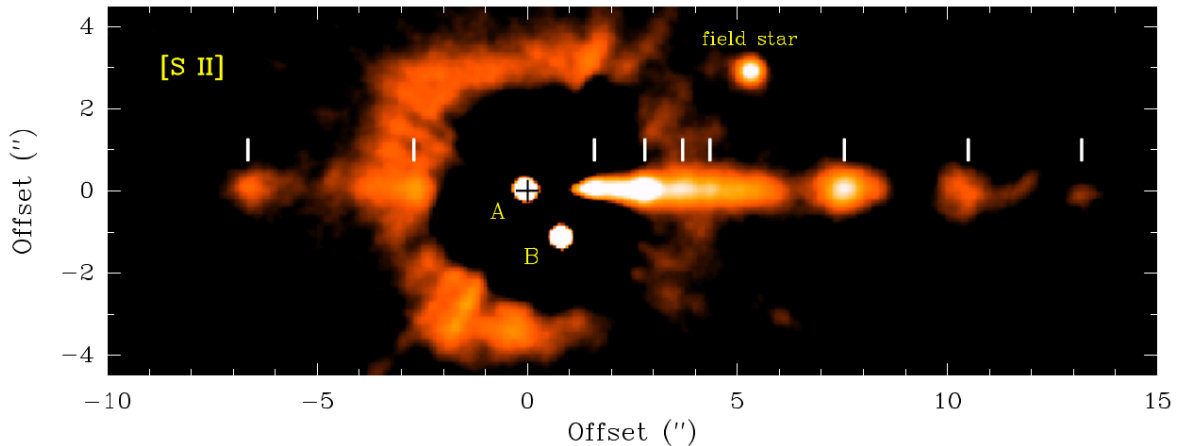
Figure 1.3: [S II] observations of the RW Aur system carried out at CFHT by Dougados et al. (2000).

Using the Subaru Telescope, Takami et al. (2020) performed long-term observations ($\sim$ 10 years) of the [Fe II] outflows, which, showed four knot ejections occurring over $\sim$15 years with an irregular interval of 2-6 years. In the blue-shifted jet they observed a strong and spatially extended emission with a peak velocity of -[200,170] kms^{-1} and a less blue-shifted wing covering -[100,0] kms^{-1}, localized to the stellar position. The red-shifted jet from RW Aur A shows a sharp drop toward the star from its peak located at Y $\sim$ -0.2" suggesting that its disk radius is smaller than 40 AU. Their position velocity diagram (PVD) was in agreement with the predicted PVD for an X-wind (Shenavrin et al. 2015). This is consistent with observations in the optical band of [OI], [SII] and [NII] which also demonstrated how the RW Aur A system can be interpreted

within the X-wind model (Liu & Shang 2012) (Figure 1.4). Evidence of a rotation signature is well studied in the RW Aur jet, HST observations found both the blue and red jet rotated in the same direction at a rate of between 5— 30 km/s (Woitas et al. 2005), this was confirmed by further HST observations (Coffey et al. 2004), however, later observations in the near-UV (Coffey et al. 2012) were unable to detect such a rotation signature. It should be noted, however, that this discrepancy may be caused by the variable nature of the RW Aur system itself. The Brγ line is considered to be of immense importance to the understanding of T Tauri systems (discussed further in §2.2). Using NIRSPEC on the KECK Interferometer, Eisner et al. (2007) presented spectroscopic observations of a sample of 11 TTS. They used the Brγ emission line to calculate L$_{Br\gamma}$ of RW Aur, finding it to be 1.5×10^{-4} L$_\odot$ and 3.1×10^{-4} L$_\odot$, with uncertainties between 5 and 20%. Using Eq. 2.2 and 2.3, they calculated L$_{acc}$ to be 0.42 L$_\odot$ and 1.02 L$_\odot$.

1.5 Summary

In this chapter I have the discussed the main features of CTTS including RW Aur. The main focus of this thesis will be centred on RW Aur A and its powerful bipolar outflow. The morphology of the jet will be examined to determine intrinsic characteristics of the jet and surrounding system such as the jets density, structure, the mass outfow rate, mass accretion rate and whether RW Aur A has a close, unseen companion.
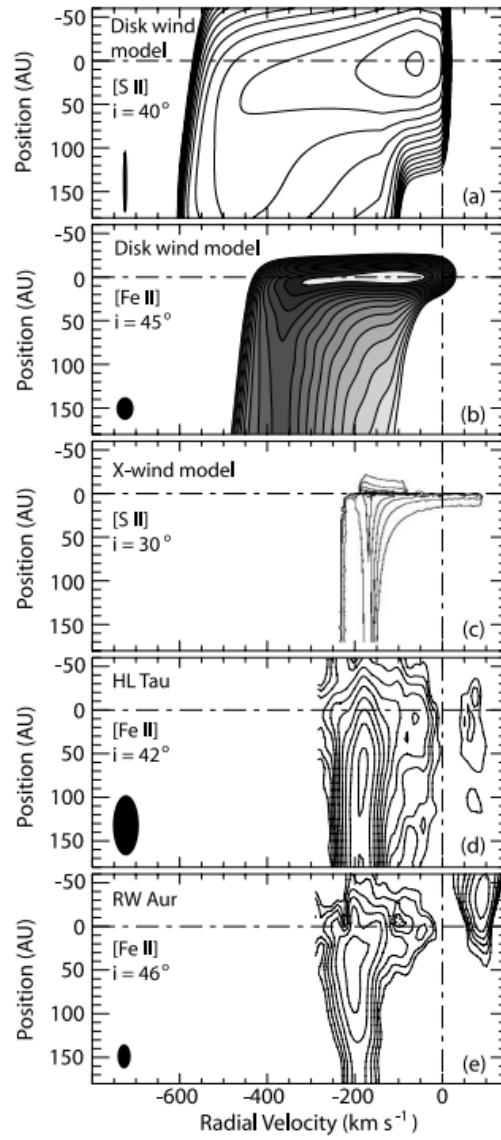
Figure 1.4: Comparison of model PVD's (a, b and c) with observations (d and e) created by Pyo et al. (2006) with references there in.

2 Near-IR Diagnostics Tools

This chapter outlines the near-IR (NIR) diagnostic tools available to us that can help us constrain the physical parameters (temperature, density, mass accretion rate, etc.) for RW Aur A and its jet. NIR observations are used due to their ability to trace close to the source without being impacted by extinction; originally, instruments such as SINFONI and OSIRIS combined integral field spectroscopy and adaptive optics (discussed later) in a way that were unrivalled when compared to optical telescopes.

2.1 [Fe II] Lines as a Diagnostic Tool

Forbidden lines are a result of transitions that occur which are not allowed by a particular set of selection rule (Bunker 2012). These selection rules are dependent on certain approximations, however, these approximations breakdown when we consider higher orders. An example is the electric dipole approximation preventing a set of transitions, but, the same transitions being allowed when considering electric quadrupoles. A comparison of the selection rules for dipole vs quadrupoles can be seen in Table 2.1. Selection rules (1) — (3) are rigorous in the absence of nuclear perturbations and two-quantum processes, while rules (4) — (6) are approximate selection rules, with lines produced by them usually not called "forbidden": (4) is only applicable when the configuration interaction is negligible, and (4) & (5) hold only for LS-. The "rigorous" rules can be violated when considering an electric dipole, but obeyed when considering higher-order poles such as electric quadrupole radiation (Garstang 1962).

In astrophysical systems, the probability of spontaneous decay exceeds that of the collisions, allowing forbidden transitions to occur. In a terrestrial environment, the electron density is too high, resulting in quenching of these forbidden transitions. [Fe II] is a well known and powerful diagnostic tool that can be used to determine numerous

properties about jets. It is possible to derive key parameters in protostellar outflows such as n_e, T_e and A_v by using line ratios of transitions with similar excitation energies and similar ground states. By looking at the energy levels diagram in Figure 2.1 we see that in the case of [Fe II], the 1.644 μm and 1.533 μm transitions are close in their excitation energies, with both residing in the same ground state. As a result, the ratio of these two lines is considered to be one of the best diagnostic tools for determining the electron density, as there is a weak dependence on the temperature (Pesenti et al. 2003). Critical densities for [Fe II] can be calculated using;

$$n_{cr}(i) = \frac{\Sigma_{j<i}A_{ij}}{\Sigma_{j\neq i}q_{ij}} \tag{2.1}$$

where A_{ij} denotes the Einstein spontaneous emission coefficients and q_{ij} denotes the collisional rate coefficients. When $n \gg n_{cr}$, the level population is given by the Boltzmann distribution. In the case where $n \ll n_{cr}$, the upper-level population is much smaller than that expected for a Boltzmann distribution, gas of such a low density only emits weakly (Pesenti et al. 2003).

The curves presented by Pesenti et al. (2003) were unavailable in a usable format for this research, as a result the line ratio curves were plotted using the python package `PyNeb` (Luridiana et al. 2013). The modelled curves for [Fe II] 1.533μm/1.644μm were in agreement between the 10^3 and 10^6 range, which, is of most concern. The modelled line ratios (for a range of lines) can be seen in Appendix A3.2, the curves are in agreement with the theoretical model within the region of low-temperature dependence and will be used to calculate density values from the line ratios.
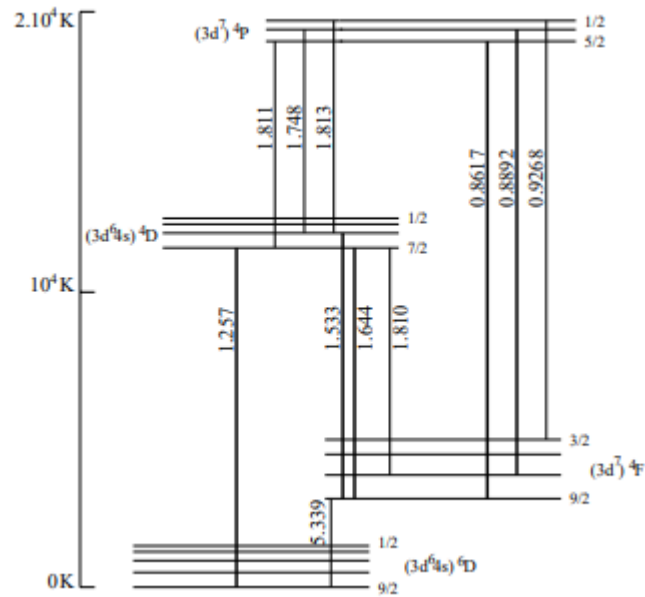
Figure 2.1: Energy level diagram of [Fe II] (Pesenti et al. 2003).

Atomic Spectra Selection Rules.			
—	Electric dipole	Magnetic Dipole	Electric quadrupole
(1)	$\Delta J = 0, \pm 1$	$\Delta J = 0, \pm 1$	$\Delta J = 0, \pm 1, \pm 2$
(2)	$\Delta M = 0, \pm 1$	$\Delta M = 0, \pm 1$	$\Delta M = 0, \pm 1, \pm 2$
(3)	Parity change	No parity change	No parity change
(4)	One electron jump	No electron jump	One or no electron jump
	$\Delta l = \pm 1$	$\Delta l = 0$	$\Delta l = \pm 2$
(5)	$\Delta S = 0$	$\Delta S = 0$	$\Delta S = 0$
(6)	$\Delta L = 0, \pm 1$	$\Delta L = 0$	$\Delta L = 0, \pm 1, \pm 2$

Table 2.1: Atomic Selection rules taken from Garstang (1962). L, S and J are the orbital, spin and total angular momentum respectively, M is the magnetic quantum number. The parity is $(-1)^{\Sigma l_i}$, where l_i is the azimuthal quantum number of the ith electron.

2.2   H and HeI as Diagnostic Tools

Despite early assumptions of hydrogen lines being associated only with stellar winds and mass loss, now it has come to be a sign post for accretion - this is due to the concept of magnetospherically guided accretion of the circumpolar disk material onto the forming star (Beck et al. (2010), Ghosh & Lamb (1979), Koenigl (1991) and Shu et al. (1994)) having gained acceptance due to its ability to explain the shapes of Paβ and Brγ emission lines. As a result, Brγ is considered a substitute for Hα as a signpost for circumstellar disk accretion in CTTS in the NIR (Najita et al. 1996) and, in some cases, a tracer for outflow activity (Whelan et al. 2004).

It is well established that it is possible to constrain the mass accretion of a source using measurements of Brackett and Paschen series emission lines, the equations for which are given by Eq. 2.2, Eq. 2.3 (originally by Muzerolle et al. (1998), with updated a, b parameters from Alcalá et al. (2017)), Eq. 2.4 (Gatti et al. (2008)) and Eq. 2.5 (Alcalá et al. (2014)). Bouvier & Appenzeller (n.d.) conducted a multi-epoch near-infrared spectroscopic survey of 16 actively accreting CTTS in the Taurus-Auriga star forming region, deriving line rations of the Brackett and Paschen series.

$$\text{Log}\left(\frac{L_{acc}}{L_\odot}\right) = (1.19 \pm 0.10) \times \text{Log}\left(\frac{L_{Br\gamma}}{L_\odot}\right) + (4.02 \pm 0.51) \tag{2.2}$$

$$\text{Log}\left(\frac{L_{acc}}{L_\odot}\right) = (1.14 \pm 0.16) \times \text{Log}\left(\frac{L_{Pa\beta}}{L_\odot}\right) + (3.15 \pm 0.58) \tag{2.3}$$

$$\text{Log}\left(\frac{L_{\text{acc}}}{L_\odot}\right) = 1.36 \times \text{Log}\left(\frac{L_{Pa\gamma}}{L_\odot}\right) + 4.1 \tag{2.4}$$

$$\dot{M}_{acc} \approx 1.25 \frac{L_{acc} R_\star}{G M_\star} \tag{2.5}$$

Along with H emission, HeI has now become a tool used to indicate the mass accretion

rates. A survey of 39 CTTS (Edwards et al. 2006) found HeI 1.083μm and Paγ line emission in 97% of the sample population, demonstrating that strong HeI emission can be used as an indicator for high accretion rates, while net absorption, probably due to a wind, is typical of low accretion rates. This demonstrates the unprecedented sensitivity that HeI has to the inner winds and magnetospheric accretion flows (Gatti et al. 2008).

2.2.1   Accretion Parameters

Using the mass accretion rate we can derive the fraction of the surface area covered by the accretion spot ($f_\star$) using the relation derived by Batalha et al. (2002), this relation can be seen in equation 2.6. Using models derived by Calvet & Gullbring (1998), it is possible to determine the energy flux carried by the accretion column into the shock region, ζ, given by equation 2.7. The hydrogen emission in these models arises from pre-shocked regions, which predicts the density given by equation 2.8. Finally, it is possible to measure the infall velocity using these models, which is given by equation 2.9 (Calvet & Gullbring (1998) and Vacca & Sandell (2011)).

$$f_\star = 0.49 \left(\frac{L_{acc}}{L_\odot} \right) + 0.01 \tag{2.6}$$

$$\zeta = 9.8 \times 10^{10} \left(\frac{\dot{M}}{10^{-8} M_\odot yr^{-1}} \right) \left(\frac{M}{0.5 M_\odot} \right) \left(\frac{R}{2 R_\odot} \right)^{-3} \left(\frac{f_\star}{0.01} \right)^{-1} \mathrm{erg\ cm^{-2} s^{-1}} \tag{2.7}$$

$$n_\mathrm{H} = 5.8 \times 10^{12} \left(\frac{\dot{M}}{10^{-8} M_\odot yr^{-1}} \right) \left(\frac{M}{0.5 M_\odot} \right)^{-0.5} \left(\frac{R}{2 R_\odot} \right)^{-1.5} \left(\frac{f_\star}{0.01} \right)^{-1} \mathrm{cm^{-3}} \tag{2.8}$$

$$\nu = 275 \left(\frac{M}{0.5 M_\odot} \right)^{0.5} \left(\frac{R}{2 R_\odot} \right)^{-0.5} \mathrm{km\ s^{-1}} \tag{2.9}$$

2.3   H2 Lines as a Diagnostic Tool

Molecular hydrogen (here after H_2) emission was first discovered around a young star by Beckwith et al. (1978) when they discovered the 1-0 S(1) line at 2.1218 μm in T Tau. H_2 2.12 μm ($v = $ 1-0S(1)) is a rotational vibrational transition of molecular hydrogen. There are a number of suggestions for the source of H_2 2.12 excitations. Below, the two most common arguments are outlined.

H_2 is a primary constituent of cool gas in the circumstellar environments of young stars, it is believed that these lines are collisionally excited in transiently heated, shocked gas in the 2000-3000K temperature range (Gredel 1994). Gredel (1994) studied a number of HH objects in the H- and K- bands, demonstrating that for these objects the population distribution is thermal, and can be well described by single excitation temperatures ranging from 2000-2700 K. Non-thermal excitation scenarios such as excitations in UV or X-ray heated gas were not observed. This is supported by Youngblood et al. (2018), who took measurements across the Orion Becklin-Neugebauer/ Kleinmann-Low explosive outflow, measuring the H_2 temperatures and column densities for a set of 13 near-IR H_2 rovibrational lines. They then modelled the radiative transfer of H_2 in the region with UV pumping models to look for signatures of H_2 fluorescence from HI Lyα pumping. Their model predicted a detectable Lyα signature in near-IR lines, however, such a source was not present in the outflow, resulting in them concluding that their data was consistent with shocks as the H_2 heating source.

H_2 at the low temperatures that we expect to find in the circumstellar environment, predominantly populates the ground vibrational level and leaves only low rotational excitation levels remaining, which are difficult to stimulate due to their lack of a dipole moment. Where we have a temperature that is high enough to cause the excitation of H_2 directly, the density is too high to detect H_2 noticeably and regions with a low

enough density to make H_2 detection possible don't have a high enough temperature (1000 K) to excite H_2 into its first vibrational state, making detection of thermally excited H_2 near impossible to detect (Bary et al. 2003).

Similar to [Fe II], by taking line ratios of H_2 it is possible to obtain physical parameters of the outflow. For example, the H_2 1–0 S(1)/2—1 S(1) ratio is sensitive to excitation mechanisms, whether that be UV excitation, X-Ray excitation or shocked gas. These models, unfortunately, have limited ability to be applied to circumstellar disks due to their inability to reliably distinguish between shocked and UV exited emission (Beck et al. (2008), Greene et al. (2010) and Gredel & Dalgarno (1995)).

2.3.1   H2 as a Tracer for Outflow Activity

In the NIR the jet shocked excited regions mainly cool through H_2 quadrupole transitions, therefore the bright rovibrational lines in that range represent the most suitable shock tracer, with the ability to evaluate the molecular hydrogen luminosity (L_{H_2}) of the outflow. Compared to HI (§2.2), 1-0S(1) traces very different excitation conditions, namely, a dense, molecular gas of relatively low excitation. Where HI is thought to trace the infall of material, H_2 traces the outflow (Davis et al. 2001).

Due to the rapid cooling, H_2 is more suitably compared to the CO lines, which only give a time integrated response (Smith et al. (2002) and Caratti o Garatti et al. (2006)). Caratti o Garatti et al. (2006) analysed 23 outflows driven by Class 0 and I sources. They found in $\sim$ 74% of the outflows, spots of ionized gas, which in some cases indicated the presence of embedded HH-like objects.

Wilking et al. (1990) observed 33 HH objects and suspected HH objects. They appear to demonstrate that in the case of R CrA and LkHα 234, 1-0S(1) emission appears to indicate the exact position of the blue shifted molecular gas in these bipolar outflows. However, these results were not entirely consistent with models using C-type and J-type

shocks. For the C-type shock models, beam-filling factors of 0.02-0.2 are required to match the observed 1-0S(1) line intensities. The J-type shock matched the 1-0S(1) line intensity, however the predicted ratio of 2-0S(1)/1-0S(1) is $\sim$3 times higher than what was observed.

By using H_2 2.122 μm emission as a tracer of jets and outflows, Davis et al. (2009) performed an analysis of the southern part of the Orion constellation, encompassing the Orion A and B Giant Molecular Clouds (GMCs). Their results indicate that regions of H_2 emission in jets and outflows are short-lived, fading much faster when compared to the timescales associated with CTTS and their outflows.

2.4   Summary

In this chapter I have discussed the main diagnostic tools available in the observed wavebands. Using [Fe II], H, HeI H_2 it is possible to determine various properties of the star, the disk and the jets itself along with their origins within the systems. This research however, focuses mainly on the [Fe II] and H emission lines.

3 Observations, Data Reduction & Analysis

In this chapter, the observations taken using the OH-Suppressing Infra-Red Imaging Spectrograph (OSIRIS) instrument on the KECK telescope, the processes used to reduce and flux calibrate the data, along with the accuracy of the fitting routines are discussed.

3.1 Integral Field Spectroscopy

In standard astronomical observations, we typically have a two-dimensional image of either two spatial dimensions or one spatial and one spectral dimension, whereas, in integral field spectroscopy (IFS) all three dimensions are observed. There are a number of ways that this can be done (Bacon et al. (1995), Weitzel et al. (1996) and Arribas et al. (1998)). In the case of OSIRIS, lenslet based IFS are of the most interest. The OSIRIS instrument is an IFS on the W.M Keck II telescope, located near the summit of Mauna Kea, Hawaii. OSIRIS utilises lenslet-based IFS to provide a spectral resolution of 3900 from 1 - 2.5μm, offering a range of narrow and broad-band filters of varying pixel scales and fields of view (FOV). Each lenslet forms a small image at the pupil of the telescope. With the images being formed at the entrance of the spectrograph, dispersing each image into the spectrum. The result of this is an image acquired at each wavelength and a spectrum captured at every spatial location.

3.2 Observations

RW Aur A was observed between the 21-22 December 2009 UTC using OSIRIS. The adaptive optics system was used in its natural guide star (NGS) with RW Aur A itself being used. The filters chosen for observation were Zbb (1 - 1.18μm), Hbb (1.47 - 1.8μm) and Kbb (1.96 - 2.4μm) with 50 mas pixel scale chosen, providing a field of view

of 0.56" × 2.4" (Larkin et al. 2003), however, by having the stars' positioned differently in each observation, it is possible to make use of mosaicking in the pipeline to increase the FOV to 0.6" × 4.4" for the Hbb filter and 1.15" × 3.8" for the Kbb filter. This allowed for observations of the HeI, [FeII], Brγ and H_2 emission lines — allowing for the diagnostics outlined earlier to be carried out. OSIRIS maintains a spectral resolution of $\sim$ 3900 and velocity resolution of $\sim$ 77 km/s across the entire waveband (Larkin et al. 2003). The position angle of the spectrograph and imager were set to 130° and 177.5° respectively and a seeing of 0.05" was achieved in both Hbb and Kbb.

Band	Date of Observation	Time of Observation	Exposure Time (s)
Kbb	2009-12-21	07:30:43.06	2430
Zbb	2009-12-22	06:21:57.12	1200
Hbb	2009-12-22	07:05:52.77	920

Table 3.1: Observations carried out using the OSIRIS instrument, with the date of observations being in Universal time and the times of observation being quoted in local apparent sidereal time. The principal investigator was Dr. Emma Whelan, project ID is W010o.

3.3   Data Reduction Pipeline

The raw data were acquired from the KOA archive and run through the OSIRIS Data Reduction Pipeline (Lyke et al. (2017) and Lockhart et al. (2019)), this was carried out using an IDL licence provided by Maynooth University on a Fedora 32 machine. As part of the installation, the `libnsl` library had to be installed separately using standard methods. The $\sim\backslash$`.bashrc` file can be seen in Appendix A2.1.

Standard data reduction procedures were carried out using `odrfgui` (the pipeline's GUI) and the `run_odrp` (the command to call the pipeline) which is outlined below. A master dark was created and was used along with each data set's respective rectification matrix as the calibration input files for the modules `Subtract Frame` and `Extract`

`Spectra` respectively. These rectification matrices are maps of the point spread function of each lenslet and are made at all wavelengths. Along with these calibration files, four additional modules were used `Adjust Channel Levels`, `Remove Crosstalk`, `Glitch Identification` and `Clean Cosmic Rays`. These six modules reduced the files, and then they were mosaicked. When mosaicking, the 'AVERAGE' option was chosen over the other options as the most suitable option, this was especially important for the Hbb cube, as when using the 'MEANCLIP' mosaic it distorted a knot while the 'MEDIAN' cut it off. A comparison of the 'MEANCLIP' and 'AVERAGE' can be seen in Figure 3.1. Finally, the data cubes were assembled and the data sets' information was saved using their respective modules, Assemble Data Cube and Save DataSet Information. A sample .xml file with n input files can be seen in Appendix A2.2.

Knot

Skyline

Jet Emission

Jet Emission

Crosstalk
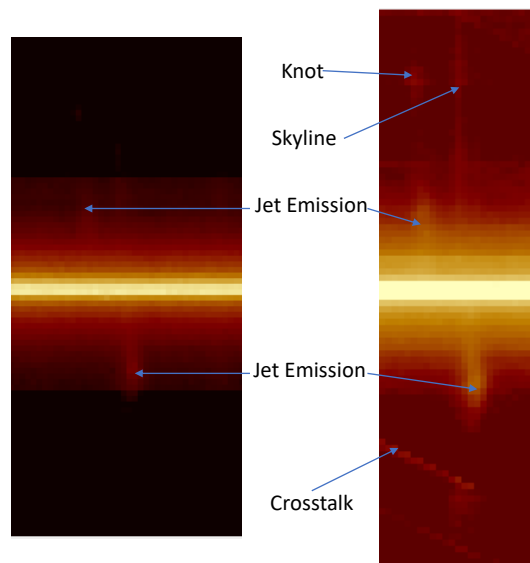
Figure 3.1: Comparison of the 'MEANCLIP' (left) and 'AVERAGE' (right) methods when mosaicking in regard to the 1.644 μm emission. The 'AVERAGE' method achieves a larger field of view ($\sim 0.5"$) in the y-axis, allowing us to observe the blue shifted knot that is extended away from the jet.

3.4   Data Analysis

In a typical jet spectrum observed from the ground, a number of contributions must be considered: continuum emission from the star, broad line components from accretion - seen strongly in Hα, but there are also other accretion tracers like Ca and He, low velocity contribution in lines like [OI] 6300 (likely caused by a wind) and OH skylines from the atmosphere. As a result, a number of procedures outside the pipeline had to be carried out to produce scientifically significant data.

3.4.1   Continuum Removal

When studying jets, we want to isolate the jet emission as close to the star as possible. To do this, a reference spectrum that does not contain any jet emission was subtracted. The reference spectrum (Figure 3.2) is created using a fitting routine that creates a smooth curve that is polynomial in nature, the reference spectrum was then scaled up to the jet emissions using a background reference. An example of this removal can be seen in Figure 3.3. The continuum subtraction routine, `OSIRIS.py` can be seen in Appendix A1.1.

Using these reduced cubes, we can create PVD; the position angle is set to 90° placing a slit along the jet axis, this slit then has its width set to 1". The cubes are then summed within the slit width to create a 2-dimensional image, with dimensions of wavelength and position. To create spectro-images, the reduced cubes were summed within the velocity range of the emission line, creating a 2-dimensional image, with dimensions of RA and Dec.
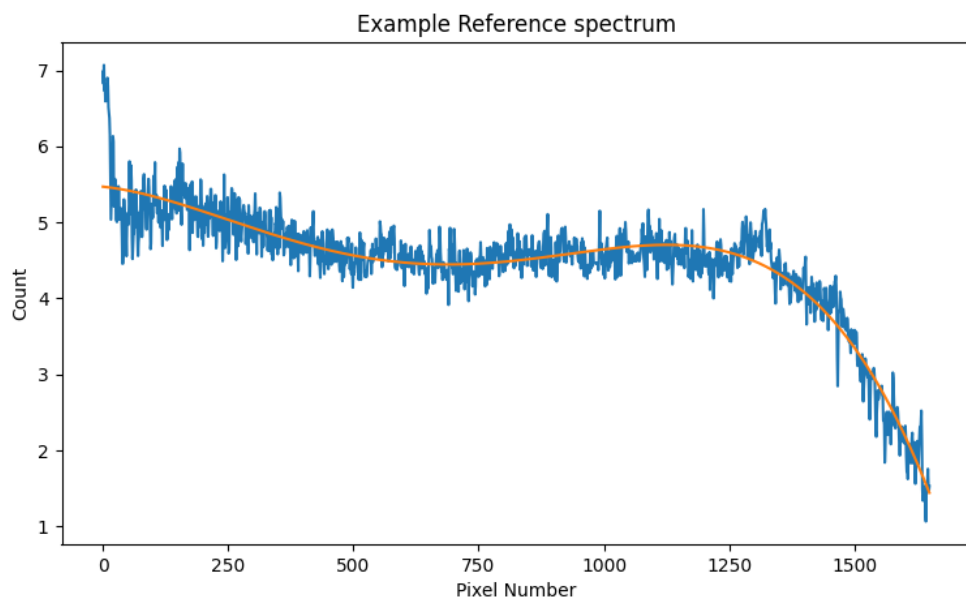
Figure 3.2: Example reference Hbb spectrum taken for the continuum subtraction.
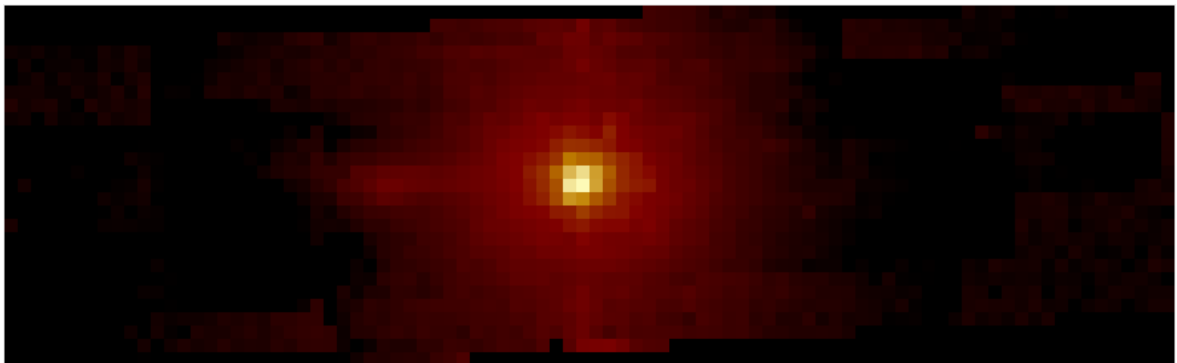
(a) Jet and Continuum Slice
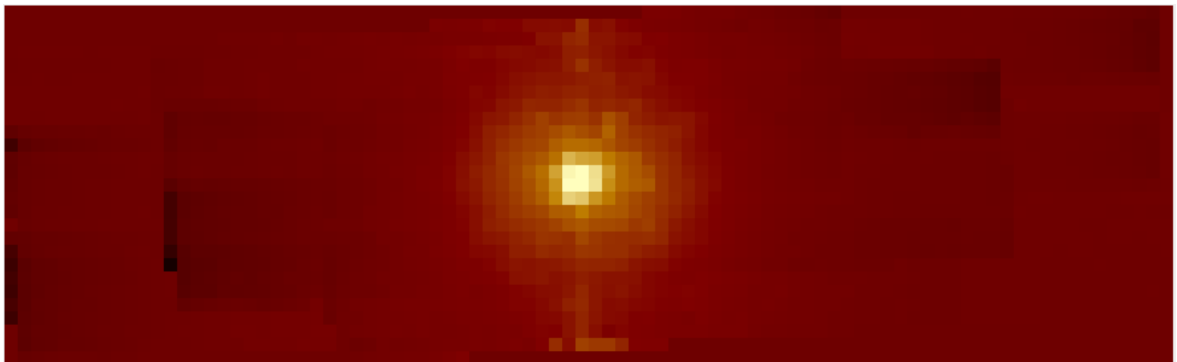
(b) Continuum only
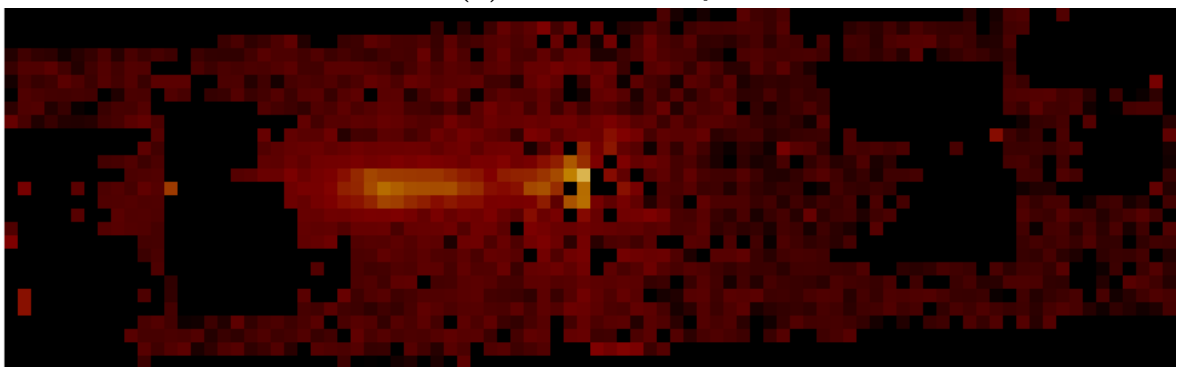
(c) Jet only

Figure 3.3: This figure shows the process of taking a jet slice (a) and subtracting a scaled continuum slice (b), resulting in a pure jet emission image (c) for the [Fe II] 1.644 μm emission line. The axes in the x and y directions are in arbitrary units, however, represent the same wavelength slice.

3.5 Velocity Corrections

The radial velocity of all measurements needed a velocity correction carried out to get the true velocity. Due to motions of the earth a heliocentric correction was carried out using standard methods (Stumpff 1985). A number of OH lines were taken around the sample location (Rousselot et al. 2000), these were compared to the lab frame with an average radial velocity calculated and finally the systemic velocity of RW Aur was taken into account. These values were then used in Eq. 3.1.

$$V_{true} = V_{measured} + V_{heliocentric} + V_{sky} + V_{systemic} \qquad (3.1)$$

Here, $V_{measured}$ is the velocity measured when compared to the rest wavelength of the emission line. $V_{heliocentric}$ is the heliocentric velocity, this was found using the `astropy` package and requires the altitude, longitude, and latitude of the observatory. $V_{systemic}$ is the systemic velocity of RW Aur ($\sim$ 16 km/s Cabrit et al. (2006)) and finally, to correct the wavelength calibration, V_{sky} is found by measuring the wavelength shift of the OH lines. This shift is found by taking the PVD and iterating a Gaussian fitting routine along the length of the OH line; to remove poorly fitted results a selection / rejection routine was used. This routine involved taking values such as the standard deviation and the peak value, comparing them to the data points being fitted. The resulting velocities are then binned, with the median value taken to be the radial velocity for that specific OH line. This was then repeated for a number of lines around the PV plot, with the average then taken.

3.6 Fitting Routines and Statistical Analysis

In later chapters the wiggling of the jet is modelled, to do this, we measure the variation of the centroid position along the length of the jet. To find these centroid values,

each of the columns in the data set had a Gaussian fit applied to it using a standard `scipy.optimize.curve_fit` (Virtanen et al. 2020) routine that guessed parameters for a standard Gaussian (Figure 3.4). A simple accept - reject algorithm was used to discard poorly fitted data, this was done by carrying out a χ^2 optimisation. A sample of the outputs for the fitting routine can be seen in Figures 3.4 — 3.5. Assuming the centroid fits act as a point spread function, they can be measured to an accuracy given by Murphy et al. (2021):

$$\text{Error} = 0.4\frac{\text{FWHM}}{\text{S/N}} \tag{3.2}$$

where the *FWHM* is the Full Width Half Max of the fitted Gaussian and *S/N* is the Signal to Noise ratio, this is defined as:

$$\text{S/N} = \frac{\text{Peak Signal}}{\sigma_{bkg}} \tag{3.3}$$

where σ_{bkg} is the background standard deviation, calculated by taking a region on either side of the profile wings and then calculating the standard deviation using traditional methods:

$$y = \frac{1}{\sigma\sqrt{2\pi}}e^{\frac{-(x-x_0)^2}{2\sigma^2}} \tag{3.4}$$
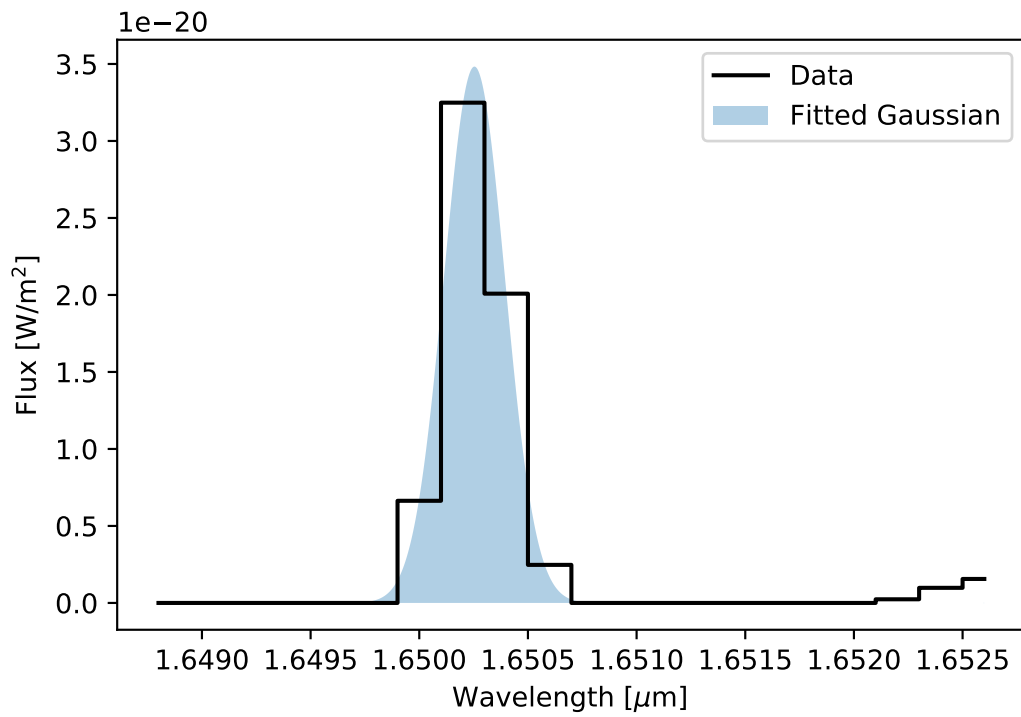
Figure 3.4: Sample of the fitting routine overlaid the observational data.
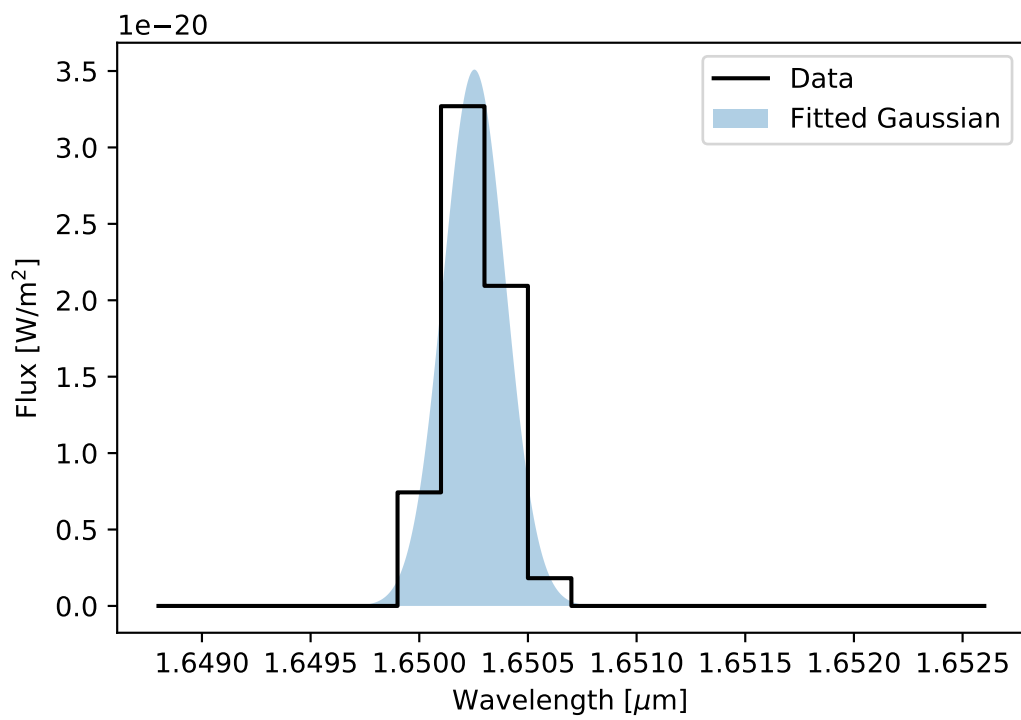
Figure 3.5: Sample of the fitting routine overlaid the observational data.

3.7   Flux Calibration

To flux calibrate the data, two standard stars were selected: HIP 17704 and HIP 29909. These standard stars have known magnitudes in H and K, which were taken from the 2MASS catalogue. To convert the magnitudes to flux densities, the following relations are used.

$$m_1 - m_2 = -2.5\log(F_1/F_2) \tag{3.5}$$

$$F_{calibration}(\text{Standard}) = F_0 \times 10^{-m(\text{Band})/2.5} \tag{3.6}$$

In the two equations above, F_0 is the zero-magnitude flux of a star, taken from the 2MASS catalogue (Table 3.2), $m(\text{Band})$ is the known magnitude of the star. $F_{calibration}$ is the flux of the standard star in the wave band (Table 3.3).

Band	F_λ (Wcm$^{-2}\mu$m^{-1})	λ (μm)
H	$1.133\times10^{-13} \pm 2.212\times10^{-15}$	1.662 ± 0.009
K	$4.283\times10^{-14} \pm 8.053\times10^{-16}$	2.159 ± 0.011

Table 3.2: Zero-Magnitude Attributes of 2MASS Bands Cohen et al. (2003)

Standard Star	Band magnitude	Flux density (Wcm$^{-2}\mu$m^{-1})
HIP 17704	H: 6.641 ± 0.026	$2.499\times10^{-16} \pm 4.680\times10^{-18}$
	K: 6.607 ± 0.024	$9.748\times10^{-17} \pm 1.833\times10^{-18}$
HIP 29909	H: 7.641 ± 0.040	$9.950\times10^{-17} \pm 1.864\times10^{-18}$
	K: 7.635 ± 0.018	$3.782\times10^{-17} \pm 6.995\times10^{-19}$

Table 3.3: List of Standard Stars, with H- & K-bands magnitude values taken from 2MASS. The uncertainties on the fluxes were calculated using standard methods.

A fit of log(F) vs log(λ), was made in the case of each star, the plots of which can be seen in Figures 3.6 and 3.7. The linear equations corresponding to each are given by equations 3.7 & 3.8 respectively.

$$\log_{10}(F_\lambda) = -3.598\log_{10}(\lambda) - 14.808 \tag{3.7}$$

$$\log_{10}(F_\lambda) = -3.697\log_{10}(\lambda) - 34.968 \tag{3.8}$$

The point spread function was fit with an aperture, with a polynomial fit taken of the aperture's spectrum. The linear fits in Equations 3.7 and 3.8 were then divided by their respective polynomial fits, the respective wavelength band (also known as a wave array) was filled in for λ and then the line equation was brought to the power of 10 to retrieve a correction curve on a linear rather than a logarithmic scale for the standard stars (the correction curve for HIP 17704 can be seen in Figure 3.8). The example code for which can be seen below.

```
LineFit = 10**(-3.598*np.log10((WaveArr)) + -14.808)
CorrectionCurve = LineFit/Aperature_Curve
```
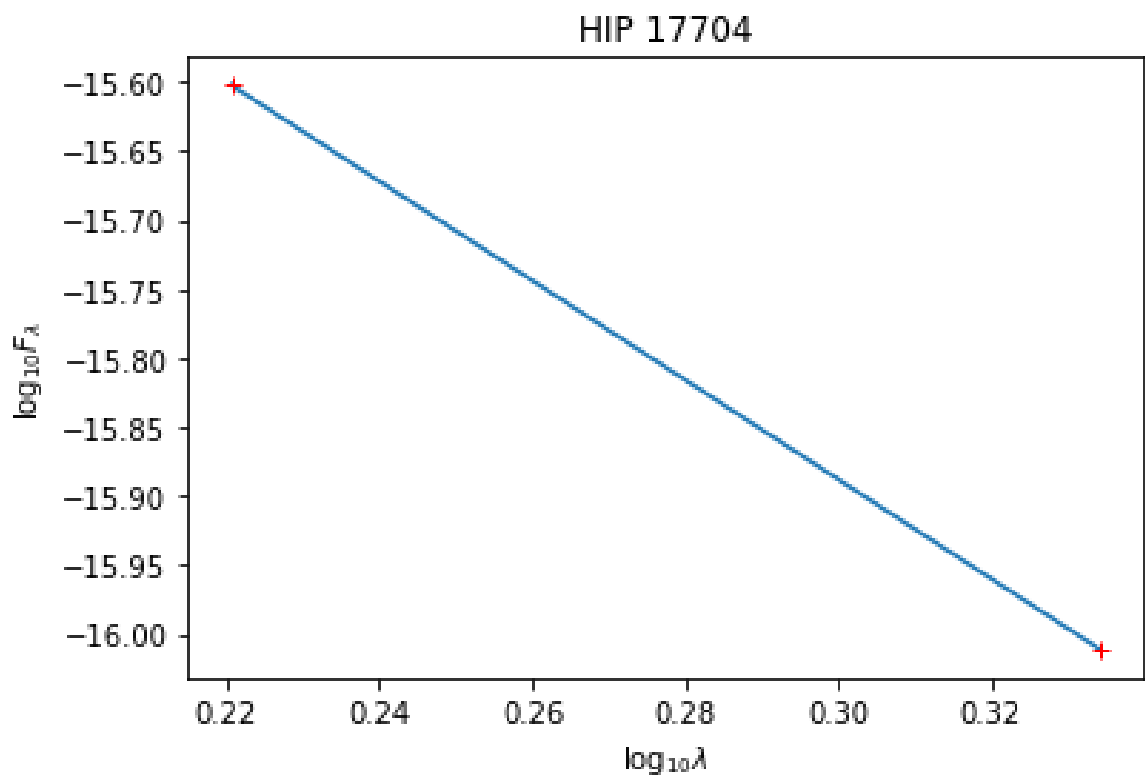
Figure 3.6: $\log_{10}F$ vs $\log_{10}\lambda$ for HIP 17704
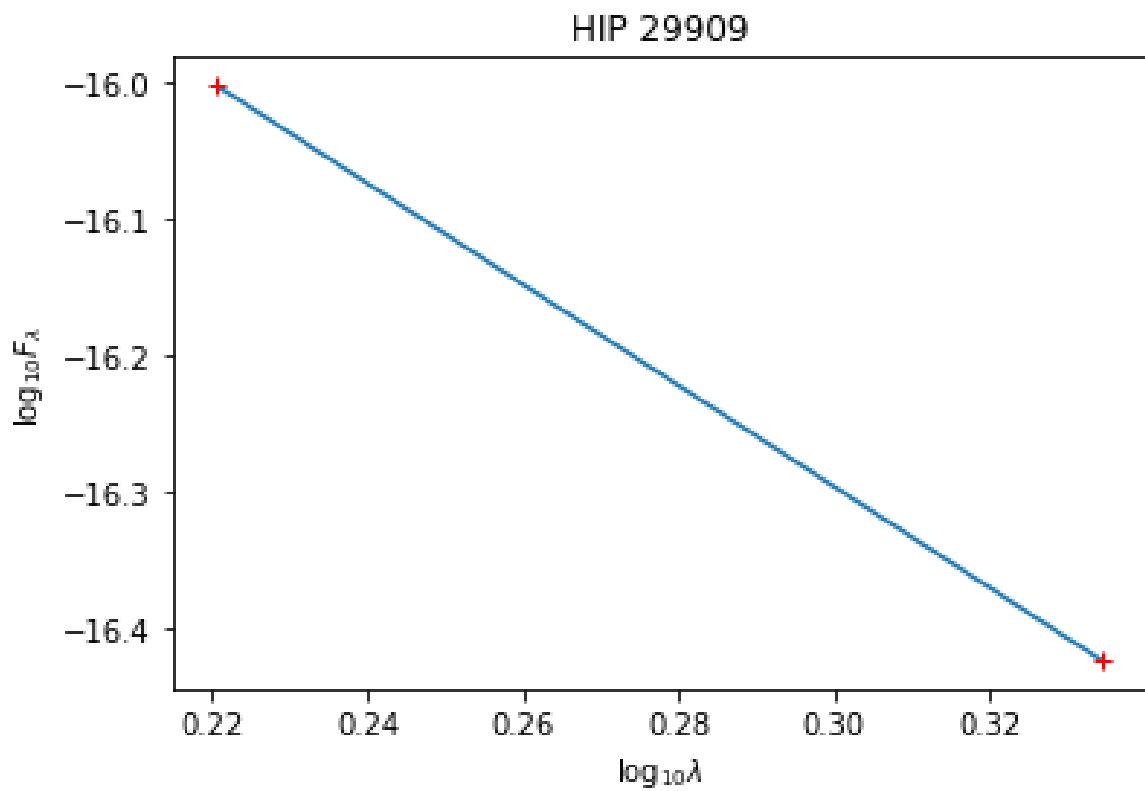
Figure 3.7: $\log_{10}F$ vs $\log_{10}\lambda$ for HIP 29909
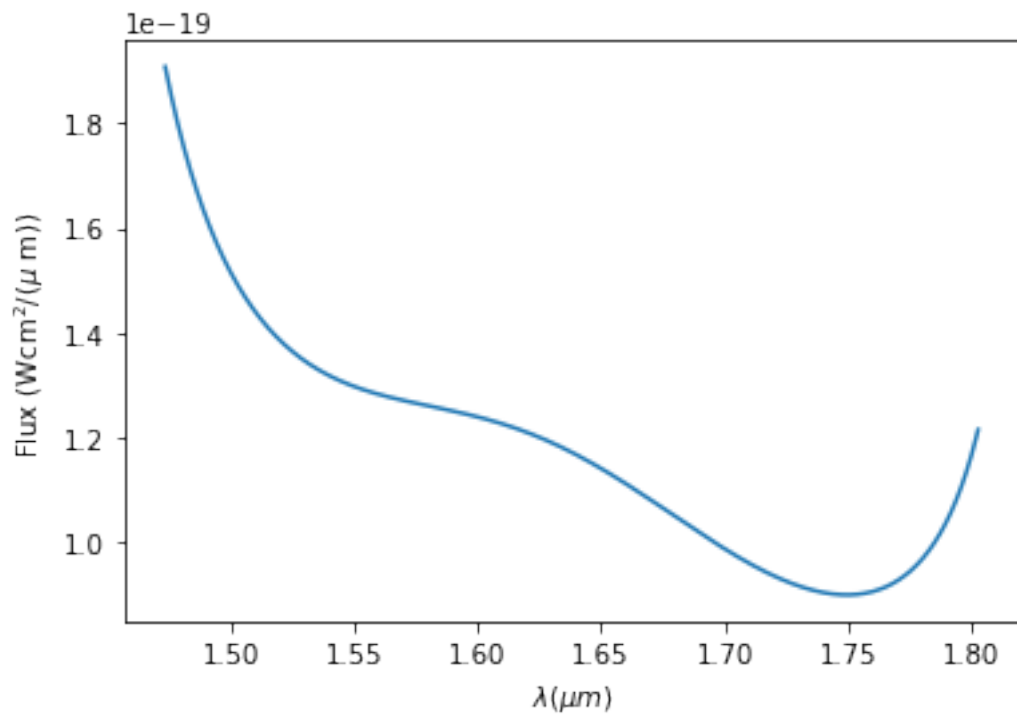
Figure 3.8: Correction curve as described above for HIP 17704

3.7.1 Back-testing the Calibration.

To test the calibration, the correction curves were applied to the standard stars themselves, measuring the flux value at the 2MASS wavelength and then comparing these to the 2MASS index. This back testing of the calibration was also carried out on RW Aur A, the results of the back testing can be seen in Table 3.4.

For the standard stars the magnitude measured are in agreement with those of 2MASS. In the case of RW Aur A the magnitude is outside the margin of error when compared to 2MASS. This can be attributed to 2MASS not resolving RW Aur A and B individually. The magnitude measurements are in line with observations carried out between 2014 — 2016 (Dodin et al. (2019) , Lamzin et al. (2017) & Schneider et al. (2015)), however, this is lower than later observations (Giannini et al. 2019). An obvious outlier in these measurements is the missing HIP 29909 measurement in the H band. This was caused by the OSIRIS pipeline producing poorly reduced cubes. As a result it was not included in the H band flux calibration back testing. However, due to the closeness for the other cubes, it is unlikely that it would have been substantially different from the 2MASS measurements.

Star	Band	Magnitude Measured	2MASS Magnitude
HIP 29909	Hbb	—	7.641 ± 0.040
	Kbb	7.682	7.635 ± 0.018
HIP 17704	Hbb	6.620	6.641 ± 0.026
	Kbb	6.658	6.607 ± 0.024
RW Aur	Hbb	9.326	7.621 ± 0.038
	Kbb	9.864	7.020 ± 0.018

Table 3.4: Table comparing the flux calibrations to the 2MASS catalogue.

4 Morphology & Kinematics

In this chapter, we discuss the results of our observations. With the use of spectro-images and PVD, the morphology of HH 229 using [Fe II] and H_2 emission. We also examine the collimation and the opening angle of the jet and H_2 outflow. PVD and spectro-images were created using methods outlined in §3.4.1. The spectra for each of the bands are found in Figures 4.1 — 4.3, with a list of the emission lines we observe in the jet and the disk found in Table 4.1.
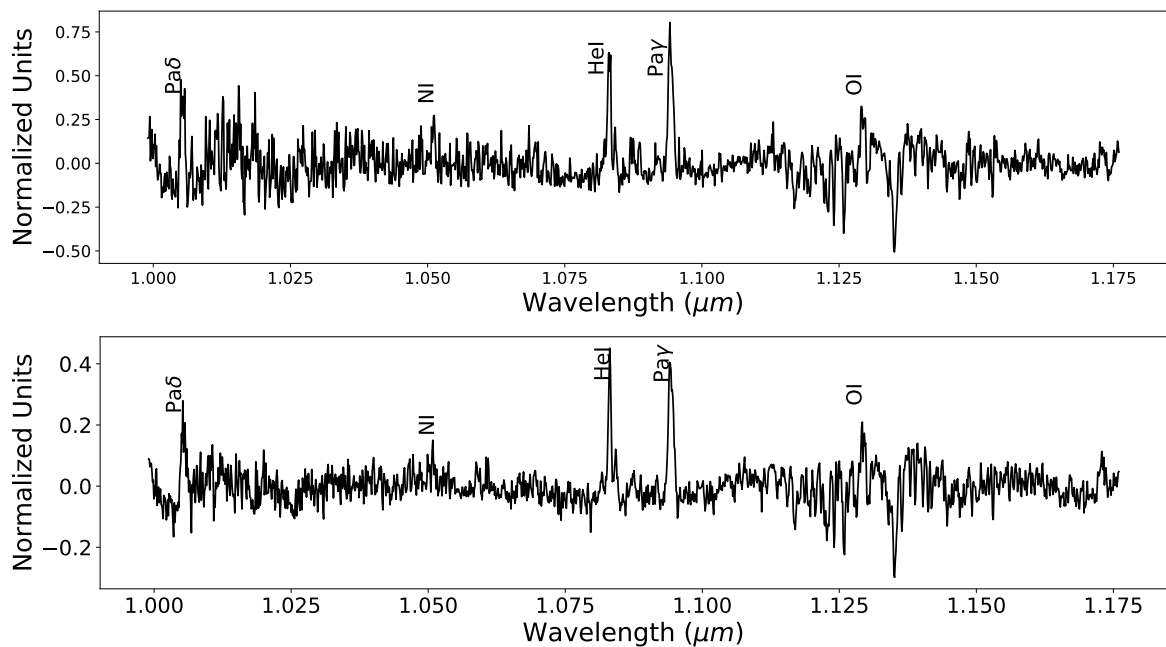
Figure 4.1: Z-band spectra for the RW Aur Jet, with the blue component on top and the red component on the bottom, the intensity axis is normalised so that it's average is zero.
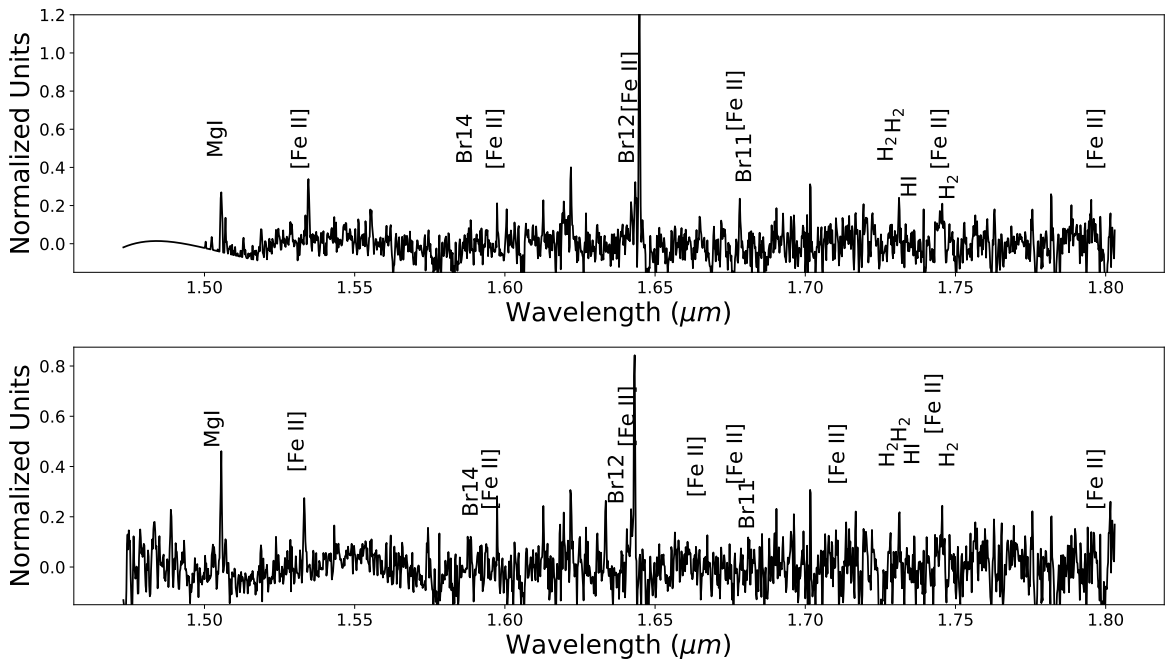
Figure 4.2: H-band spectra for the RW Aur Jet, with the blue component on top and the red component on the bottom, the intensity axis is normalised so that it's average is zero.
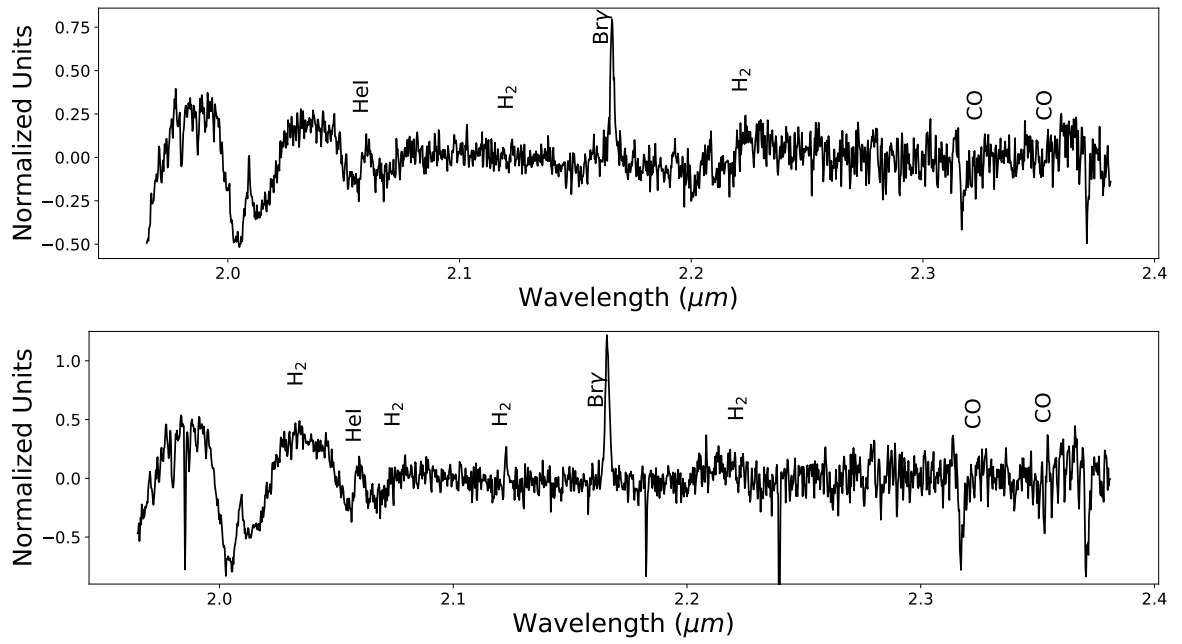
Figure 4.3: K-band spectra for the RW Aur Jet, with the blue component on top and the red component on the bottom, the intensity axis is normalised so that it's average is zero.

Emission Line	λ (μm)	Jet
Paδ	1.005	R, B
NI	1.051	R, B
HeI	1.083	R, B
Paγ	1.094	R, B
OI	1.129	R, B
MgI	1.504	R, B
[Fe II]	1.533	R, B
Br14	1.588	R, B
[Fe II]	1.599	R, B
Br12	1.534	R, B
[Fe II]	1.644	R, B
[Fe II]	1.664	R
[Fe II]	1.677	R, B
Br11	1.681	R, B
[Fe II]	1.711	R
H$_2$ 7-5 Q(1)	1.729	R, B
H$_2$ 6-4 O(3)	1.733	R, B
HI	1.736	R
[Fe II]	1.745	R, B
H$_2$ 1-0 S(7)	1.748	R, B
[Fe II]	1.797	R, B
HeI	2.026	R, B
H$_2$ 2-1 S(2)	2.074	R
H$_2$ 2-1 S(3)	2.223	R
H$_2$ 1-0 S(1)	2.122	R, B
Brγ	2.155	R, B
H$_2$ 1-0 S(0)	2.223	R, B
CO (3-1)	2.323	R, B
CO (4-2)	2.353	R, B

Table 4.1: List of lines in which we observe the RW Aur jet, corresponding to the spectra in Figures 4.1 — 4.3.

4.1   Position Velocity Diagrams

The PVD in Figure 4.4 is centred around the [Fe II] 1.644 line, the Br12 recombination line (λ_{vac}=1.6411μm) is visible on the PVD and can be seen to the left of the blue-shifted lobe centred around -500 km/s. In the blue shifted component of the [Fe II] 1.644μm an extended knot is seen at $\sim$ 1.6" away from the jet. The PVD in Figure 4.5 is centred around the [Fe II] 1.533μm line. These PVD have a relatively narrow line width compared to the modelled PVD (Figure 1.4) of a disk wind at the jet. The narrow width of the high velocity component is in support of an X-wind, where there is a small localized launching region. In comparison, with the broadened, low velocity emission favours the presence of a cold disk wind. These results are consistent with previous observations (Pyo et al. (2006) and Liu & Shang (2012)).

Figure 4.6 shows the PVD for the H_2 emission. The region with the highest densities being closer to the source (<0.5") when compared to the [Fe II] emissions in Figure 4.4 & 4.5 where the regions of the highest densities are extended and collimated away from the launch site.

Post subtraction of the stellar continuum, what appeared to be spatially extended Brγ (see Appendix A3) was observed in the direction of the blue lobe, centred around $\sim$ 0 km/s. Upon further inspection, this can be considered a false positive for a number of reasons; firstly, measurements before and after our observations (mentioned earlier) were unable to resolve spatially extended Brγ in the RW Aur jet making it unlikely that this measurement was accurate. Secondly, the pre-subtracted continuum contains, as expected, a high amount of Brγ, however, there is no significant difference between the positive or negative directions (with respect to the distance from the star). As a result, this Brγ 'outflow' can be attributed to remnant emission not properly subtracted by the fitting routine. As a result, similar results to Beck et al. (2010) are found, in that these observations are unable to resolve spatially extended Brγ emission in the jet,

attributing the emission almost entirely to disk accretion, this will be discussed further in §5.1.

4.2   Spectro-images

Blue and red-shifted spectro-images for [Fe II] can be seen in Figure 4.7 — 4.8. Because there were no clear LVC and HVC in the PVDs these have been integrated over their total velocity range. There is a knot separated from the blue shifted component in the [Fe II] 1.644μm jet, located around $\sim$ 1.8" in Figure 4.7. However, this knot is not observed in any of the fainter [Fe II] emission lines.

The spectro-image in Figure 4.9 shows the H_2 outflow in the red component of the jet under the total velocity ranges. Compared to the outflow being collimated in the [Fe II] lines, the H_2 has a more "carrot" like outflow shape. Unfortunately, due to a lower spectral resolution, velocity resolution and smaller field of view compared to Beck et al. (2008) ($\sim$ 5300, $\sim$ 57 km/s and 3"$\times$3" respectively (Beck et al. 2008)), a comparison to Figure 12 cannot be performed as the jet is too wide for the FOV, giving the straight edges. While in the Beck et al. (2008), the FOV is over 1".
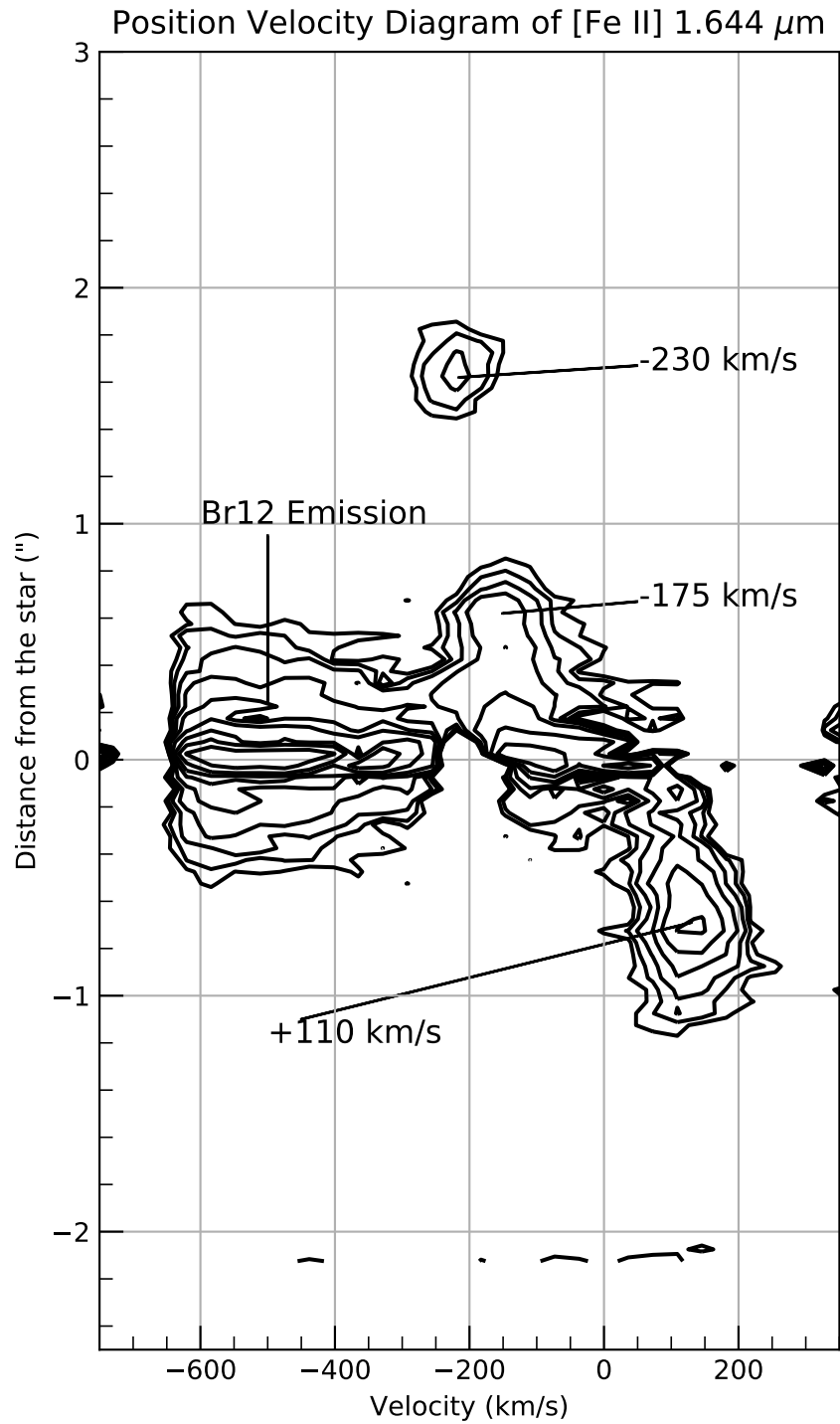
Figure 4.4: Position-Velocity diagram centred around [Fe II] 1.644μm with contour levels drawn at $5\%(\text{peak}) \times \sqrt{2} \times \sigma$, where σ is the standard deviation. Br12 emission is seen centred around -500 km/s. Similar to Figure 4 of Pyo et al. (2006), a telluric absorption feature (-200,0) can be seen in the blue shifted component.
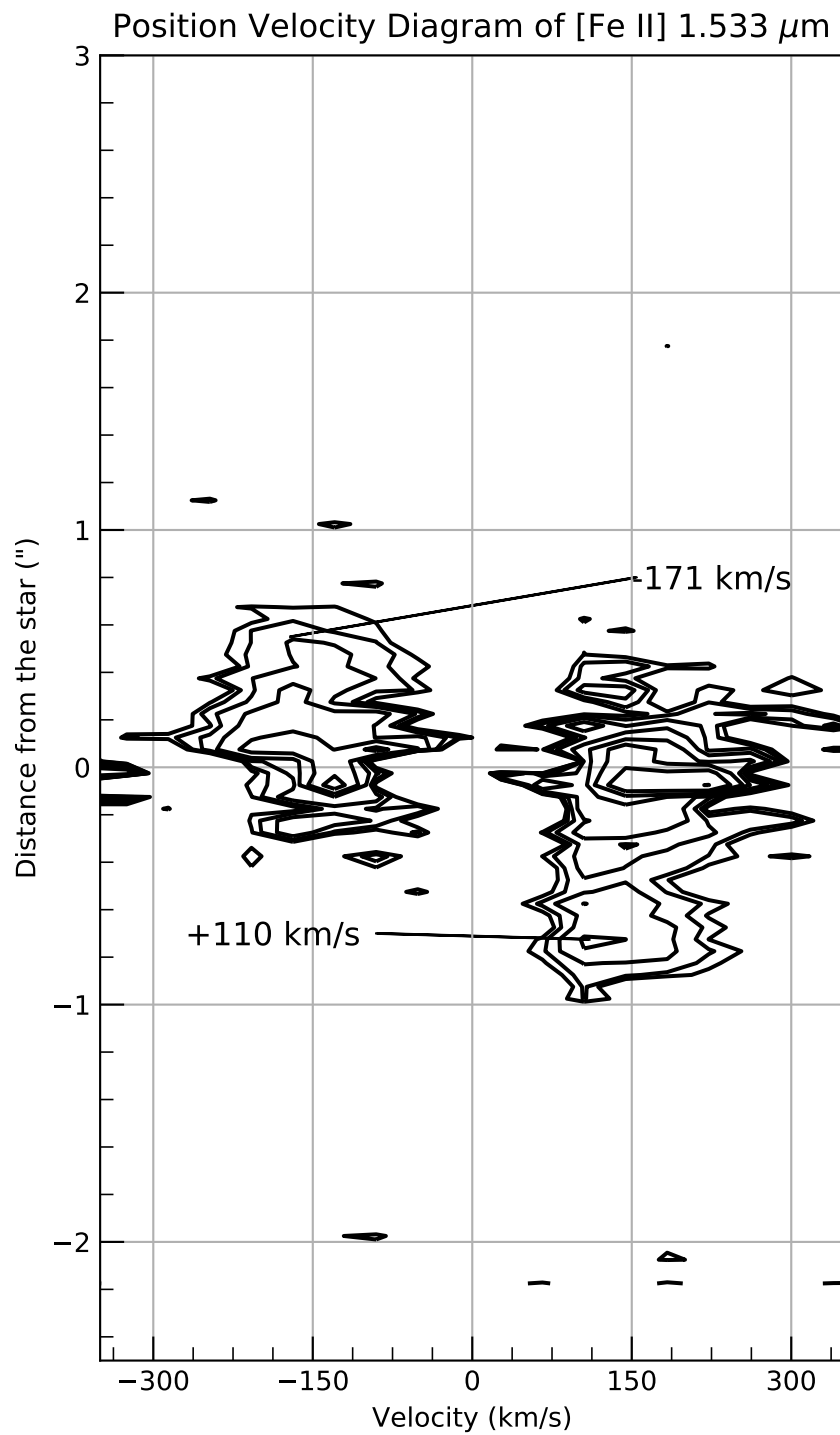
Figure 4.5: Position-Velocity diagram centred around [Fe II] 1.533μm with contour levels drawn at 5%(peak) $\times \sqrt{2} \times \sigma$, where σ is the standard deviation.
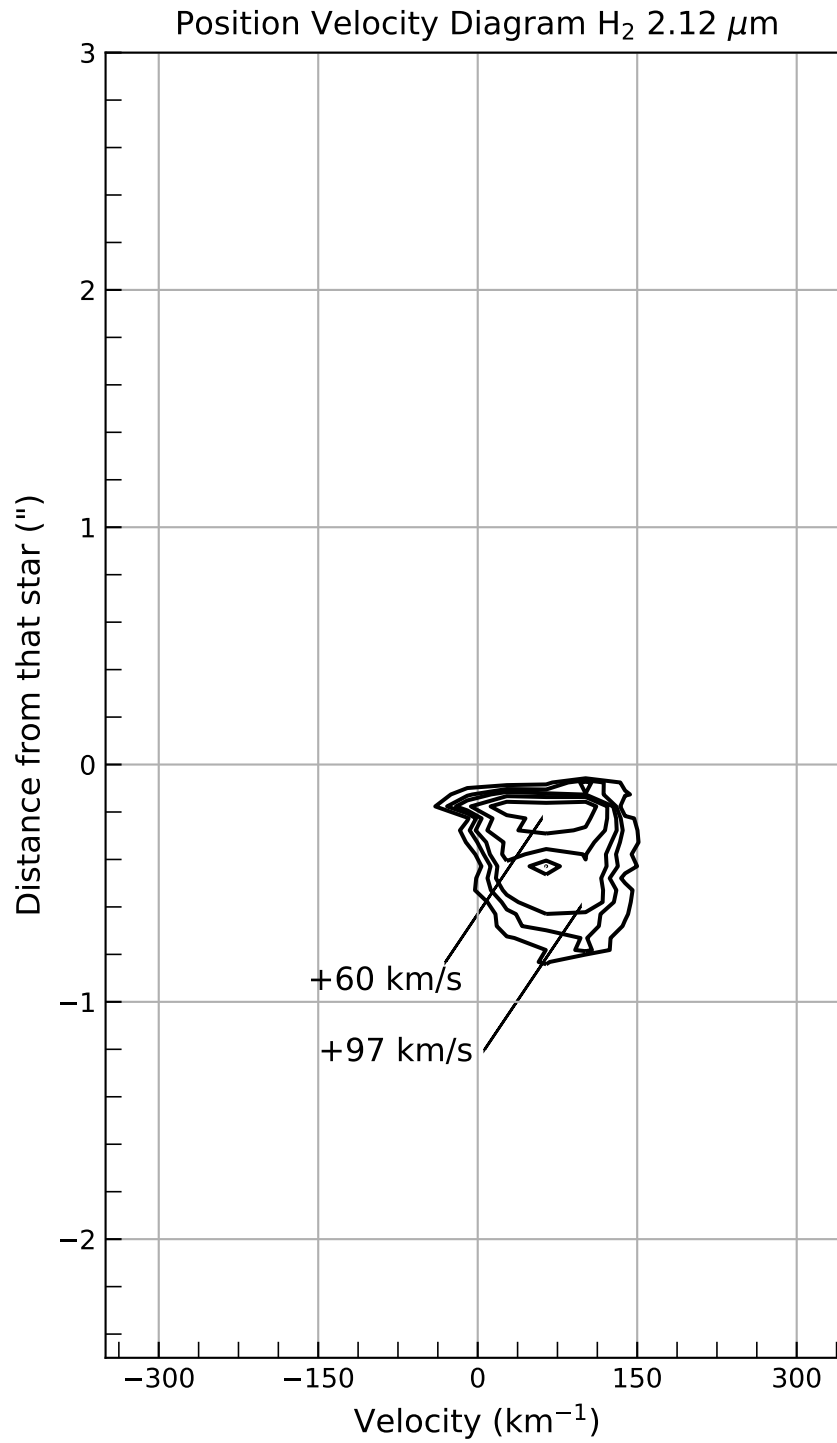
Figure 4.6: Position-Velocity diagram of the H_2 2.12μm emission line with contour levels drawn at 5%(peak) $\times$ $\sqrt{2} \times \sigma$, where σ is the standard deviation.
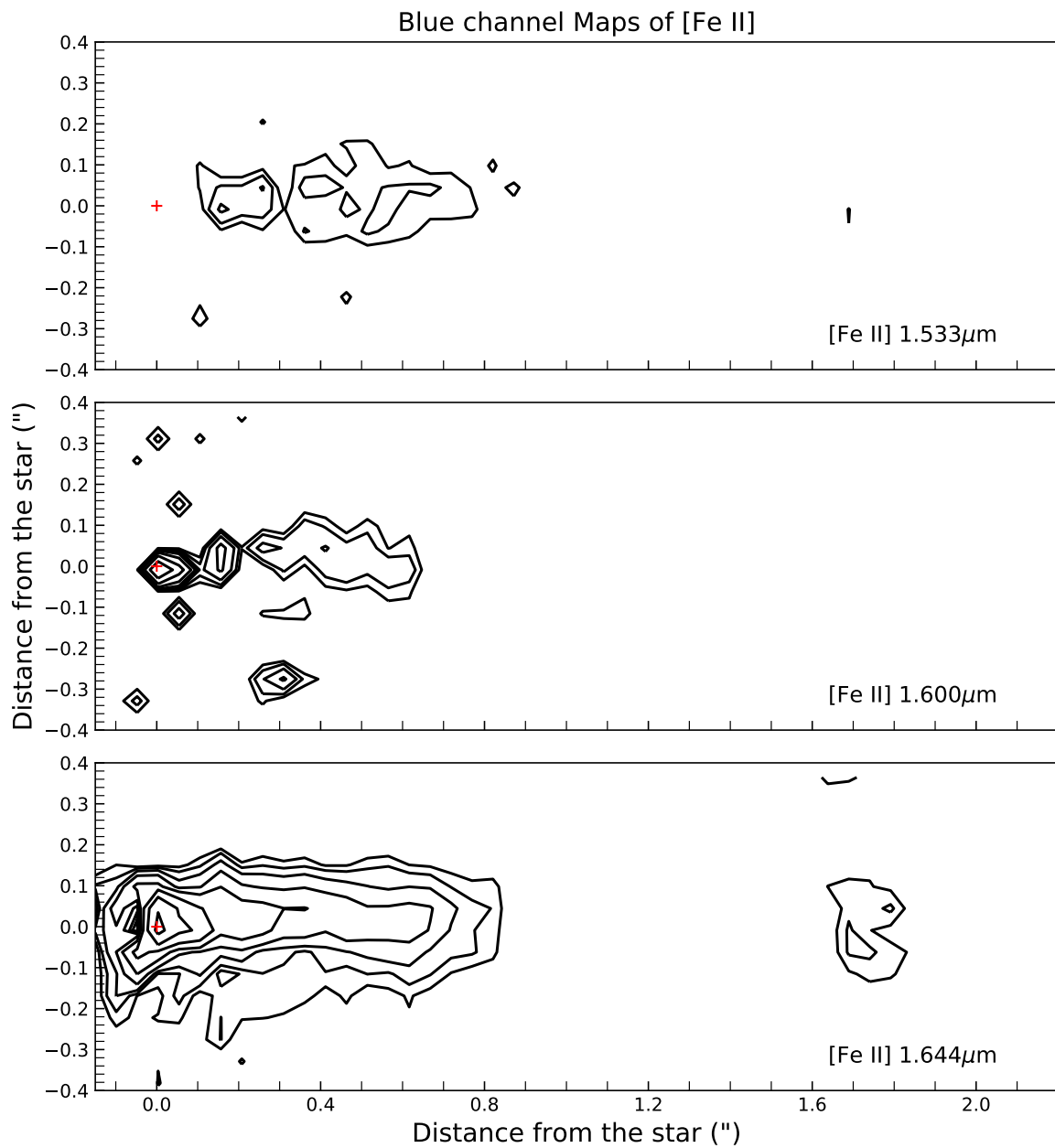
Figure 4.7: Blue channel maps of all [Fe II] observed in numerical order. Contour levels are at $5\%(\text{peak}) \times \sqrt{2} \times \sigma$, where σ is the standard deviation. The velocity range is [0,-250]km/s for all emission lines.
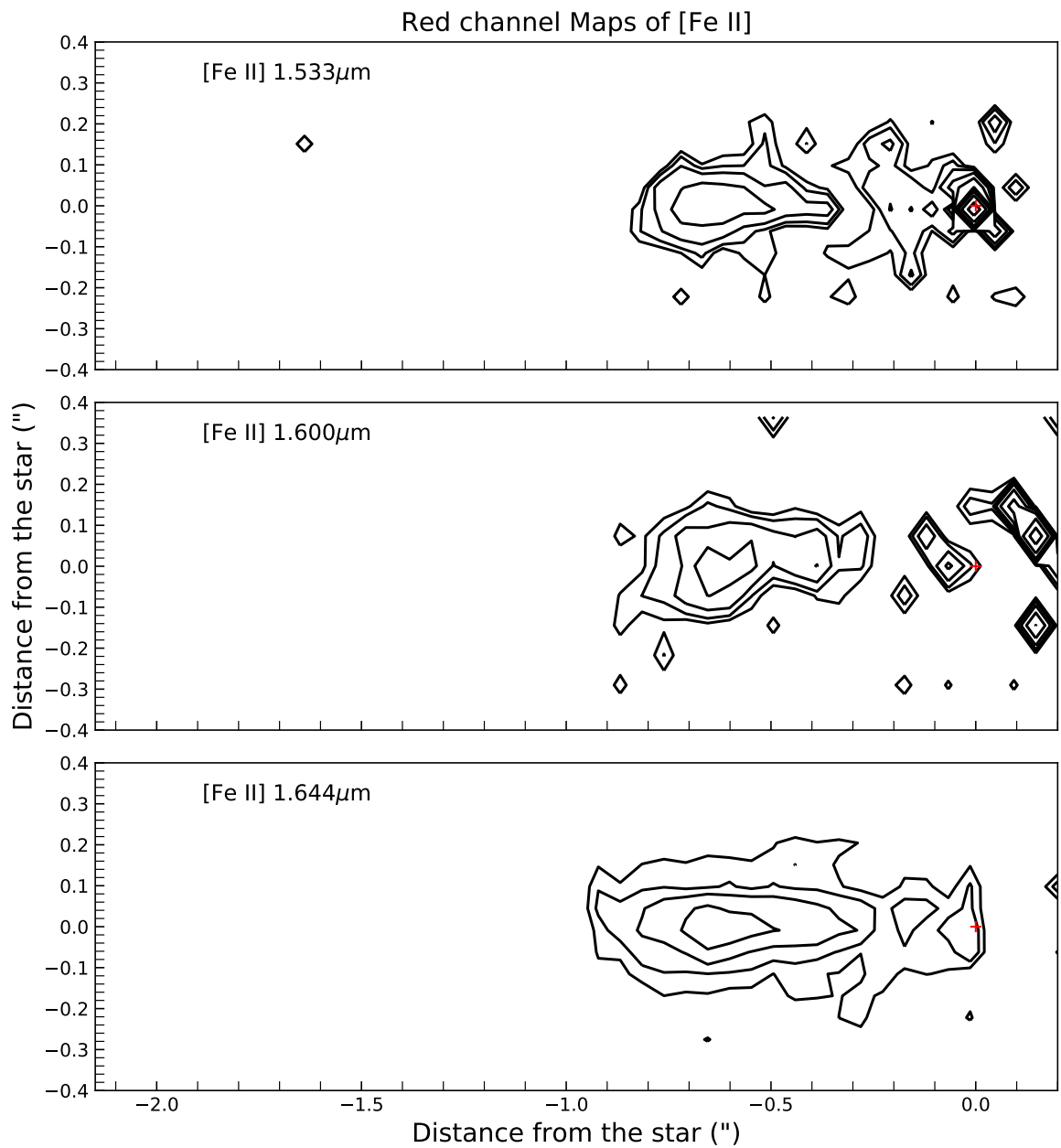
Figure 4.8: Red channel maps of all [Fe II] observed in numerical order with contour levels drawn at $5\%(\text{peak}) \times \sqrt{2} \times \sigma$, where σ is the standard deviation. The velocity range is [0,300]km/s for all emission lines.
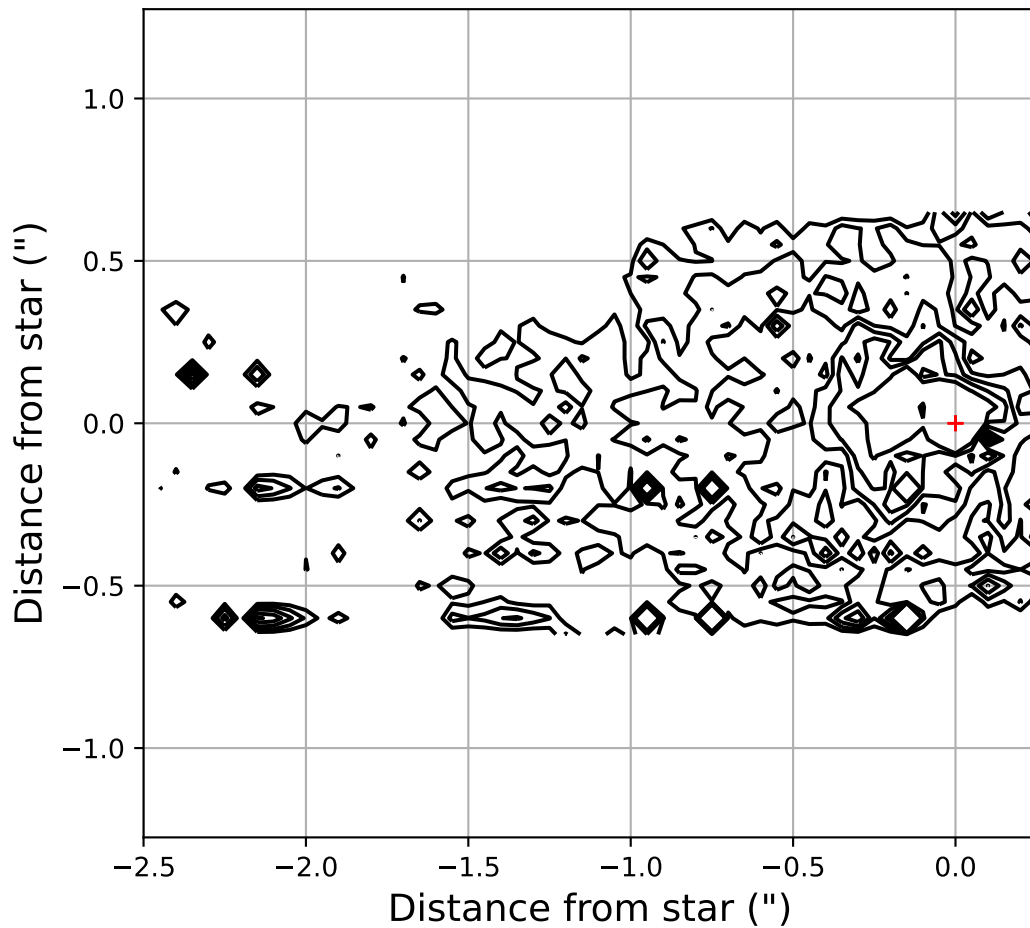
Figure 4.9: Spectro-image of the H_2 2.12μm emission, integrated over the total velocity range, the width is truncated by the FOV of the observations. Contour levels are drawn at $5\%(\text{peak}) \times \sqrt{2} \times \sigma$, where σ is the standard deviation.

4.3   Knot Positions

Using standard methods outlined in §3.6, the knot positions were fitted using Gaussian curves, with the knot position taken to be the mean value of the fitted Gaussian so the full width of the region is taken into account. These curves can be seen in Figures 4.10 and 4.11. In the case of the blue jet, there are three knots in the main body of the jet (0.05", 0.2" and 0.59") with a fourth knot extended at 1.69". For the red jet, there are two knots distinct knots (-0.7" and -0.17").

When compared to the H_2 outflow, there is general agreement in the knot positions, however, the radial velocity of the knots are lower than that of the [Fe II] $1.644\mu m$ emission (Figures 4.4 & 4.6). Similar to Beck et al. (2008), most of the H_2 emission is mono-directional, with the position of the knots of the emission corresponding to the inner jet region as opposed to a H_2 cavity typically seen in CTTS Massi et al. (2004) Lopez et al. (2013).

The dominant knot, close to the source in the H_2 outflow, is moving at a significantly lower speed than that of the [Fe II] emission. Indicating a very different origin, such as a cooler region closer to the circumstellar disk. H_2 outflow was not observed in the blue-shifted jet.

A full list of knot positions can be seen in Table 4.2.

Emission Line	Jet	Knot position
[Fe II] 1.644 μm	B	0.05 $\pm$ 0.03"
[Fe II] 1.644 μm	B	0.20 $\pm$ 0.18"
[Fe II] 1.644 μm	B	0.59 $\pm$ 0.11"
[Fe II] 1.644 μm	B	1.69 $\pm$ 0.08"
[Fe II] 1.644 μm	R	-0.17 $\pm$ 0.12"
[Fe II] 1.644 μm	R	-0.70 $\pm$ 0.23"
H_2 2.1212 μm	R	-0.23 $\pm$ 0.11"
H_2 2.1212 μm	R	-0.60 $\pm$ 0.21"

Table 4.2: Table of knot positions for the [Fe II] and H_2 emission lines.
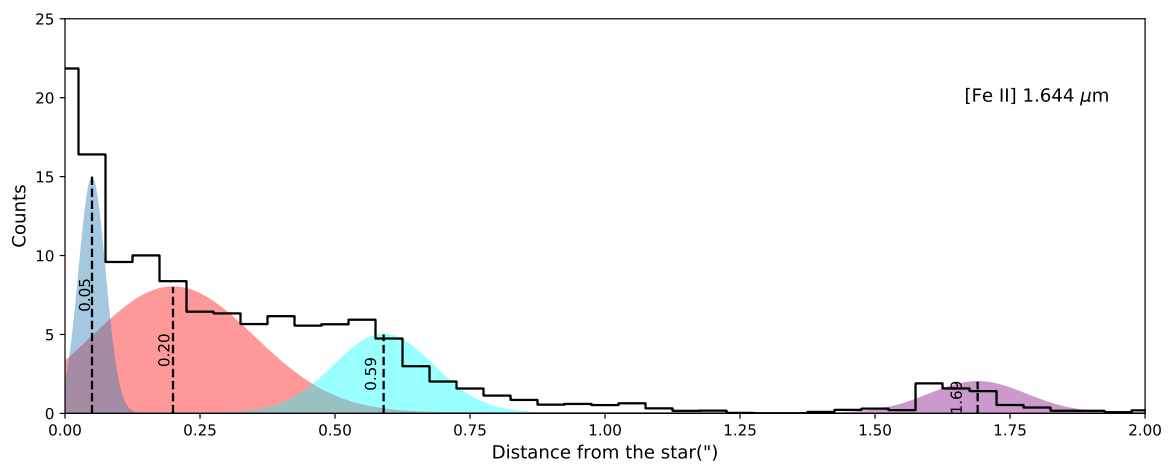
Figure 4.10: Knot positions for the blue [Fe II] 1.644μm, with the knot positions taken from the mean value of the Gaussian curve, a plot was created by taking a three pixel wide slice along the length of the jet through the centre, over the total velocity range. The black step plot is the data points, while the shaded Gaussians are those fitted using `scipy.optimize.curve_fit`.
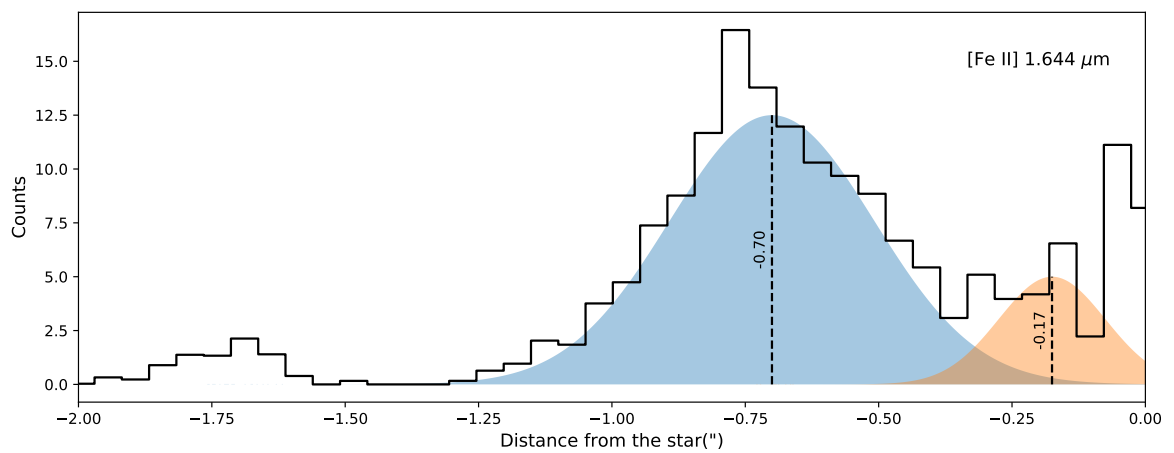
Figure 4.11: Knot positions for the red [Fe II] 1.644μm, with the knot positions taken from the mean value of the Gaussian curve. The plot was created by taking a three pixel wide slice along the length of the jet through the centre, over the total velocity range. The black step plot is the data points, while the shaded Gaussians are those fitted using `scipy.optimize.curve_fit`. Remnant emission from the removed skyline subtraction can be seen at -1.75 on the x-axis.
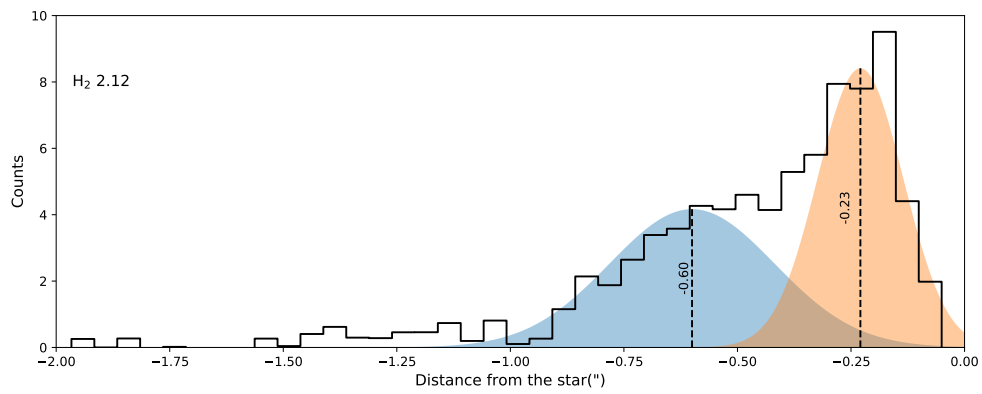
Figure 4.12: Knot positions for the H$_2$ outflow, with the knot positions taken from the mean value of the Gaussian curve. The plot was created by taking a three pixel wide slice along the length of the jet through the centre, over the total velocity range. The black step plot is the data points, while the shaded Gaussians are those fitted using `scipy.optimize.curve_fit`.

4.4   Proper Motion of the Knots

In astronomy, the proper motion is the apparent rate of change of position in the sky. To measure the proper motion of the RW Aur jets' knots, knot locations were compared to previous measurements (Takami et al. (2020), Liu & Shang (2012) and López-Martín et al. (2003)). The error on the proper motions was determined to be best represented by taking the error on the centroid to be half the FWHM of the fitted curve (Ellerbroek et al. 2014). For the blue jet, knot locations are taken to be at 0.05 ± 0.03 arcsec/year, 0.20 ± 0.18 arcsec/year, 0.59 ± 0.11 arcsec/year and 1.69 ± 0.08 arcsec/year. In the case of the inner two knots, reliable measurements for the knot locations were unable to be found in the literature. However, in the case of the 1.69" knot, this is identified to be the knot B5 (0.2") from López-Martín et al. (2003), this gives us a proper motion of 0.166 ± 0.009 arcsec/year. The inner two knots are unlikely to be the same knots as those observed by López-Martín et al. (2003) as the proper motion would be ≤ 0.044 arcsec/year. Archival data from X-Shooter on the European Southern Observatory's (ESO) telescope, the Very Large Telescope (VLT) (Vernet et al. 2011) was accessed. Assuming that the inner knots at 0.2 and 0.59 have a proper motion of 0.166 arcsec/year like the outermost knot (Figure 4.13), it can be seen that there is agreement in the position of the knots with respect to the assumed proper motions and OSIRIS knot positions.

For the red jet, knot locations are taken to be at -0.7 ± 0.23 arcsec/year and -0.17 ± 0.11 arcsec/year. None of the knots observed by Liu & Shang (2012) and López-Martín et al. (2003) can be identified to be the same as those in our observations. However, knots 'A' (1.4") and 'B' (1.018") from Takami et al. (2020) have been determined to be the same knots as in our observations. Assuming a time difference of 1015 days between observations, we obtain proper motions of 0.252 ± 0.079 arcsec/year and 0.305 ± 0.040 arcsec/year (for A and B respectively).
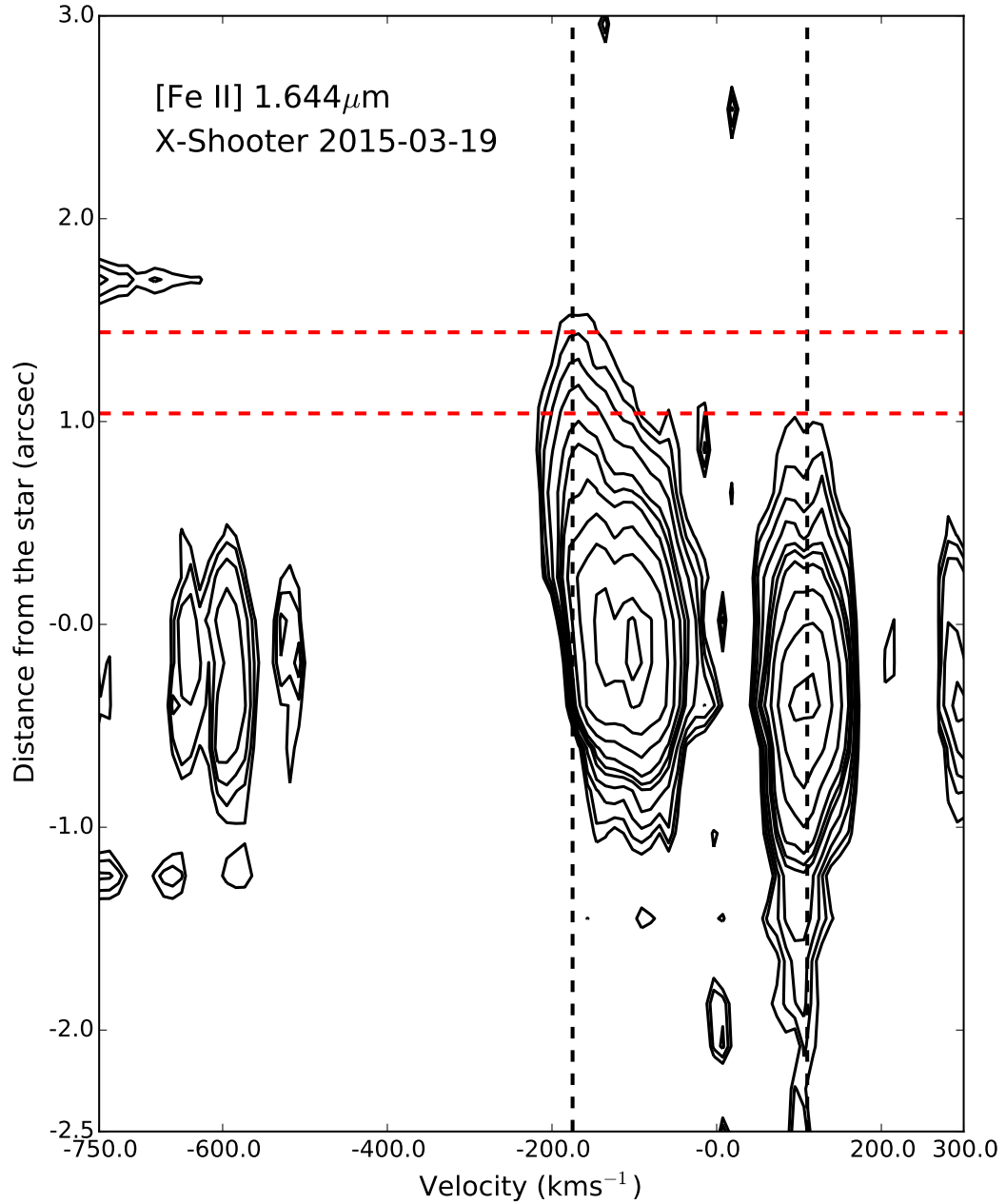
Figure 4.13: PV diagram of the Fe II 1.644μm line in a 2015 X-Shooter spectrum of RW Aur (program ID: 294.C-5047(A)). Contours start at 6-sigma and increase by a factor of $\sqrt{2}$. The black dashed lines mark the radial velocities of the blue and red-shifted jets measured in the OSIRIS data. The red dashed lines mark the estimated positions of the inner knots detected in the blue-shifted jet, assuming a proper motion of 0.166 arcsec/year.
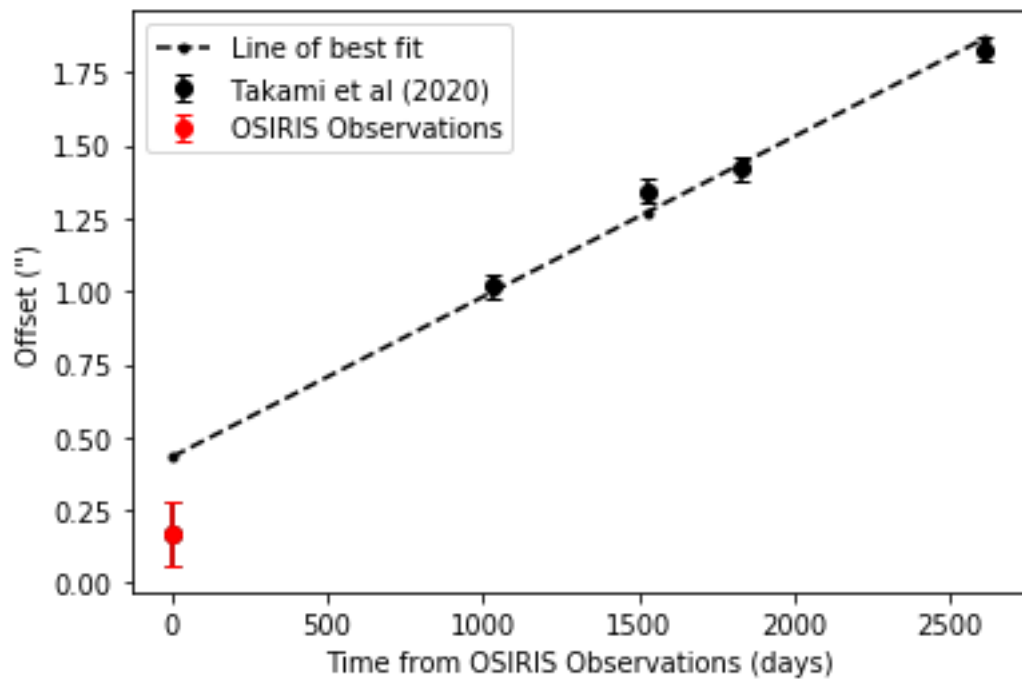
Figure 4.14: Graph used to determine the proper motion, with measurements from Takami et al. (2020) added.

4.5   Opening Angle of the Jet

Using methods outlined in §3.6, Gaussian fits were applied to the jet. Due to its relative brightness, the [Fe II] 1.644μm emission line was used, along with the H$_2$ emission line. Figures 4.15 — 4.17 show the FWHM as a function of distance from the source. The opening angle in each case was estimated by a linear fit to the lower bounds of the FWHM measurements (Murphy et al. (2021)). The corresponding table of results can be seen in Table 4.3. The error on the fit was calculated using methods outlined in 3.6, given by:

$$\text{Error} = 0.4 \frac{\text{FWHM}}{\text{S/N}} \tag{4.1}$$

Emission Line	Jet	Opening Angle
[Fe II] 1.644μm	Blue	$5.31 \pm 2.59°$
[Fe II] 1.644μm	Red	$16.57 \pm 2.59°$
H$_2$ 2.12μm	Red	$33.9 \pm 17.55°$

Table 4.3: Table summarising the opening angles from Figures 4.15 — 4.17.

4.6   Centroids

The same routine used to measure the opening angle also provided the centroid position for the jet. This routine was used on the [Fe II] 1.644μm emission line, due it having the highest signal-to-noise ratio (10.6) compared to that of the [Fe II] 1.533 μm (6.5) and 1.600 μm (2.7) emission lines. For the 1.644μm emission line, both the blue and red components of the jet (Figures 4.18 & 4.19) demonstrate evidence for wiggling. With a clear sinusoidal pattern observed outside the error range. In the case of the H$_2$ outflow (Figure 4.20), evidence of wiggling is less apparent. In §6 these wiggles will be investigated to determine if this can be caused by the existence of an unseen companion (discussed in §1.4).
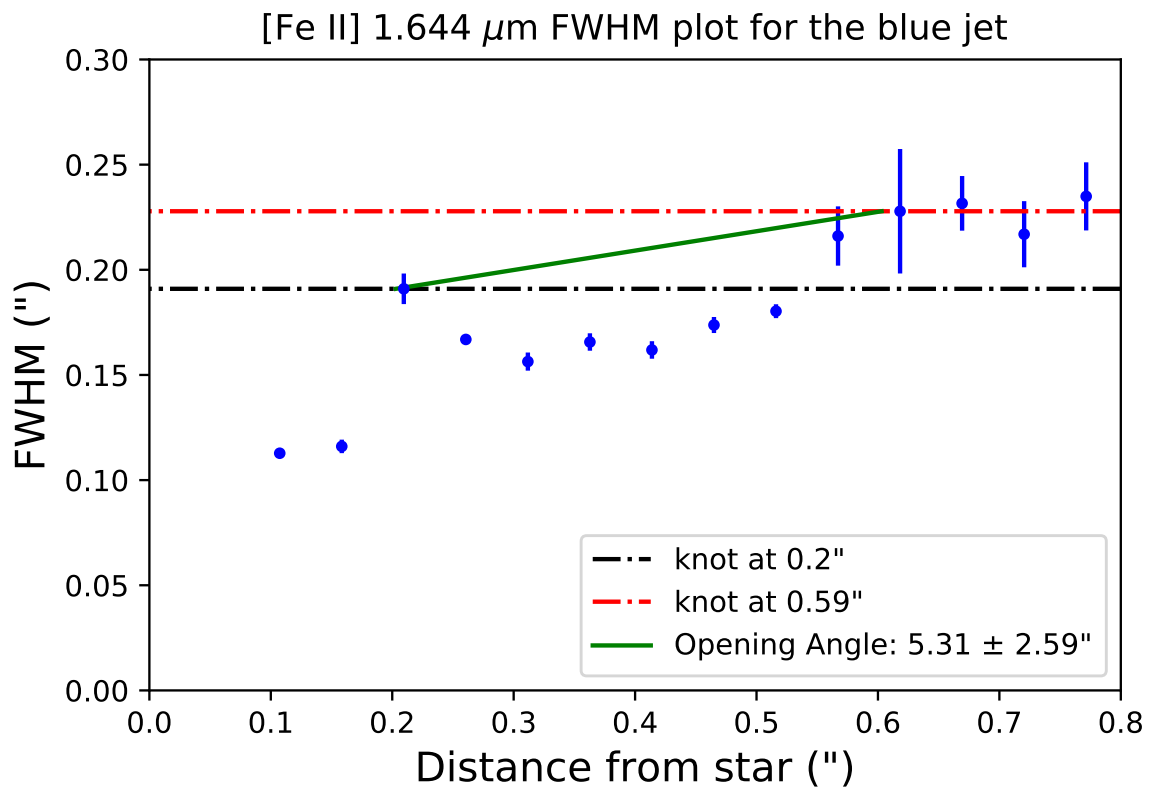
Figure 4.15: FWHM as a function of distance from the star. The dashed red line corresponds to the knot at 0.59" while the dashed black line corresponds to the knot at 0.2", with the linear fit in green used for the [Fe II] 1.644μm emission opening angle for the red jet.
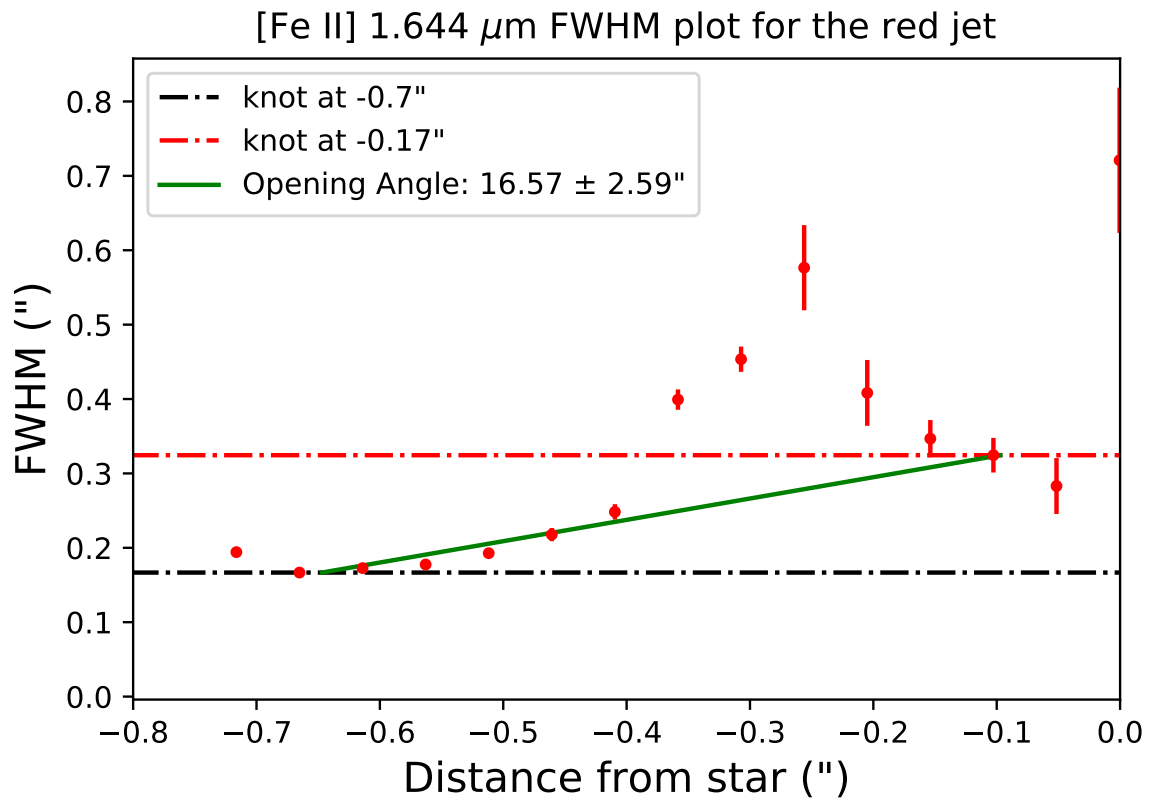
Figure 4.16: FWHM as a function of distance from the star. The dashed red line corresponds to the knot at -0.17" while the dashed black line corresponds to the knot at -0.7", with the linear fit in green used for the [Fe II] 1.644μm emission opening angle for the red jet.
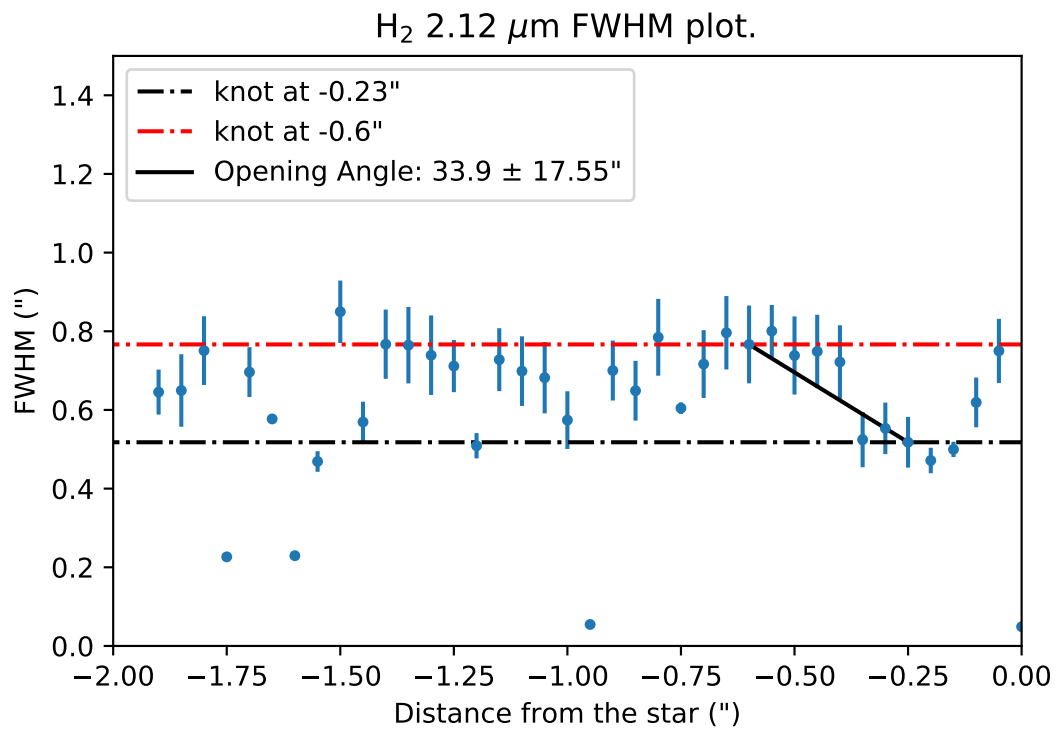
Figure 4.17: FWHM as a function of distance from the star. The dashed red line corresponds to the knot at -0.6" while the dashed black line corresponds to the knot at -0.23", with the linear fit in green used for the [Fe II] 1.644μm emission opening angle for the red jet, with the linear fit used for the H$_2$ emission opening angle.
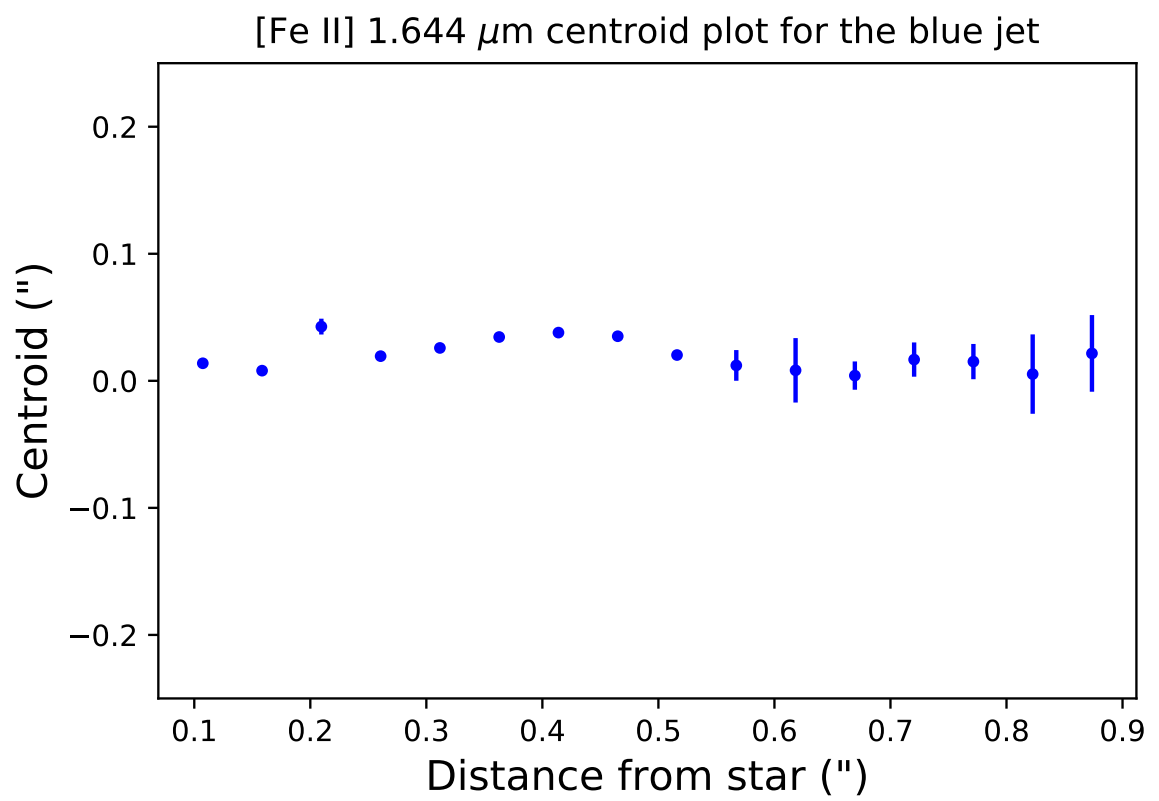
Figure 4.18: Centroids as a function of distance from the star for the blue-shifted jet, over the total velocity range.
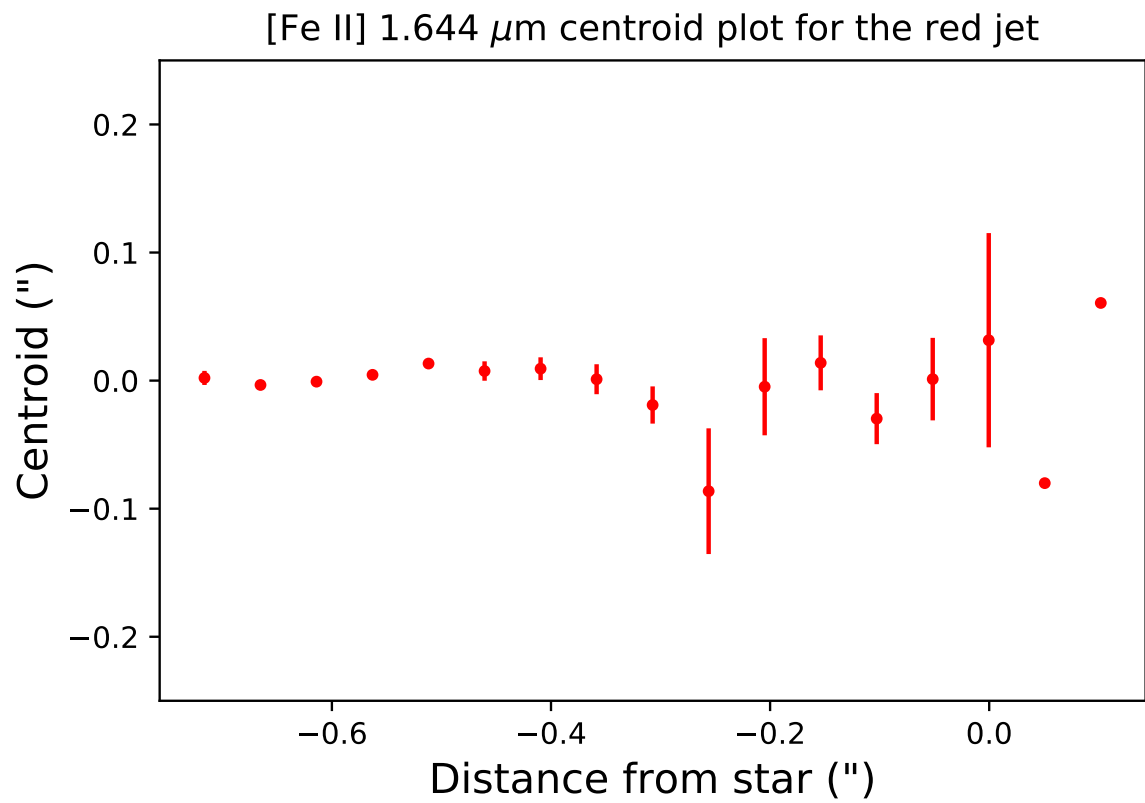
Figure 4.19: Centroids as a function of distance from the star for the red-shifted jet, over the total velocity range.
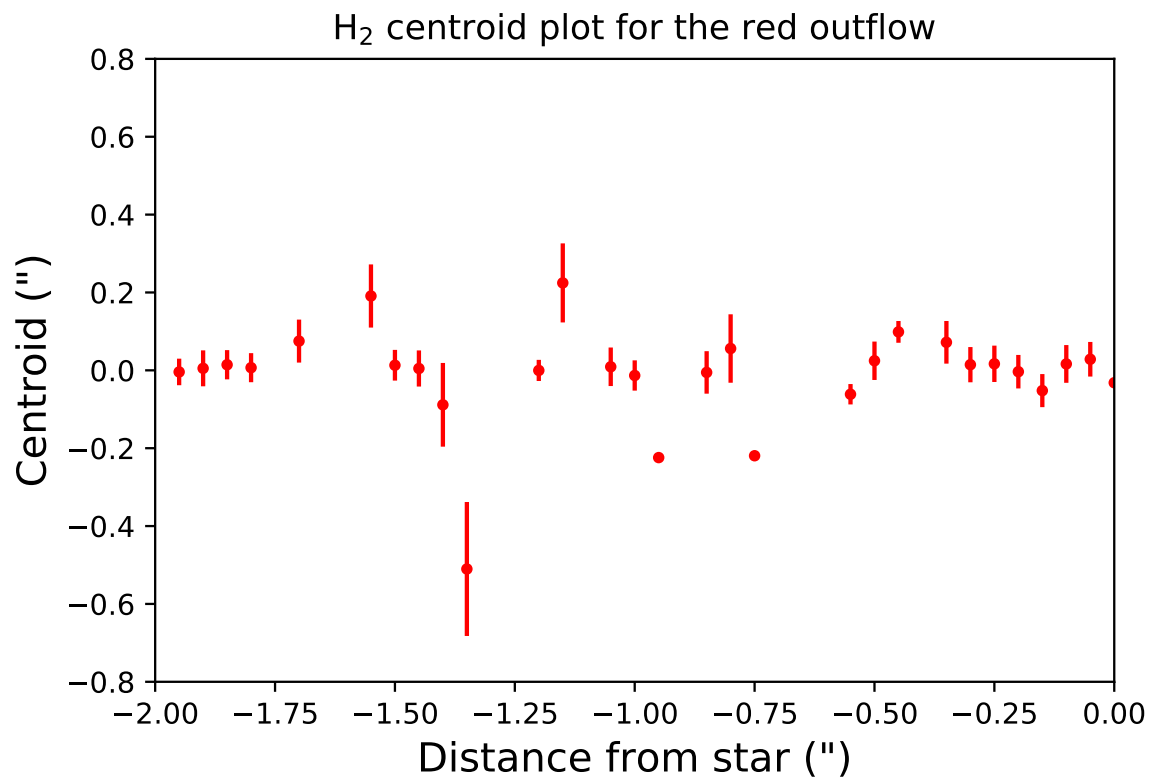
Figure 4.20: Centroids as a function of distance from the star for the red-shifted H_2 outflow, over the total velocity range.

4.7 Discussion

In this section, the morphology of the RW Aur jet has been discussed, the results of which are summarised below.

A number of PVD have been presented, which point towards the existence of an X-Wind being the driving force behind the jet. As expected, Brγ was not resolved spatially extended, which is in contrast to H_2, demonstrating their processes of origin (accretion and outflow respectively) being different from one another.

It has been shown that the jet is spatially extended between $\pm 0.8"$ in the main body of the jet with an extended knot seen in [Fe II] 1.644μm $\sim$ 1.69" away from the blue shifted component, which has been found to have a proper motion of 0.166 $\pm$ 0.009 arcsec/year. In the case of the red component, the proper motions were found to be 0.252 $\pm$ 0.079 arcsec/year & 0.305 $\pm$ 0.040 arcsec/year slightly lower than that of previous observations.

Collimated emission was observed for a number of [Fe II] lines, excluding the blue component of [Fe II] 1.665μm. The opening angle of the jet was measured using [Fe II] 1.644μm and was found to be $8.5 \pm 2.9°$ in the blue component and $10.2 \pm 2.3°$ in the red component. The opening angle of the H_2 outflow was also measured using the red component and found to be $21.5 \pm 9.5°$. These measurements are higher than previously observed optical measurements of $\leq 6°$ (Woitas et al. (2002), Dougados et al. (2000), Hirth et al. (1994)) indicative of the onion layer structure discussed earlier.

Evidence of wiggling has been observed in both the blue and red jet, with wiggling also observed in the H_2 outflow (with a lower SNR compared to the [Fe II] emission lines). This will be examined later in chapter 6.

5 Diagnostics of the Jet

In this chapter, diagnostics such as the mass accretion and mass-loss rates and the density of the jet for the RW Aur A system are outlined.

5.1 Mass Accretion Rate

To measure the mass accretion rate, the flux calibrated Brγ line was integrated to get the observable flux, and was measured to be 6.8×10^{-17} Wm^{-2}. This however had to be corrected for interstellar extinction. `PyNeb.RedCorr` was used with the correction law defined by Cardelli et al. (1989) and with a standard extinction law of R$_v$ = 3.1 (Mooley et al. (2013) and Kraus et al. (2017)). The two lines used to determine A$_v$ and thus the correction factor were the [Fe II] 1.553 and 1.677μm with an intrinsic ratio of 1.22 (Giannini et al. 2014).

The observed ratio for each pixel was found to create an observed ratio map, a sigma clipping routine ($\sigma = 5$) was used on the ratio map to remove outliers and a histogram of the observed ratios was produced (Figure 5.1). Taking the median of the histogram to be $\sim$1.08, this was then used as the observed ratio for `PyNeb.RedCorr`. Thus producing a corrected Brγ flux of 1.11×10^{-16} Wm^{-2} with A$_v$ = 4.6, this A$_v$ value is considerably higher than previous observations of 0.3 — 3 (Dodin et al. (2019), Bozhinova et al. (2016) and Antipin et al. (2014)), if instead of calculating the ratio pixel by pixel and using the integrated flux ratio A$_v$ is found to be 4.7 - still higher than previous observations. Combining the corrected Brγ flux with Eq. 2.2 and 2.5 gives a mass accretion rate of 1.14×10^{-08} M$_\odot$yr^{-1}. The uncertainties are derived from those intrinsic to the equations in Eq. 2.2 and 2.5 and the uncertainty of the fitting routine. Expressed in log scale, this gives -7.94 $\pm$ 1.56.
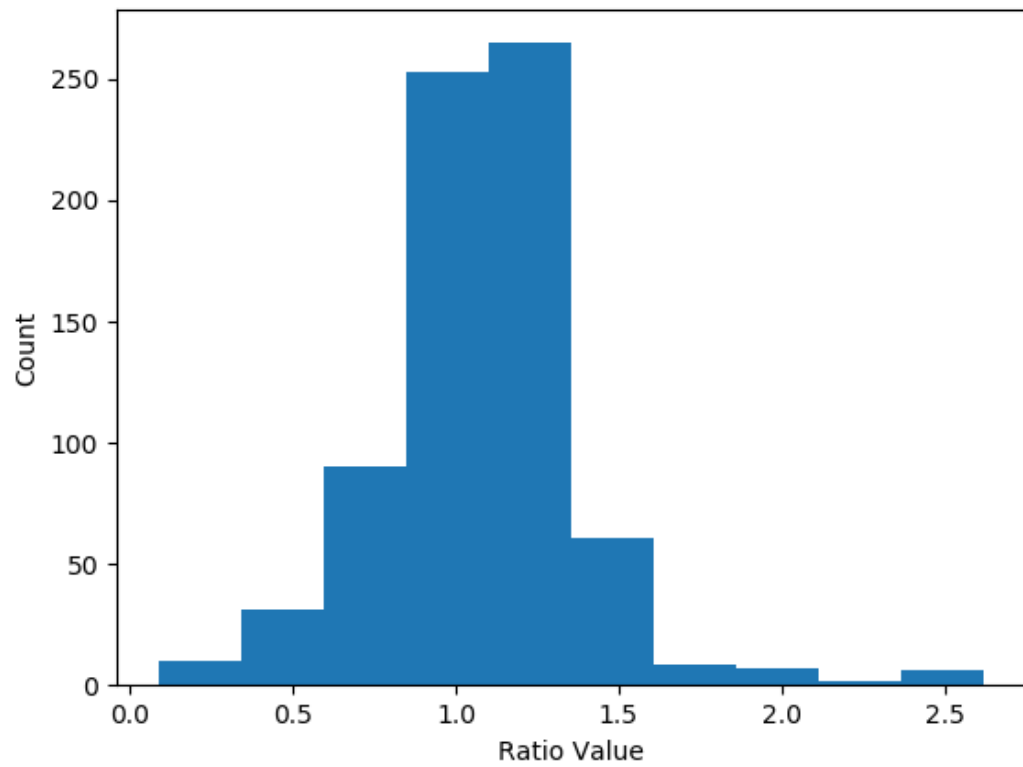
Figure 5.1: Histogram for the post sigma clipping routine of the ratio values.

The mass accretion rate of RW Aur A has been measured a number of times previously. Table 5.1 contains a literary review of measurements for the mass accretion rate from 1999-2016. When looking on a logarithmic scale and taking into account (the rather large) error bar, it is clear that the mass accretion rate lies within the region of previous measurements. However, it is possible to improve this result further. By using the improved a, b coefficients from Table B.1 of Alcalá et al. (2017) (1.19 ± 0.1 & 4.02 ± 0.51 respectively), the uncertainty on the mass accretion rate reduces to -8.07 ± 0.91. The plot for which can be seen in Figure 5.2.

Following from § 2.2.1, parameters relating to the accretion column have been derived and can be found: $f_\star = 0.09$, $\zeta = 3.01 \times 10^{11}$ erg cm^{-2}s^{-1} and $\nu = 443.42$ km s^{-1}.

Date	M$_\odot$yr^{-1}	Derived Using	Reference
2016 Sep 30	2×10^{-8}	Brackett Gamma	Koutoulaki et al. (2019)
2015 Mar 19	4.07×10^{-8}	Number of lines	Facchini et al. (2016)
2011 Mar 25	1.99×10^{-8}	Near ultraviolet and optical	Ingleby et al. (2013)
2005 Oct 22	1.4×10^{-7}	Brackett Gamma	Beck et al. (2010)
2002 — 2004	3.1×10^{-8}	Assumed Parameters	Akeson et al. (2005)
1999-2003	4.78×10^{-7}	Various Optical	White & Hillenbrand (2004)
1996 Dec 6	3.16×10^{-8}	Hα	White & Ghez (2001)

Table 5.1: Literature summary of the mass accretion rates over time, with the method of derivation included. In the case of Facchini et al. (2016), an average value across a number of lines was taken. For Ingleby et al. (2013), near ultraviolet and optical shock models are used.
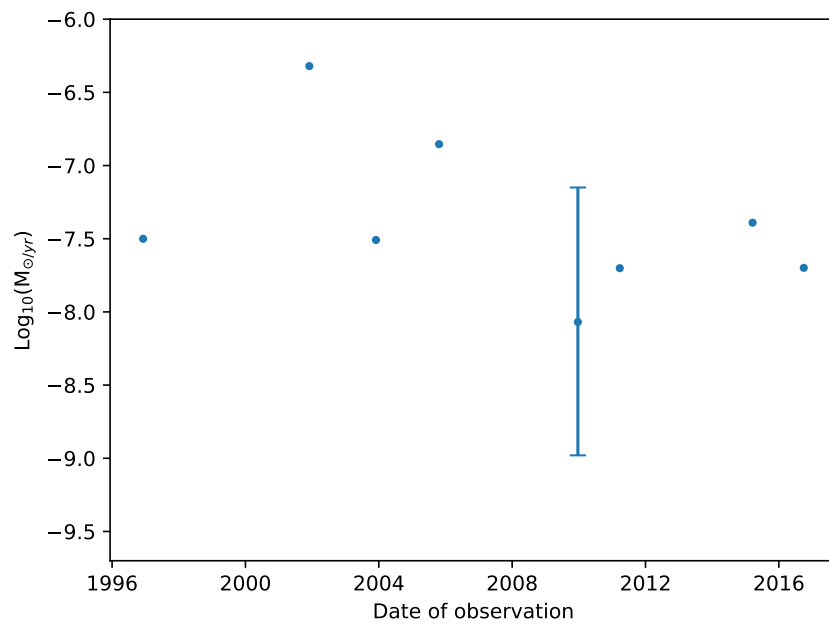
Figure 5.2:   Plot of the mass accretion rate measured compared to literature measurements, using the newest a, b coefficients from Alcalá et al. (2017).

5.2   Mass-Loss Rate for the [Fe II] Flow Component

A brief overview of the methods used to determine the mass-loss rate are outlined below, with further explanation found in Davis et al. (2011) and Fedriani et al. (2019). For N_{H} (Eq. 5.1), the flow component's area (a in steradians) is assumed to be equal to the extent of the flow along the jet axis multiplied by the width of the flow in steradians, with A_v being taken from earlier in the chapter.

$$N_H = 7.03 \times I_{[FeII]} 10^{A_v/14.4} \times 4/(a\pi)$$ (5.1)

For the blue and red component of the RW Aur jet, $I_{[\mathrm{Fe\ II}]}$ is defined by:

$$\mathrm{I}_{[\mathrm{Fe\ II}]} = \sum_i \mathrm{I}_{[\mathrm{Fe\ II}]_i}$$ (5.2)

where $I_{[\mathrm{Fe\ II}]_i}$ is the intensity of each [Fe II] emission line found in the knot. This was found by summing over the knot's area, creating a 1-D spectrum with each [Fe II] emission and fitting a Gaussian to it (Figure 5.3 — 5.5). These Gaussians were then integrated over using `SciPy.integrate.quad`, these three lines were chosen as an approximate estimate for the total [Fe II] as they make up the vast majority of the [Fe II] emission. This process was then repeated for red emission.
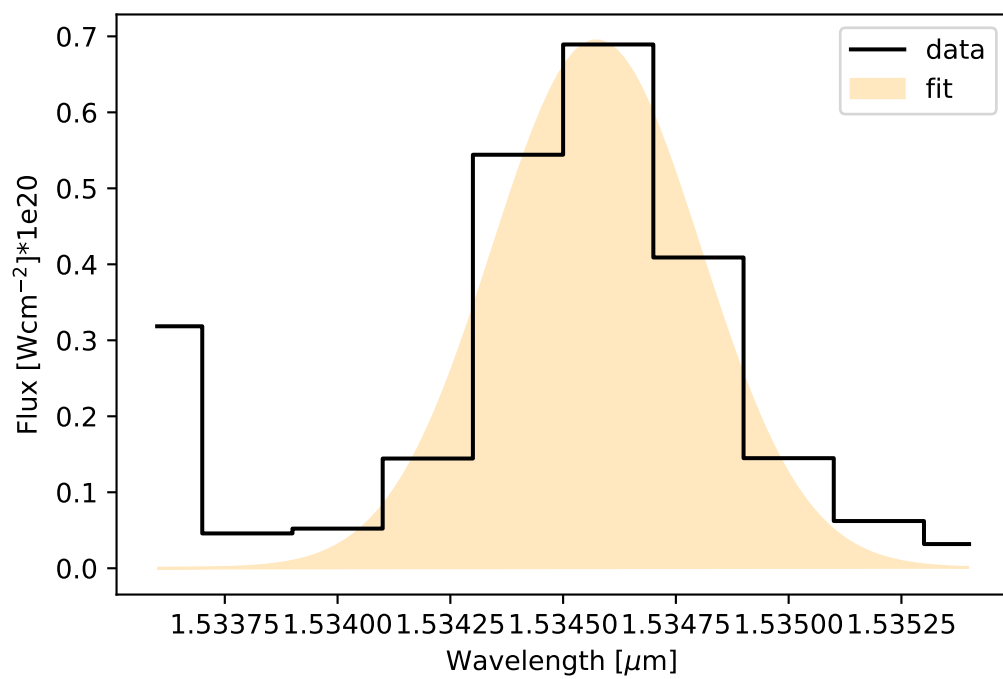
Figure 5.3: Spectrum for the blue [Fe II] 1.533μm emission with the fitted Gaussian plotted on top.
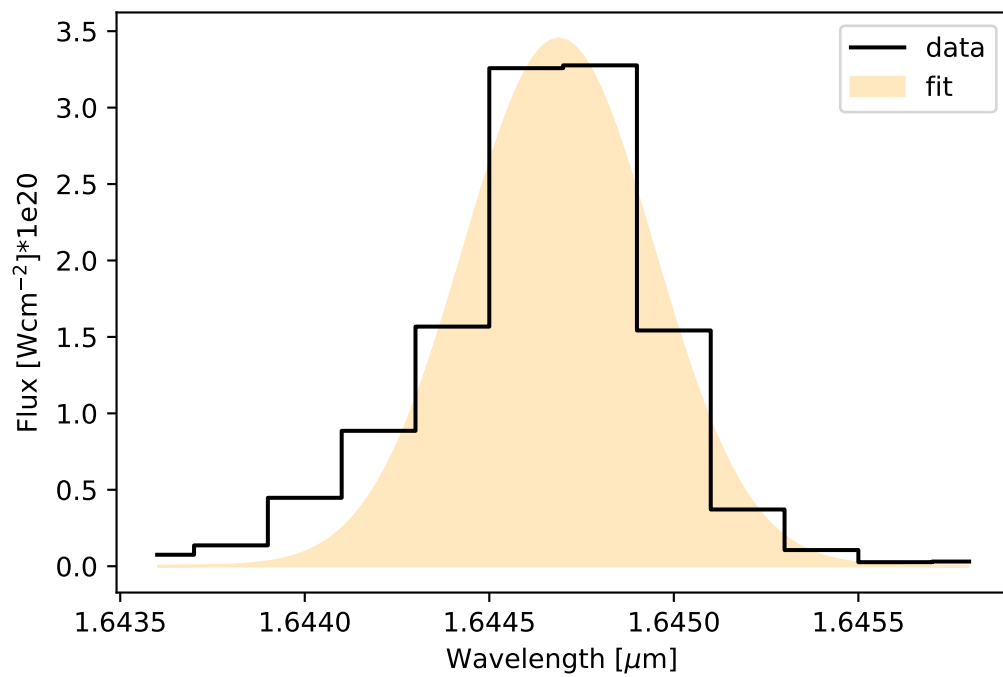
Figure 5.4: Spectrum for the blue [Fe II] 1.644μm emission with the fitted Gaussian plotted on top.
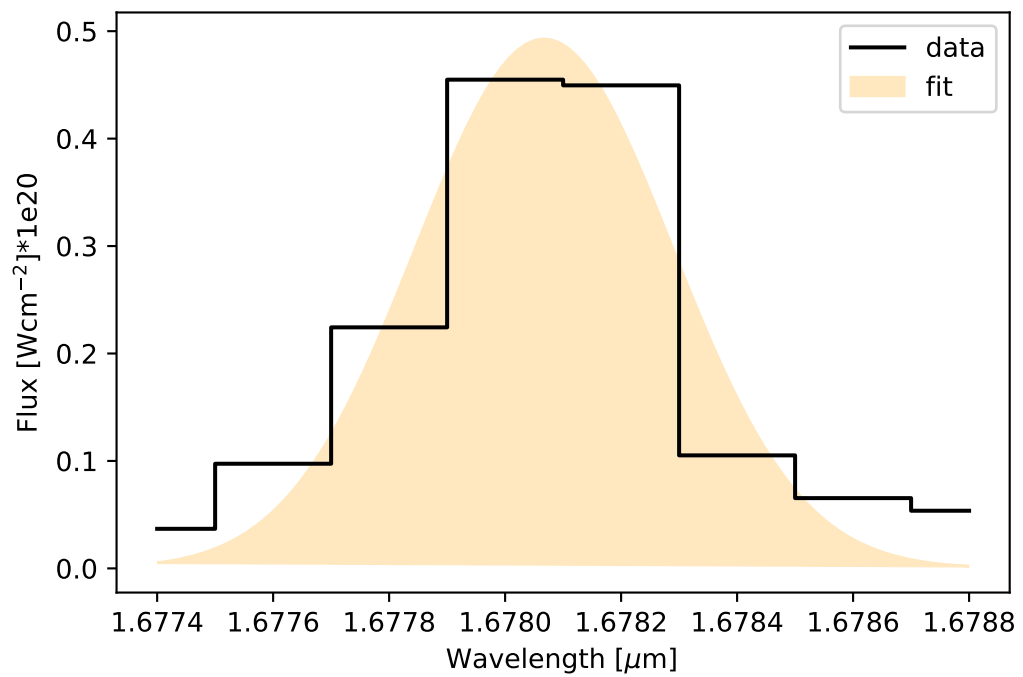
Figure 5.5: Spectrum for the blue [Fe II] 1.678μm emission with the fitted Gaussian plotted on top.

The mass of the flow component is found by multiplying the column density by the flow component's area (m^2) and the mass of atomic hydrogen (Eq. 5.3).

$$M = m_H a N_H \tag{5.3}$$

Finally, the mass-loss rate is found using the mass of the flow component, the tangential velocity and the length of the flow component (Eq. 5.4).

$$\dot{M_j} = \frac{M v_\perp}{l_\perp} \tag{5.4}$$

For the red jet (taking the component velocity to be 0.251 arcsec/year), $\dot{M_j}$ was found to be 1.544×10^{-9} M$_\odot$yr^{-1} with the jet efficiency found to be $\sim 0.022 - 0.181$ ($\dot{M_j}/\mathrm{M_{acc}}$).

While for the blue jet the component velocity is taken to be 0.166 arcsec/year, resulting in $\dot{M_j}$ being found to be 1.022×10^{-9} M$_\odot$yr^{-1} with the jet efficiency found to be $\sim 0.015 - 0.120$ ($\mathrm{M_{acc}}/\dot{M_j}$).

5.3   Evaluating the Density of the Jet

In appendix A3.2, a number of [Fe II] line ratios are modelled. Unfortunately, none of the observed lines are particularly temperature sensitive between 3,000 — 10,000K (Davis et al. (2011), Bacciotti et al. (1996) and references therein). Previous measurements of the RW Aur jet found the temperature to be between 3,600K — 20,000K (Bacciotti et al. (1996), Coffey et al. (2008), Dougados et al. (2002), Berdnikov et al. (2017) and Lisse et al. (2022)). The upper range of these temperatures (15,000 — 20,000 from Lisse et al. (2022)) come with the caveat of having a density estimate two orders of magnitudes larger than previous observations. These temperature measurements are consistent with that of the X-Wind model discussed in §4. As a result, the temperature is taken as 7,500K.

The continuum was subtracted from the flux calibrated cubes, and then `numpy.trapz` was used to integrate each emission line. These 2-D data sets were divided into each other to create the relevant ratio images, with each pixel having its density calculated (source code: Appendix A1.2).

The resulting density maps can be seen in Figures 5.6b and 5.6c for the red jet and Figure 5.6a for the blue jet. The [Fe II] 1.533μm ratio was not included due to the OH line subtraction producing unrealistic values for the density. Since both of the measurements for the density in the red jet are similar in their distribution, it is reasonable to say that the likely outcome for the [Fe II] 1.533μm ratio is that it will be similar to that of the [Fe II] 1.678μm ratio.

Binning both sets of data and excluding non-physical results produces Figures 5.7a and 5.7b, with the median electron density of the red and blue jets to be $n_e \sim 18{,}000$ cm^{-3} and 19,500 cm^{-3} respectively.
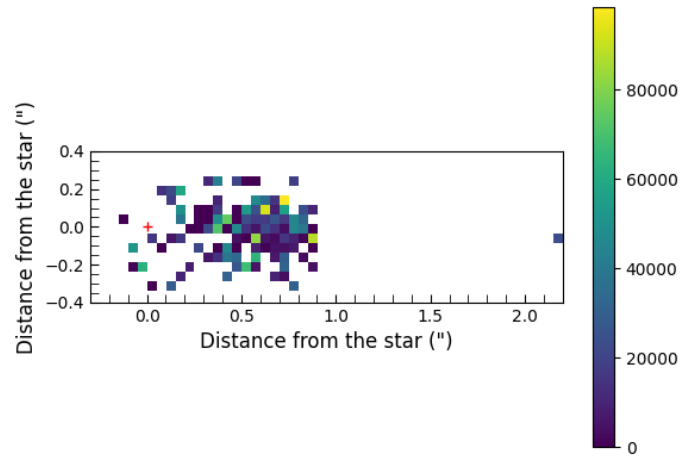
(a) Density map for 1.677μm$/1.644\mu$m in the blue jet.
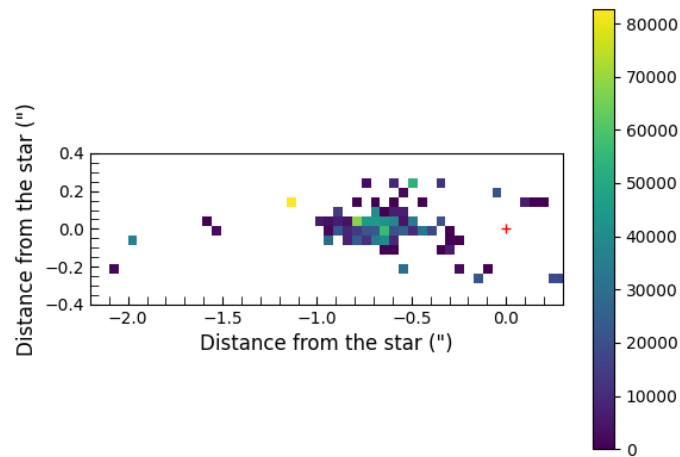
(b) Density map for 1.533μm$/1.644\mu$m in the red jet.
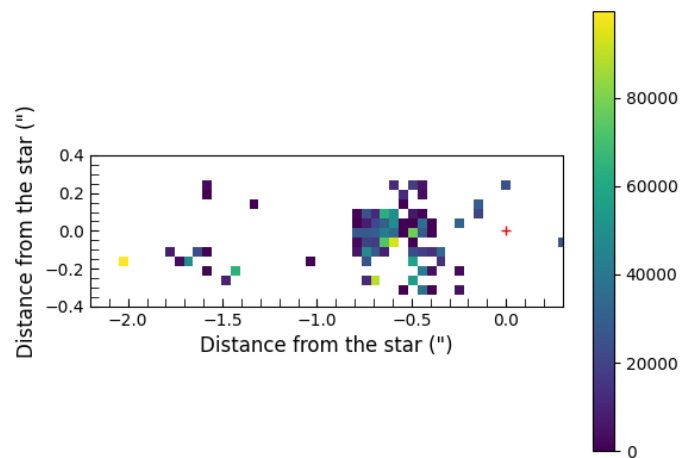
(c) Density map for 1.677μm$/1.644\mu$m in the red jet.

Figure 5.6: Density maps for the RW Aur jet, making use of the `PyNeb` modelled ratios with all measurements in units of n_e.
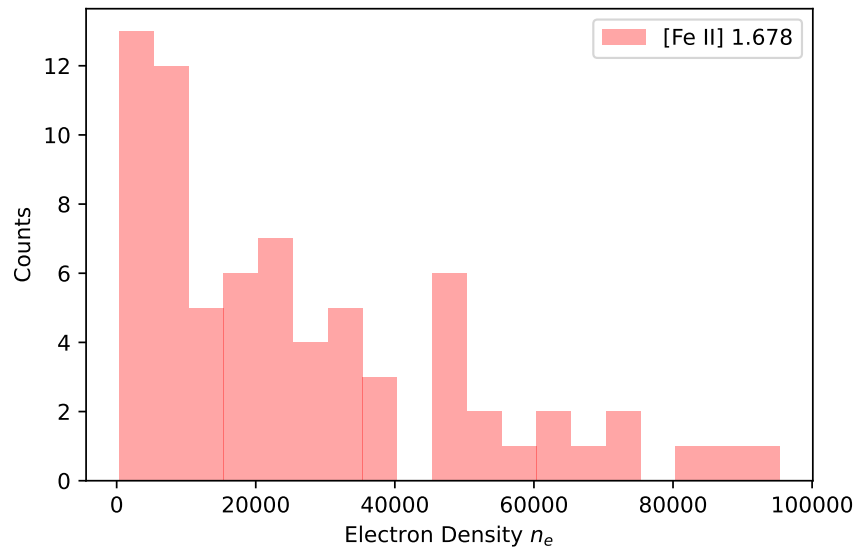
(a) Histogram of the density values in Figure 5.6a.
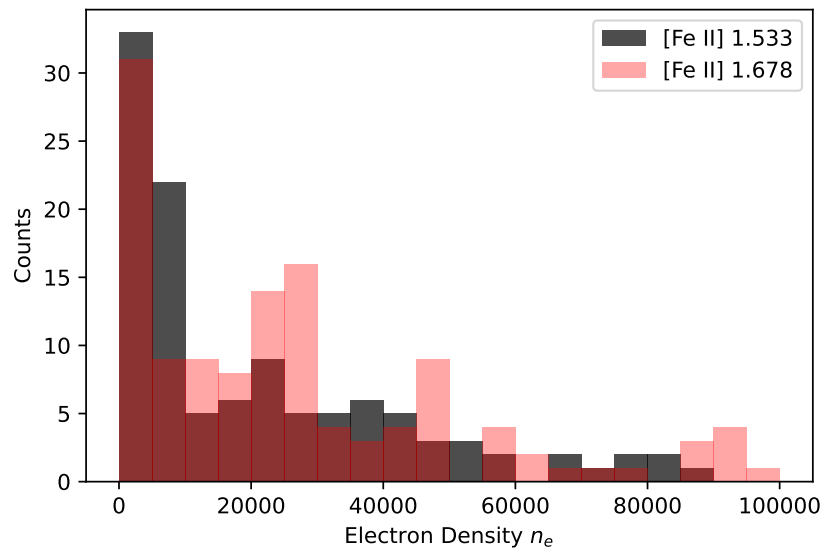
(b) Histogram of the density values in Figures 5.6b and 5.6c. The black bars indicate the electron densities derived from the [Fe II] $1.533/1.644\mu$m ratio, while the pink bars indicate electron densities derived from the [Fe II] $1.678/1.644\mu$m ratio.

Figure 5.7: Histogram for the density values for the blue and red component of the RW Aur jet.

5.4 Discussion

Previous measurements of A_v range from 0.3 — 3 (Dodin et al. (2019), Bozhinova et al. (2016) and Antipin et al. (2014)), this is significantly less than our measurement of 4.6. Such a dramatic variability in A_v has been observed in other CTTS; T Tau currently has $A_v \sim 1$, however, previous observations in the early 1900s observe A_v 2-3 magnitudes higher than the present day, this variation may be caused by in-homogeneous material surrounding the T Tau system with an abrupt clearing of the obscuring material (Beck & Simon (2001) and references therein).

The variability of RW Aur has been well studied, with a dusty wind being one of the main explanations for the variability. Observations carried out during one of RW Aur A's infamous dimming events showed that the mass accretion rate did not actually change (Chou et al. 2013). This is emphasised by our measurements that do not observe a significant change in the mass accretion rate when compared to other historic measurements. Rodriguez et al. (2013) proposed the 2010-2011 dimming event to be caused by an occultation of the RW Aur A, with simulations by Dai et al. (2015) suggesting the body of occulting dust being disrupted material bridging between RW Aur A and B ($\sim$ 100 AU wide) and providing predictions for further dimming events. This was supported by the simulation replicating observations by Cabrit et al. (2006). Multiband observations during 2014-2015 showed that the occulting material became steadily more gray as the dimming progressed, suggesting the body consists of small dust grains on the outside with the inner core being composed of large dust grains or dust enveloped in ice (Rodriguez et al. 2016). Therefore, this increase in extinction may be attributed to a dense dust region entering the line of sight between the observation and the system. The mass accretion rate of RW Aur A was measured to be 8.93×10^{-09} $M_\odot yr^{-1}$ or -8.07 $\pm$ 0.91 on a $\log_{10}$ scale, consistent with previous measurements (Table 5.1). The mass-loss rate were measured to be 1.544×10^{-9} $M_\odot yr^{-1}$

for the red jet and 1.022×10^{-9} $M_\odot yr^{-1}$ for the blue jet, with these results being consistent with of previous observations for RW Aur A (Melnikov et al. (2009), Liu & Shang (2012) & Dodin et al. (2019)). The jet efficiencies were found to be between $\sim$ 0.022 – 0.181 for the red jet and 0.015 – 0.120 for the blue jet, typical for protostellar objects (Lee 2020), thus pointing to the asymmetric nature of the RW Aur jet, with the red jet being more efficient in removing mass from the accretion column. However, these results are much lower than those of Melnikov et al. (2009), who measured the jet's efficiency to be $\sim$ 0.003 despite having similar mass outflow rates (4.6×10^{-9} $M_\odot yr^{-1}$). This measured comes with the caveat of using previous measurements of the accretion rate (1.6×10^{-06} $M_\odot yr^{-1}$ (Hartigan et al. 1995)), which is much higher than recent measurements. When taking the mass accretion rate to be 3.4×10^{-07} $M_\odot yr^{-1}$ (Valenti et al. 1993), the jet's efficiency increases by a factor of 5. It should be noted that this value for the mass accretion rate is still higher than all other measurements, barring that of White & Hillenbrand (2004).

The electron density measured for the red outflow in the RW Aur jet was found to be 18,000 cm^{-3}. Similarly, for the blue jet, the electron density was found to be 19,500 cm^{-3}. In Appendix A3.3, the densities were investigated for a range of temperatures (between 3,500 - 10,000K), densities were found to be 16,000 — 21,000 cm^{-3} for the blue jet, and 16,500 — 19,500 cm^{-3} for the red jet. In the case of the blue jet, blending with the Br12 emission (Figure 4.4) may have occurred, resulting in the results for the blue jet's density to be a lower estimate — further pointing to the asymmetric nature of the RW Aur jet.

6 Investigating The Wiggle

In §4.6, evidence for wiggling is seen in both the blue and the red jet. By combining the centroid plots for the blue and red jet onto one plot (Figure 6.1), a clear wiggling pattern is observed. To confirm this wiggling is real, the FWHM and centroid plots are compared against each other. In the case of the wiggling being caused by one of the outlined models, it is expected that there would be no significant relationship between them. When we compare the FWHM and centroid plots from the blue and red jet (Figure 6.2 and 6.3 respectively), we see that there appears to be no correlation between them.
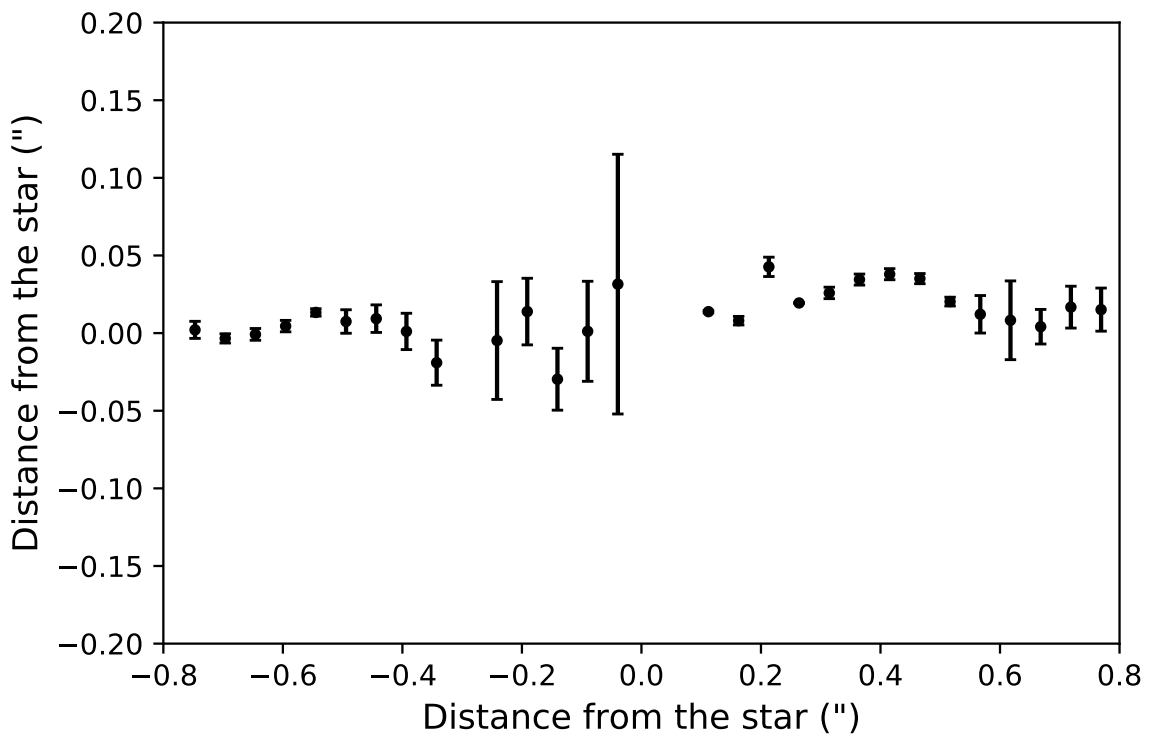
Figure 6.1: Combined [Fe II] 1.644 μm centroid plot for the RW Aur jet.

As outlined in §1.3.1, there are a number of possible origins for the wiggle in protostellar
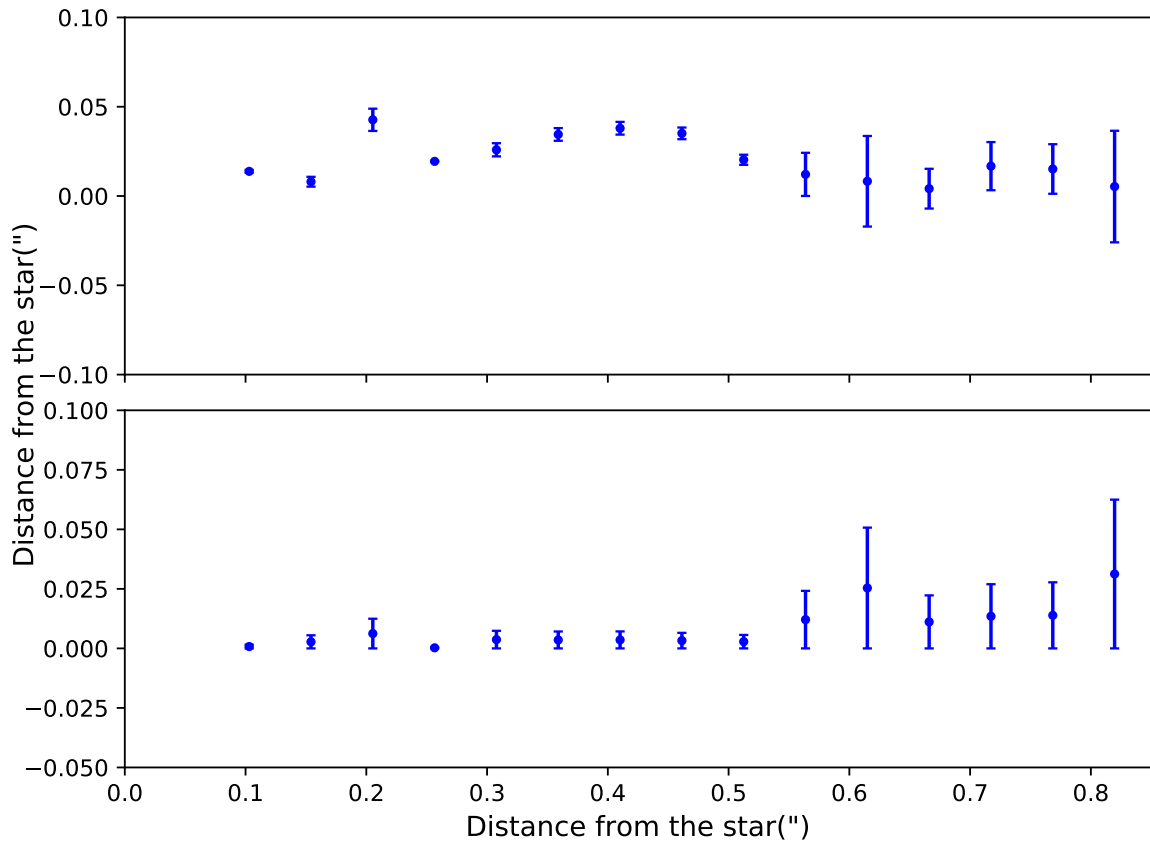
Figure 6.2: Centroid (top) and FWHM (bottom) [Fe II] 1.644 μm plots for the RW Aur blue jets.

jets. The first of these scenarios is that the wiggling observed is due to orbital motion of the jet around a binary companion (Anglada et al. 2007) – in the case of RW Aur A, there are suggestions for RW Aur A to have either an unseen brown dwarf or a Vesta sized companion (see §1.4).

Another possible scenario to be investigated is that the wiggling observed is caused by the precession of the jet axis caused by an interaction between the circumstellar disk and a companion which is orbiting in a different plane to that of the jet (Anglada et al. 2007).

It is possible to identify the source of the wiggle via the symmetric properties of the jet;
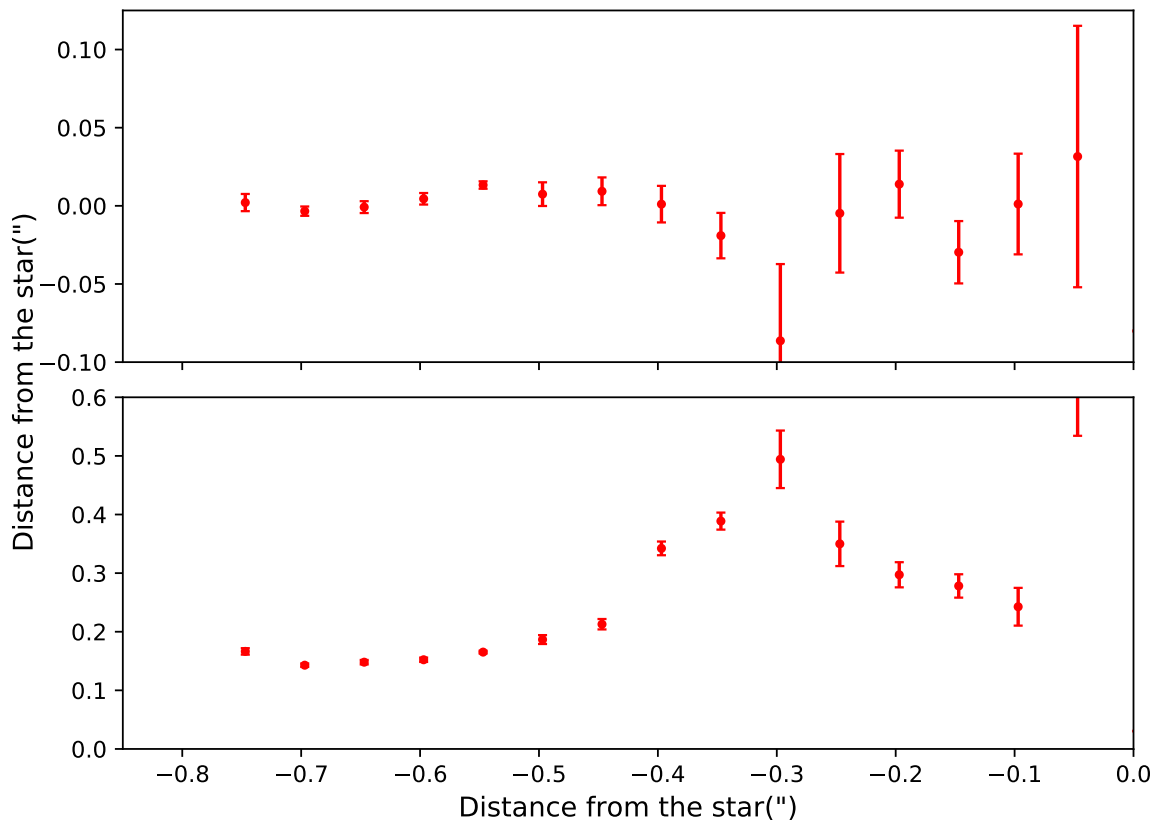
Figure 6.3: Centroid (top) and FWHM (bottom) [Fe II] 1.644 μm plot for the RW Aur red jets.

for an orbital model, it is expected that the jet will have a mirror-symmetric wiggle. While for the precession model, it is expected that the jet will have a point-symmetric wiggle (Murphy et al. 2021). Due to noise close to the source (6.1), this method of determination of the source of the wiggle is unavailable to be use. The following sections investigate these cases using standard methods (see Masciadri & Raga (2002) and Anglada et al. (2007) and references therein for full derivations) outlined below, and makes use of routines created by Murphy et al. (2021).

6.1   Orbital Motion

The first case to be considered is that the wiggling is caused by an orbital motion of a ballistic jet around a binary companion. The total systems mass (m) is defined to be:

$$m = m_1 + m_2 \tag{6.1}$$

Here, m_1 and m_2 are the masses of the jet source and the companion, respectively. A key relation related in the formulation of these models is the relation of the companions mass and the total system mass, this is defined by:

$$m_1 = (1 - \mu)m, \qquad m_2 = \mu m \tag{6.2}$$

The binary separation for the system (a) is defined in relation to the orbital radius of the jet source with respect to the system's centre of mass and is given by:

$$r_o = \mu a \tag{6.3}$$

and the orbital velocity (v_o) of the jet source is given by:

$$v_o = \frac{2\pi r_o}{\tau_o} \tag{6.4}$$

where τ_o is the orbital period. From here, the total system mass can be given by:

$$\frac{m}{M_\odot} = \mu^{-3}\left(\frac{r_o}{AU}\right)^3\left(\frac{\tau_o}{yrs}\right)^{-2} = \left(\frac{a}{\text{au}}\right)^3\left(\frac{\tau_o}{\text{yrs}}\right)^{-3} \tag{6.5}$$

When considering the jet's shape in the plane of the sky, its shape can be described by:

$$y = \kappa x \sin\left(\kappa\frac{x}{r_o} - \phi\right) + r_o\cos\left(\kappa\frac{x}{r_o} - \phi\right) \tag{6.6}$$

here, κ is the ratio of the orbital to jet velocity and ϕ is the phase angle of the sinusoid. If we can estimate these parameters from the jet shape, we use existing information of the jet velocity and total mass of the binary to estimate the orbital period τ and binary separation σ from Kepler's Third Law (Kirwan et al. 2022).

The parameters κ and r_o are related to the jets observables by:

$$\kappa = \tan\alpha \, \cos\theta \tag{6.7}$$

$$r_o = \frac{\lambda_x \tan\alpha}{2\pi} D \tag{6.8}$$

where, α is the half opening angle, θ is the inclination angle, λ_x is the angular distance between two maxima of the sinusoid and D is the distance from earth to RW Aur A. By substituting Eq. 6.7 and 6.8 into Eq. 6.6, we get:

$$y = |x|\tan\alpha\sin\left[\frac{2\pi}{\lambda_x}(|x| - x_o)\right] + \frac{\lambda_x}{2\pi}\tan\alpha\cos\left[\frac{2\pi}{\lambda_x}(|x| - x_o)\right] \tag{6.9}$$

where, x_o is defined to be the offset from the origin, in the plane of the sky and given by:

$$x_o = \frac{\lambda_x \phi}{2\pi} \tag{6.10}$$

Similarly to the precession model, the orbital model was fitted to the blue and red jets separately. For the blue jet (Figure 6.4), a companion mass of 0.23 $\pm$0.01 M$_\odot$ was found. While for the red jet (Figure 6.5), a companion mass of 0.16 $\pm$ 0.11 M$_\odot$ was found. Both of these results are consistent with Gahm et al. (1999). The full results can be seen in Tables 6.1 and 6.2
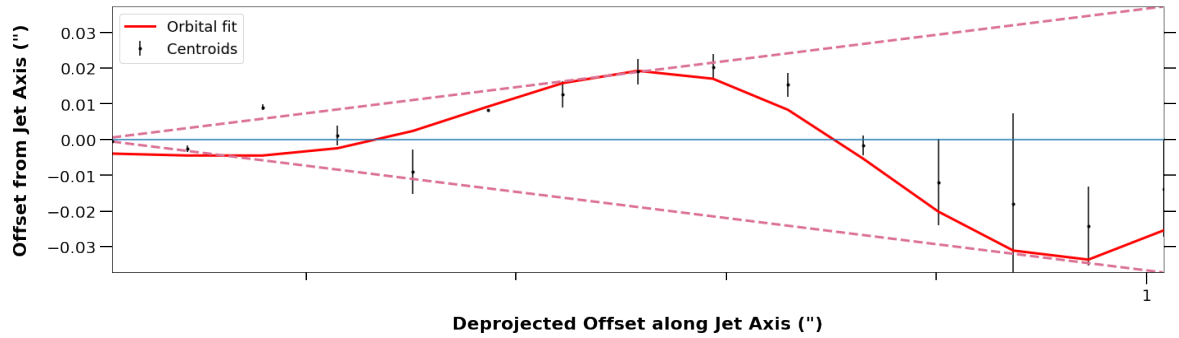
Figure 6.4: Fitted orbital model for the blue jet, where the dashed red line is the modelled opening angle. Error bars are derived using methods from 3.6. The parameters and their best fit values are given in Table 6.1.
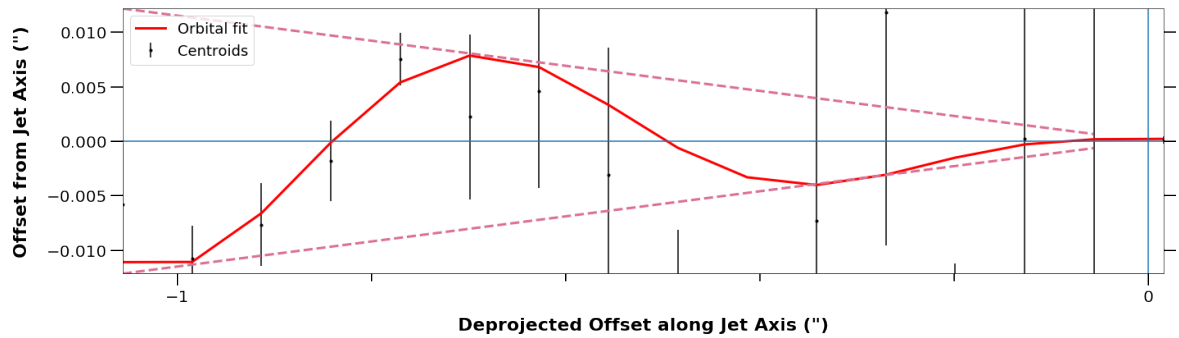
Figure 6.5: Fitted orbital model for the red jet, where the dashed red line is the modelled opening angle. Error bars are derived using methods from 3.6 The parameters and their best fit values are given in Table 6.2.

Parameter	Value
β	0.036 ± 0.003 °
λ	0.800 ± 0.025 "
a	2.85 ± 0.09 au
v_o	4.04 ± 0.13 km s^{-1}
m$_2$	0.23 ± 0.01 M$_\odot$

Table 6.1: Orbital parameters for the blue jet. Uncertainties have been derived from the fitting routine.

Parameter	Value
β	0.021 ± 0.014 °
λ	0.600 ± 0.053 "
a	1.78 ± 1.22 au
v_o	3.52 ± 2.42 km s^{-1}
m$_2$	0.16 ± 0.11 M$_\odot$

Table 6.2: Orbital parameters for the red jet, uncertainties have been derived from the fitting routine.

6.2   Jet Precession

The second case is the precession model; the jet's shape in the plane of the sky is given by (Masciadri & Raga 2002),

$$y = x\tan(\beta)\cos(\nu(t - \frac{x}{v_j\cos\beta})) \qquad \text{where } \nu = 2\pi/\tau_p \tag{6.11}$$

Here, v_j is the jet velocity. If the precession is due to an orbiting companion, there should be a smaller wiggle also present due to the orbital motion. We know the orbital motion must cause a smaller wiggle than the precession, giving us the condition:

$$v_o \leq v_j\tan\beta \qquad \text{where } v_o = \frac{2\pi r_o}{\tau_o} \tag{6.12}$$

This sets the maximum orbital velocity of the companion. Using Kepler's Third Law, we can obtain v_o as a function of μ (Anglada et al. 2007).

$$v_o = 2\pi(\frac{M_{\text{sys}}}{\tau_o})^{1/3}\mu \tag{6.13}$$

$$\frac{\tau_o}{\tau_p} = \frac{15}{32}\frac{\mu}{\sqrt{1-\mu}}\sigma^{3/s}\cos\beta \tag{6.14}$$

μ is the ratio of the companion mass to the total system mass, σ is the ratio of the disk radius to the binary separation, and β is the half opening angle of the precession. In most scenarios, this gives $\tau_p > 10\tau_o$ - we therefore expect to see precession wiggles on significantly longer timescales. This means that for a small-scale wiggle, orbital motion is more likely - if this is caused by precession then it implies an even smaller orbital motion wiggle and a correspondingly small orbit. Here it is assumed that $\sigma \sim 1$ and $\beta \sim i_p$ where, i_p is the angle between the orbital angular momentum vector of the companion and the rotation axis of the jet (Murphy et al. 2021).

The model was fit to the blue and the red jets separately. For the blue jet (Figure 6.6) the fitted parameters for the system match with that of Gahm et al. (1999), with a companion mass (m_2) of 0.08 ± 0.02 M$_\odot$ (compared to $0.07 \leq m_2 \leq 0.22$ from Gahm et al. (1999)). For the red jet (Figure 6.7), the results are not as clear-cut. Initially, the results look promising. However, there is no convergence in the optimisation routine used to determine μ. With the closest point being 0.045, producing a binary companion of m$_2 \sim 0.07 \pm 0.01$ M$_\odot$. When considering the errors, derived from `lmfit`, both of these are within the lower bound of Gahm et al. (1999).The full results can be seen in Tables 6.3 and 6.4.
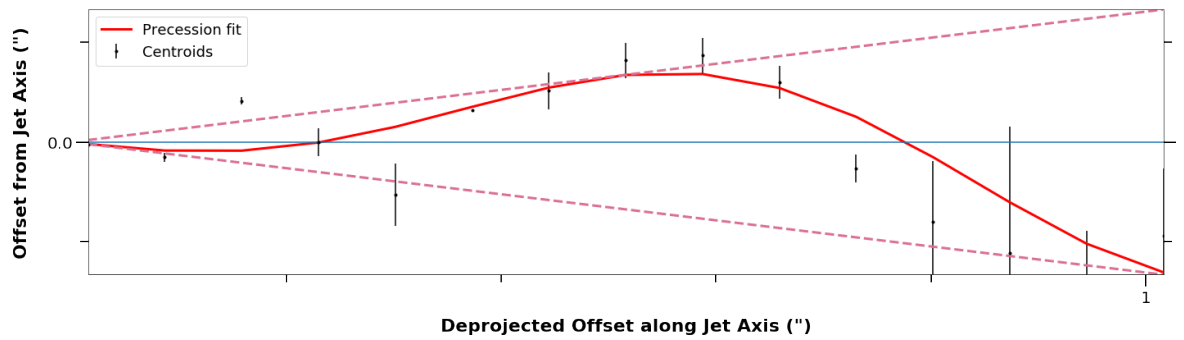
Figure 6.6: Fitted precession model for the blue jet, where the dashed red line is the modelled opening angle. Error bars are derived using methods from 3.6. The parameters and their best fit values are given in Table 6.3.
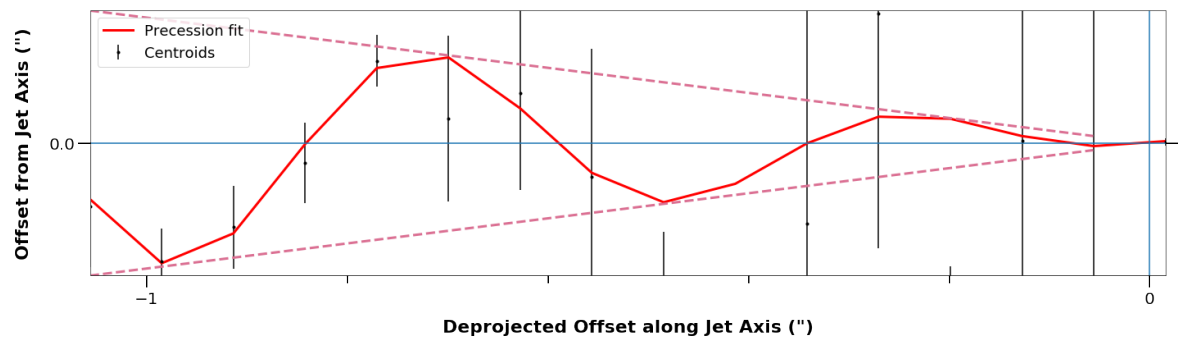
Figure 6.7: Fitted precession model for the red jet, where the dashed red line is the modelled opening angle. Error bars are derived using methods from 3.6. The parameters and their best fit values are given in Table 6.4.

Parameter	Value
β	0.026 $\pm$ 0.006 °
a	0.28 $\pm$ 0.07 au
τ_p	6.56 $\pm$ 1.63 years
τ_o	44.0 $\pm$ 11 days
m_2	0.08 $\pm$ 0.02 M$_\odot$

Table 6.3: Precession parameters for the blue jet. Uncertainties have been derived from the fitting routine.

Parameter	Value
β	0.011 $\pm$ 0.002 °
a	0.12 $\pm$ 0.02 au
τ_p	1.98 $\pm$ 0.31 years
τ_o	12.0 $\pm$ 1.9 days
m_2	0.07 $\pm$ 0.01 M$_\odot$

Table 6.4: Precession parameters for the red jet. Uncertainties have been derived from the fitting routine.

6.3   Discussion

Modelling the centroids for both a precession and orbital wiggle resulted in a companion between $0.07 - 0.23$ M$_\odot$, this result is in agreement with the RW Aur A's postulated brown dwarf companion (Gahm et al. 1999). In the case of the precession model, the binary separation ranges between 0.28 ± 0.07 and 0.12 ± 0.02 au while for the orbital model, the separation increases to 2.85 ± 0.09 and 1.78 ± 1.22 au. In the case of the precession model, these results are consistent with previous protostellar jet models (Murphy et al. (2021) and Erkal, Nisini, Coffey, Bacciotti, Hartigan, Antoniucci, Giannini, Eislöffel & Manara (2021)). The period for the precession model is consistent with that of Gahm et al. (1999) in that the orbital period parameters represent an *upper* bound for τ_o. It can be seen that for the red jet, both the companion mass and binary separations are lower than for the blue jet. As opposed to Lisse et al. (2022), the models could not reproduce a wiggle when considering a Vesta-sized companion. Modelling of the H$_2$ centroids was unable to produce realistic wiggling parameters and, as a result, was not included.

7   Conclusion and Future Work

The morphology of the RW Aur jet has been evaluated with the use of various PVD and spectro-images. It has been shown that the jet is spatially extended between $\pm$ 0.8" with an extended knot $\sim$ 1.69" away from the blue component. Similar to previous observations, Brγ has not been seen spatially extended in the jet, whereas with H_2, there is emission associated with the jet as opposed to a cavity as typically seen in protostellar systems. The proper motions have been found to be 0.166 $\pm$ 0.009 arcsec/year for the blue jet and 0.252 $\pm$ 0.079 and 0.305 $\pm$ 0.040 arcsec/year for the red. These measurements have been compared to and are in agreement with archival X-Shooter data.

A_v has been measured to be 4.6, higher than previous observations of 0.3 –3 3. This result may point to the dense dusty region impeding the line of sight. The mass accretion rate of RW Aur A has been measured to be 8.93 $\times 10^{-9}$ $M_{\odot}$/yr, with a mass loss rate of 1.544 $\times 10^{-9}$ $M_{\odot}$/yr for the red jet and 1.022 $\times 10^{-9}$ $M_{\odot}$/yr consistent with previous measurements. This agreement with previous accretion and outflow rate measurements shows that the cause in the change of extinction is independent of the accretion and outflow rates. Improvements to these measurements can be made by taking simultaneous optical and NIR measurements of the system to determine the mass accretion rate using separate line ratios (such as with [O I] and Brγ).

The electron density of the RW Aur bipolar jet was found (assuming a temperature of 7,500K) to be 19,500 cm^{-3} and 18,000 cm^{-3} for the blue and red jets respectively. Changing the temperature between 3,500 — 10,000 varies these densities from 16,000 — 21,000 for the blue jet and 16,500 — 19,500 for the red jet. Improvements to the diagnostic results can be made by taking observations of temperature sensitive [Fe II] lines, specifically Jbb observations (1.18 – 1.416 μm) and optical observations (centred

at 0.86 μm) along with Hbb observations which would allow for detailed temperature and density diagnostics by making use of the [Fe II] 0.862 μm/ 1.257 μm and [Fe II] 1.533 μm/ 1.644 μm ratios (Pesenti et al. 2003).

Modelling of the wiggle of the RW Aur jet has shown the possibility of a brown dwarf companion with mass ranging between 0.07 ± 0.01 and 0.08 ± 0.02 M$_\odot$ for the precession model and 0.16 ± 0.11 and 0.23 ± 0.01 M$_\odot$ for the orbital model, with the precession model producing orbital periods consistent with independent measurements using different methods of determination. Both models produce binary separations consistent with wiggle measurements from other protostellar system.

Further observations with a higher spatial resolution such as with MUSE or ideally with JWST would allow for a greater accuracy and allow for getting as close to the jet source as possible.

Appendices

A1 Source Code

A1.1 OSIRIS.py

```python
#!/usr/bin/env python3
# -*- coding: utf-8 -*-


'''
Simple script to perform a baseline subtraction on an
OSIRIS cube
Thanks to Andrew Miller, Star Formation Group,
Experimental Physics, Maynooth University
for the assistance
'''
from astropy.io import fits
from astropy.wcs import WCS
import numpy as np
import sys
import warnings
import argparse
import astropy.units as u
from tqdm import tqdm
# suppress UnitsWarning from some cubes
from astropy.utils.exceptions import AstropyWarning
import matplotlib.pyplot as plt
```

```python
from astropy.stats import SigmaClip
from photutils import Background2D, MedianBackground, StdBackgroundRMS

def parse_arguments():
    parser = argparse.ArgumentParser(description = head())
    parser.add_argument('infile', help = "filename of data cube",
                        type = str)
    parser.add_argument('-lmin', help = "lower wavelength
                        boundary for masked region",
                        type = float)
    parser.add_argument('-lmax', help = "upper wavelength
                        boundary for masked region",
                        type = float)
    parser.add_argument('-refspec', help = 'reference spectrum
                for scaling and '
                        'subtraction (in y x order)', nargs='+',
                        type = int)
    parser.add_argument('-outfile', help = "filename of the
                        output subcube",
                        type = str)
    return parser.parse_args()
    def head():
    print ("\nA script to generate a subcube
            from an OSIRIS datacube using a background")
    print ("subtraction routine developed for IFU data.
            Optionally, the cube can be ")
    print ("truncated before subtraction to limit runtime.
            If no {outfile} is given,")
```

```python
    print ("one will be generated.")

    print ("")

def quick_plot(fname, index):

    #plt.ion()

    print("we're in quickplot!")

    print('You asked for index', index)


    try:

        data = fits.open(fname)[0].data

        print(data.shape)

    except Exception as e:

        print(e)

        data= fits.open(fname)[1].data

        print(data.shape)

    def update_spec(hl, data, y,x):

        xarr = np.arange(data.shape[0])

        spec = data[:, y, x]

        hl.set_xdata(np.append(hl.get_xdata(), xarr))

        hl.set_ydata(np.append(hl.get_ydata(), spec))

        plt.draw()

    def implot(data, index):

        global coords

        coords = []

        def on_click(event):

                #global ix, iy

            xc, yc = event.xdata, event.ydata

            # ix, iy = event.xdata, event.ydata
```

```python
            print(yc, xc)
            coords.append((int(yc), int(xc)))
        def on_key(event):
            if event.key == 'a':#'ctrl+p':
                print('Enabling point-selection mode...')
                cid = fig.canvas.mpl_connect('button_press_event'
                    , on_click)
            if event.key == 'd': #'ctrl+q':
                print("Point-selection mode disabled.")
                cid = fig.canvas.mpl_connect('button_press_event'
                    , on_click)
                fig.canvas.mpl_disconnect(cid)
                #plt.disconnect(cid)
        fig, ax = plt.subplots(figsize = (8, 8))
        ax.imshow(data[index], origin = 'lower', vmin = 0,
                vmax = 3)
        cid = fig.canvas.mpl_connect('key_press_event', on_key)
        plt.show()
    def specplot(data, coords):
        print('Plotting chosen spectrum...')
        fig, ax = plt.subplots(figsize = (9,5))
        y, x = coords[0]
        xarr = np.arange(data.shape[0])
        spec = data[:, y, x]
        bkg = get_masked_background(spec, lbdas=0)
        ax.plot(xarr, spec)
        ax.plot(xarr, bkg)
```

```python
        ax.set_title(f'Reference spectrum = ({y}, {x})')
        plt.show()

    implot(data, index)
    if coords != []:
        specplot(data, coords)
    while True:
        query = input('Does this look okay? y/n ')
        if query.lower() == 'n':
            implot(data, index)
            if coords != []:
                specplot(data, coords)
        if query.lower() == 'y':
            y, x = coords[0]
            return data[:, y, x]
def load_cube(fname):
    '''just so I don't have to keep writing it'''
    with warnings.catch_warnings():
        warnings.simplefilter('ignore', AstropyWarning)
        try:
            ffile = fits.open(fname)[0]
        except Exception:
            ffile = fits.open(fname)[1]

    unit = ffile.header.pop('CUNIT3')
    # make a wcs object
    wcs = WCS(naxis=1)
    crval = (ffile.header['CRVAL3'] * u.Unit(unit)).to(u.angstrom)
```

```
    cdelt = (ffile.header['CDELT3'] * u.Unit(unit)).to(u.angstrom)

    wcs.wcs.crpix = [ffile.header['CRPIX3']]

    wcs.wcs.crval = [round(crval.value, 1)]

    wcs.wcs.cdelt = [round(cdelt.value, 1)]

    cube = ffile.data

    return cube, wcs

def sort_boundaries(cube, wcsobj, lmin = None, lmax = None):

    '''Figure out the boundaries'''

    #cube = load_cube(fname)


    if lmin is not None:

#        l1 = cube.wave.pixel(lmin, nearest = True)

        l1 = (wcsobj.wcs_world2pix(lmin, 0)[0] + 0.5).astype(int)

        if l1 < cube.shape[0]:

            l1 = 0

#        lmin = cube.wave.coord(l1)

        lmin = wcsobj.wcs_pix2world(l1, 0)[0]

    else:

        lmin = wcsobj.wcs_pix2world(0, 0)[0]


    if lmax is not None:

        l2 = (wcsobj.wcs_world2pix(lmax, 0)[0] + 0.5).astype(int)

        if l2 > (cube.shape[0] - 1):

            l2 = cube.shape[0] - 1

        lmax = wcsobj.wcs_pix2world(l2, 0)[0]

    else:

        lmax = wcsobj.wcs_pix2world(cube.shape[0]-1, 0)[0]
```

```python
    #print(lmin, lmax)

    return lmin, lmax


def mask_threshold(image, sigma):
    '''Mask values below -3sigma? or set them to 0?'''
    thresh = -3 * sigma
    data = image.copy()
    for y, x in np.ndindex(*image.shape):
        if data[y, x] < thresh:
            data[y, x] = np.nan
    return data

def get_background_rms(data, sigma = 3, N = 10, mask = None):
    '''
    Get the background rms/sigma value of the data.
    Use this for cutoff values in the data?


    Parameters
    ----------
    data : `np.ndarray` or `np.ma.MaskedArray`
        the data to be plotted
    sigma : int
        the sigma value sent to `SigmaClip`.
        data above or below sigma stddevs
        will be ignored in computing the background RMS;
        default is 3.
    N : int
        the number of sampling boxes to fit in the data.
```

```
    Default is 10. if the

    box sizes are a non-integer value,

    then the `edge_method` keywork used

    in `Background2D` is set to "pad"
mask : `np.ma.MaskedArray` or None

    if no mask is specified,


'''


# get a boxsize. sides must be integer values,
    so if there's a
# remainder then set an edge_method keyword
ny, nx = data.shape
sy = ny // N
sx = nx // N


if (ny % N != 0) or (nx % N != 0):
    edge_method = 'pad'
else:
    edge_method = None


# is there a mask?
if mask is None:
    try:
        mask = data.mask
    except Exception:
        mask = ~(np.isfinite(data))
```

```
    else:

        mask = mask


    # do we need to unmask the data?

    try:

        ndata = data[~data.mask]

        if ndata.shape != data.shape:

            ndata = ndata.reshape(data.shape)

    except Exception:

        ndata = np.ma.getdata(data)


    # get the background RMS. This calls

    `photutils.Background2D`

    sigma_clip = SigmaClip(sigma=sigma)

    bkg_estimator = MedianBackground()

    rms_estimator = StdBackgroundRMS()

    bkg = Background2D(ndata, (sy, sx), filter_size = (5,5),

                      sigma_clip = sigma_clip,

                      bkg_estimator = bkg_estimator,

                      bkgrms_estimator = rms_estimator,

                      mask = mask, edge_method = edge_method)


    sigrms = bkg.background_rms_median

    return sigrms

def mask_peaks(sp, lvals, unit = None, wcs = None): #deg = None,

    '''

    Simple function for masking regions of an array
```

```
Parameters:
--------------
sp : `np.ndarray`
    Array of spectral or spatial data you want to fit
lvals : list, tuple, or `np.ndarray`
    min and max values of the region or regions you want to mask
unit : bool or NoneType
    the unit-type of the values for the masking region.
    None by default, which treats lvals as pixel values;
    if True, the unit is assumed to be a wavelength
wcs : NoneType, or `astropy.wcs.WCS` object
    if no unit is specified, the wcs is unnecessary;
    if lvals are passed as wavelength values,
    specify a WCS object to handle the wavelength values
'''


spec = np.ma.array(sp)
lvals = np.asarray(lvals)
nrows = lvals.ndim


if unit is not None:
    # check for WCS info
    assert wcs, "Need WCS info for wavelength values"


    # set wavelength values as a masked array
    w = np.ma.array(wcs.wcs_pix2world(np.arange(len(spec)), 0))[0]
```

```python
        if nrows == 1:
            lmin, lmax = wcs.wcs_world2pix(lvals, 0)[0]
            lmin = max(0, int(lmin - 0.5))
            lmax = max(0, int(lmax + 0.5))
            spec[lmin:lmax] = np.ma.masked
        else:# (nrows > 1):
            for row in range(nrows):
                lmin, lmax = wcs.wcs_world2pix(lvals[row], 0)[0]
                lmin = max(0, int(lmin - 0.5))
                lmax = min((spec.shape[0]-1), int(lmax + 0.5))
                spec[lmin:lmax] = np.ma.masked
    else:
        w = np.ma.arange(len(spec))
        if nrows == 1:
            lmin, lmax = lvals
            lmin = max(0, lmin)
            lmax = min((spec.shape[0]-1), lmax)
            spec[lmin:lmax] = np.ma.masked
        else:
            for row in range(nrows):
                lmin, lmax = lvals[row]
                lmin = max(0, lmin)
                lmax = min((spec.shape[0]-1), lmax)
                spec[lmin:lmax] = np.ma.masked


    # select only non-masked portion of the arrays
```

```
    mask = ~spec.mask

    s = spec[mask]

    w = w[mask]

    return s, w

def mask_poly(data, deg = None):


    '''

    Module to find normalised polynomial fits. Called by `mask_fit()`


    Parameters:
    -----------
    data : tuple
        masked arrays of normalised spatial and wavelength data
    deg : int or NoneType
        degree of polynomial to fit


    Returns:
    ------------
    pfit : `np.poly1d` object
        polynomial coefficients
    '''
    # normalise the wavelength/spatial axis?
    s, w = data
    deg = 4 if deg is None else deg #Here


    w0 = w.min()
    dw = w.max() - w0
```

```
    w = (w - w0) / dw


    pfit = np.polyfit(w, s, deg)
    pval = np.polyval(pfit, w)


    return pfit

def mask_fit(sp, lvals, deg = None, unit = None, wcs = None):
    '''
    Convenience function for fitting continua.
    Inspired by the IRAF
    functionality which excludes specified
    regions from polynomial fit.


    Parameters:
    ---------------
    sp : `np.ndarray`
        The spectrum or spatial profile you want to fit
    lvals : `np.ndarray`, list, or tuple
        The pixel or wavelength range(s) to exclude from the fit
    deg : int or NoneType
        Degree of the polynomial fit; probably best to keep it <5
    unit : `astropy.units.Quantity` or NoneType
        input type of lvals; None by default,
        which assumes pixel input
        if not None, must be ie `u.angstrom`
        to specify wavelength ranges
    wcs : `astropy.wcs.WCS` object or NoneType
```

```
        None by default; if `unit` kwarg is not None,

        a WCS file must be

        given to figure out wavelength information

    Returns:

    ---------------

    sfit : `np.poly1d` object

        the spectrum/spatial fit

    '''

    nx = len(sp)

    nrange = np.arange(nx)

    n = wcs.wcs_pix2world(nrange, 0)[0] if wcs else nrange

    w0 = n.min()

    dw = n.max() - w0

    w = (n - w0) / dw

    data = mask_peaks(sp, lvals, unit, wcs)

    #print(data)

    z = mask_poly(data, deg)

    sfit = np.polyval(z, w)

    return sfit

def mask_fit(sp, lvals, deg = None, unit = None, wcs = None):

    '''

    Convenience function for fitting continua. Inspired by the IRAF

    functionality which excludes specified regions from polynomial fit.


    Parameters:

    ---------------

    sp : `np.ndarray`
```

```
        The spectrum or spatial profile you want to fit
    lvals : `np.ndarray`, list, or tuple
        The pixel or wavelength range(s) to exclude from the fit
    deg : int or NoneType
        Degree of the polynomial fit; probably best to keep it <5
    unit : `astropy.units.Quantity` or NoneType
        input type of lvals; None by default, which assumes pixel input
        if not None, must be ie `u.angstrom` to
        specify wavelength ranges
    wcs : `astropy.wcs.WCS` object or NoneType
        None by default; if `unit` kwarg is not None,
        a WCS file must be
        given to figure out wavelength information


    Returns:
    ---------------
    sfit : `np.poly1d` object
        the spectrum/spatial fit
    '''
    nx = len(sp)
    nrange = np.arange(nx)
    n = wcs.wcs_pix2world(nrange, 0)[0] if wcs else nrange
    w0 = n.min()
    dw = n.max() - w0
    w = (n - w0) / dw
    data = mask_peaks(sp, lvals, unit, wcs)
    #print(data)
```

```python
    z = mask_poly(data, deg)

    sfit = np.polyval(z, w)

    return sfit

def get_masked_background(spec, lbdas):

    try:

        ref_bkg = mask_fit(spec.data, lvals = [850,865],

                    deg = 4)#, unit = u.angstrom) #850,865

    except AttributeError:

        ref_bkg = mask_fit(spec, lvals = [850,865],

                    deg = 4)#, unit = u.angstrom)

    return ref_bkg

def main(fname, refspec, lmin, lmax, out):

    '''

    Now let's do all the dirty work

    '''

    cube, wcs = load_cube(fname)

    lbdas = wcs.wcs_world2pix([lmin, lmax], 0)[0]

    print('lambdas = ', lbdas)

    if refspec is None:

        print('no refspec given')

        query = input("Do you want to see a sample graph? y/n ")

        if query.lower() == 'y':

            index = input("Enter an index to plot: ")

            try:

                index = int(index)

            except Exception:

                index = input("Sorry, invalid entry. Try again: ")
```

```python
        refspec = quick_plot(fname, index)


else:
    y, x = refspec
    spec = cube[:, y, x]
    plt.plot(wcs.wcs_pix2world(np.arange(cube.shape[0]), 0)[0],
             spec, ds='steps-mid', lw=2)
    plt.show()
# get the baseline for the reference spectrum
ref_bkg = get_masked_background(refspec, lbdas)


new_cube = cube.copy()
print('Calculating background rms...')
sigs = [get_background_rms(new_cube[i])
           for i in tqdm(range(nz))]
sigs = np.asarray(sigs)
print('Done!')
print('Masking invalid values...')
masked_cube = [mask_threshold(new_cube[i],
           sigs[i]) for i in tqdm(range(nz))]
masked_cube = np.asarray(masked_cube)
masked_cube[~(np.isfinite(masked_cube))] = np.ma.masked
print('Done!')
print('\nPerforming scaled background subtraction...')
cont = np.empty_like(cube)
for (y, x) in tqdm(np.ndindex(*cube.shape[1:])):
    sp = masked_cube[:, y, x]
```

```python
        bkg = mask_fit(sp, lvals =
                [850,865], deg = 4, wcs = wcs)
        scale = ref_bkg / bkg
        ref_scaled = refspec / scale
        sub = sp - ref_scaled
        cont[:, y, x] = sub
    print('Done!')
    plt.plot(cont[445], origin = 'lower', vmin =0,
                vmax = 0.8 * cont.max())
    plt.show()
    print(f'\nSaving output to {out}.fits...')
    new_hdu = fits.PrimaryHDU(data = cont)
    new_hdu.writeto(f'{out}.fits', overwrite=True)
    print('Done! \n See ya!')

if __name__ == '__main__':
    args = parse_arguments()
    cube, wcs = load_cube(args.infile)
    lmin, lmax = sort_boundaries(cube, wcs, lmin = args.lmin,
                lmax = args.lmax)
    if args.outfile is None:
        outfile = args.infile.rsplit('/')[-1].strip('.fits')
                +'_base_sub'
    main(args.infile, args.refspec, lmin, lmax,
        outfile if args.outfile is None else args.outfile)
```

A1.2   Diagnostics Code

```
#Reduce runtime of the diagnostics code, the Rapid is False by default.
#accuracy is set to 2 for 2-decimal places by default.
#Increasing n increases run time.
#Goal is to reduce time complexity to O(N) vs O(N^2) for the for loop.
if Rapid:
    def Rapid_Approximate(Image, accuracy):
    """
    Inputs: 2-D image
    """
        array = Image.flatten()
        if type(Image) != np.ndarray:
            Try:
                Image = np.array(Image)
            Except:
                raise TypeError("Invalid ratio Image")
        if Image.ndim != 2:
            raise ValueError("Input must 2D")
        if type(accuracy) != int:
            raise TypeError("Integer values only")
        else:
            Unique_values = np.array(set(round(array, accuracy)))
            Unique_values[Unique_values<0] =np.nan
            Unique_values = Unique_values[~numpy.isnan(Unique_values)]
            def find_nearest(array, value):
                array = np.asarray(array)
```

```python
        idx = (np.abs(array - value)).argmin()
        return array[idx]


    den = fe2.getTemDen(Unique_values, tem = tem, \
        wave1 =w1,wave2=w2)
    if type(den) == list:
        den = np.array(den)
    else:
        pass
    Density_plot = np.empty_like(Image)
    with tqdm(total=Image.shape[0]*Image.shape[1]) as pbar:
        for y,x in tqdm(np.ndindex(*Image.shape)):
            if Image[y,x]<0:
                Density_plot[y,x] =np.nan
            else:
            idx = find_nearest(Unique_values,Image[y,x]
            Density_plot[y,x] = den[idx]
        pbar.update(1)
```

A2   Data Reduction Pipeline

A2.1   .bashrc file

```
. /home/darrencashin/idl88/bin/idl_setup.bash
IDL_INCLUDE="/home/darrencashin/idl88/external/include"
export IDL_INCLUDE
CFITSIOLIBDIR="/home/darrencashin/cfitsio-3.49/lib"
export PATH=$PATH:/home/darrencashin/idl88/bin
OSIRIS_VERBOSE=0
source /home/darrencashin/OsirisDRP/scripts/osirisSetup.sh
osirisSetup /home/darrencashin/OsirisDRP
```

A2.2   Sample XML file

```xml
<?xml version="1.0" encoding="UTF-8"?>
<!-- OS.20091222. -->
<DRF LogPath="/path/to/osiris/spec_orp/DRFs"
    ReductionType="ARP_SPEC">
<dataset InputDir="/path/to/RawData/" Name="OS.20091222."
    OutputDir="path/to/spec_orp">
    <fits FileName="filename_1.fits" />
    ...
    <fits FileName="filename_n.fits" />
</dataset>
<module Name="Subtract Frame"CalibrationFile=
    "/path/to/DarkFrame.fits" />
<module Name="Adjust Channel Levels" />
<module Name="Remove Crosstalk" />
<module Name="Glitch Identification" />
<module Name="Clean Cosmic Rays" />
<module Name="Extract Spectra"
    CalibrationFile="/path/to/RectificationMatrix.fits" />
<module Name="Assemble Data Cube" />
<module Name="Correct Dispersion" Skip="1" />
<module Name="Mosaic Frames" Combine_Method="MEDIAN"
    Offset_Method="TEL" />
<module Name="Save DataSet Information" />
</DRF>
```

A3   Supplementary Figures

A3.1   Position Velocity Diagrams
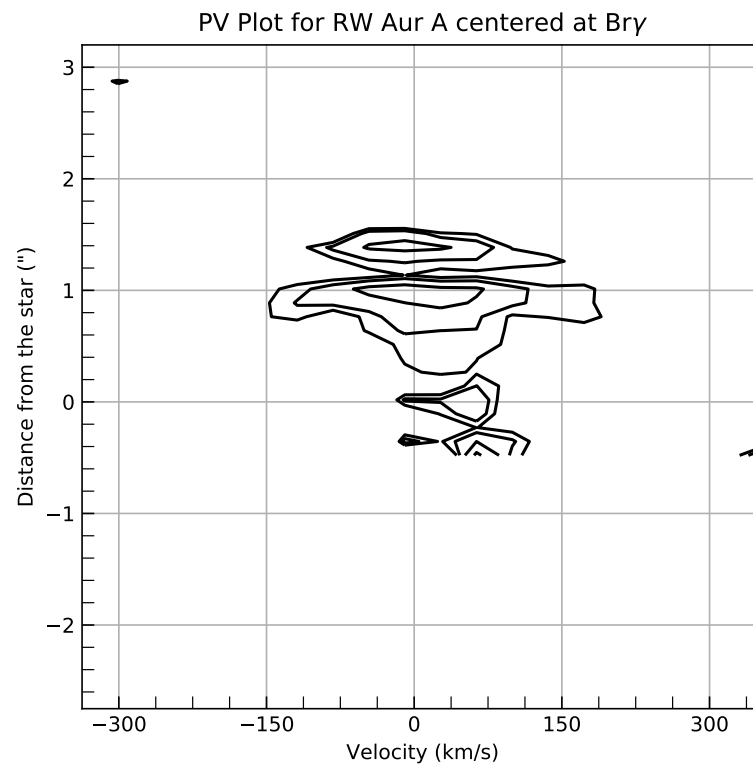
Figure A3.1: Position-velocity diagram for the Brγ emission

A3.2   [Fe II] Line Ratios
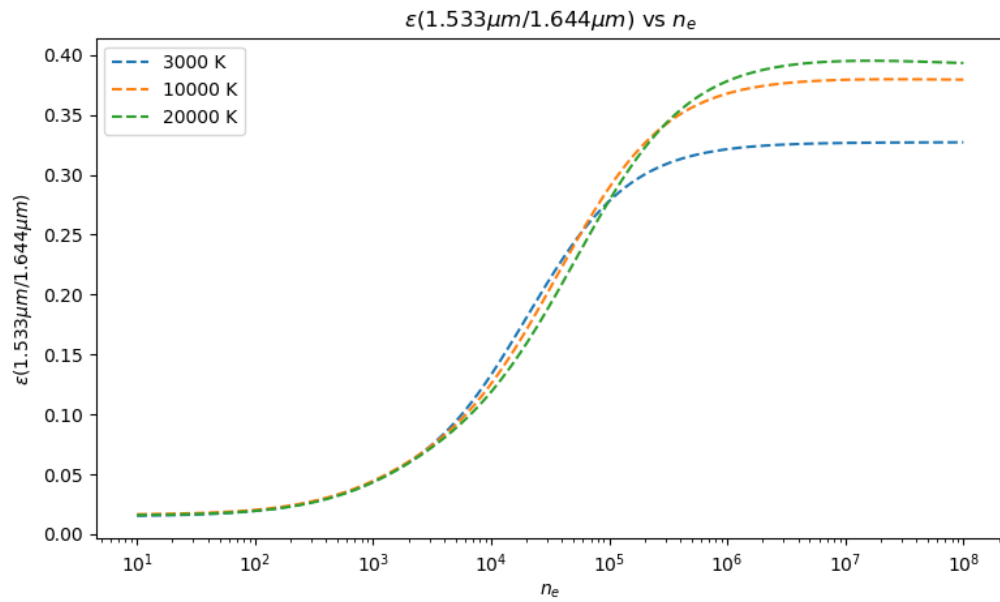
Figure A3.2: Line ratio plot used to model the electron density. σ is the ratio between the two denoted lines and n_e is the electron density
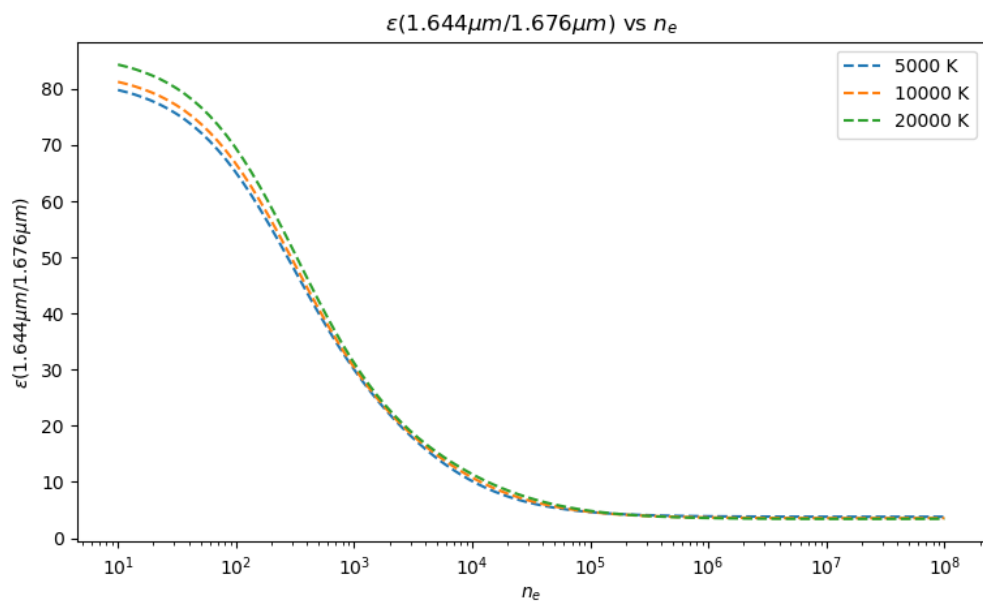
Figure A3.3: Line ratio plot used to model the electron density. σ is the ratio between the two denoted lines and n_e is the electron density

A3.3   Density Figures
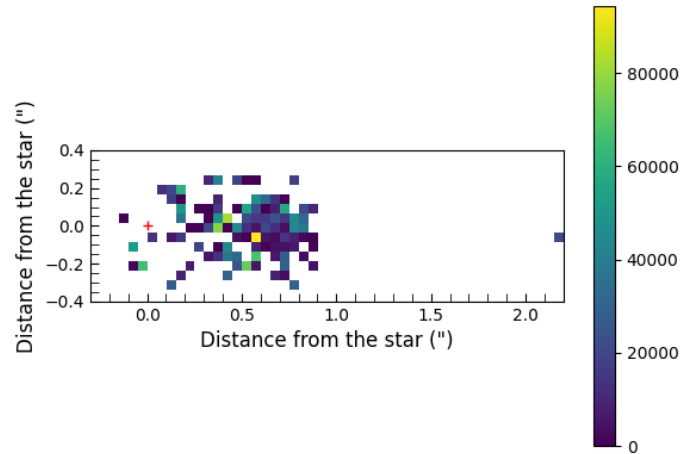
(a) Density map at 3500K using the [Fe II] 1.678 & 1.644μm line ratios in the blue jet.
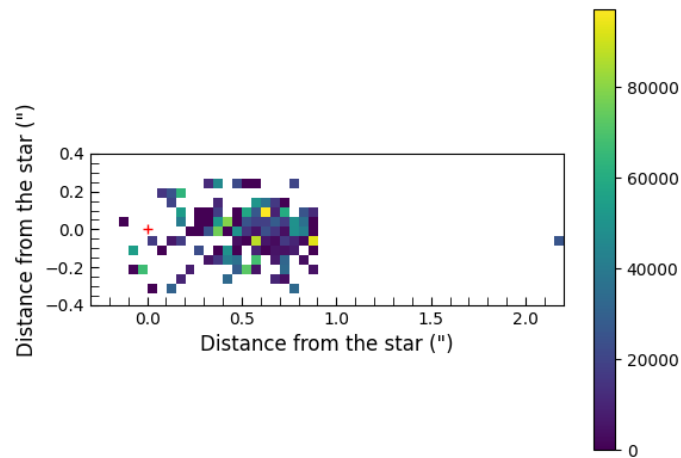
(b) Density map at 10,00K using the [Fe II] 1.678 & 1.644μm line ratios in the blue jet.

Figure A3.4: Density maps for the RW Aur jet, making use of the `PyNeb` modelled ratios. All electron density measurements are in units of cm^{-3}.
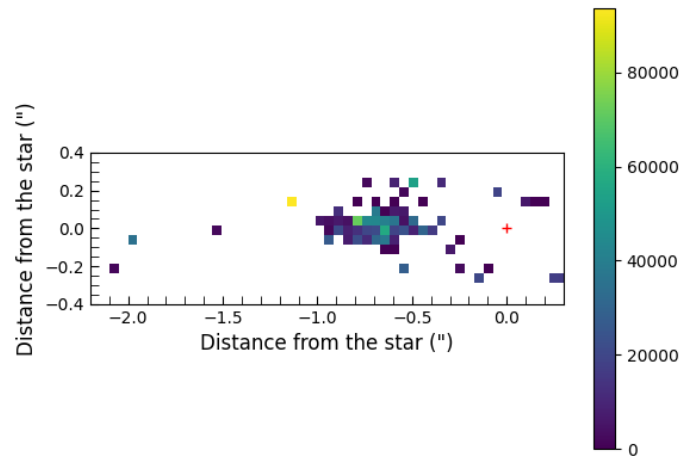
(a) Density map at 3500K using the [Fe II] 1.533 & 1.644μm line ratios in the red jet.
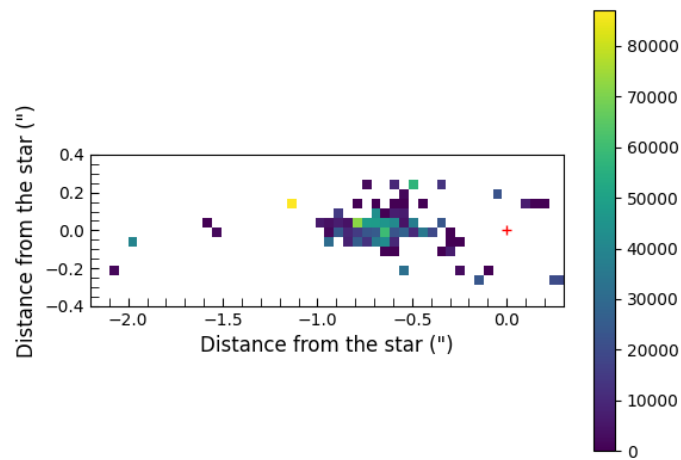
(b) Density map at 10,000K using the [Fe II] 1.533 & 1.644μm line ratios in the red jet.

Figure A3.5: Density maps for the RW Aur jet, making use of the `PyNeb` modelled ratios. All electron density measurements are in units of cm^{-3}.
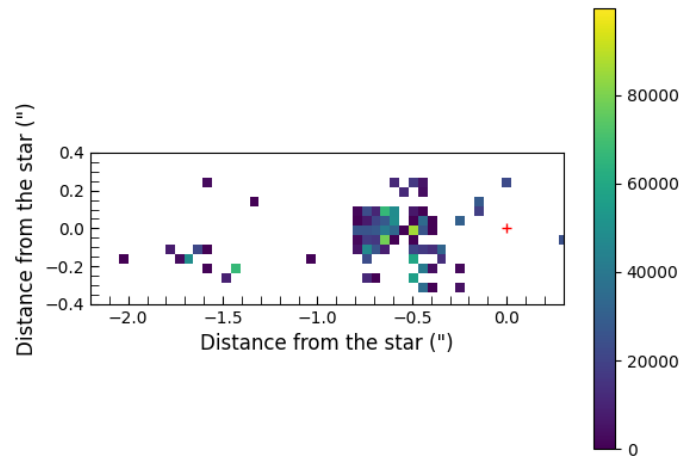
(a) Density map at 3500K using the [Fe II] 1.678 & 1.644μm line ratios in the red jet.
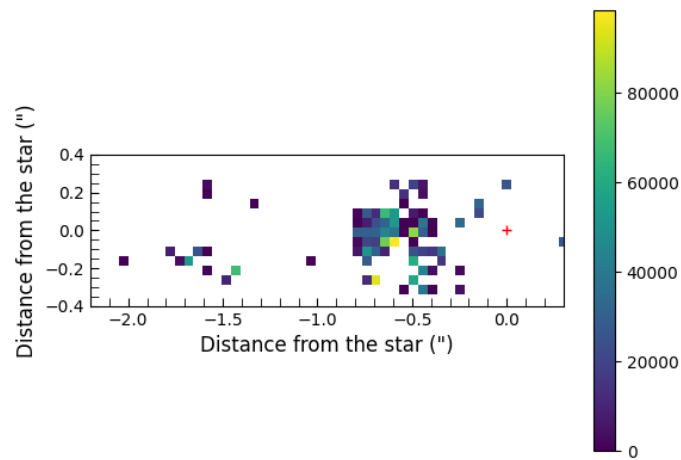
(b) Density map at 10,000K using the [Fe II] 1.678 & 1.644μm line ratios in the red jet.

Figure A3.6: Density maps for the RW Aur jet, making use of the `PyNeb` modelled ratios. All electron density measurements are in units of cm^{-3}.
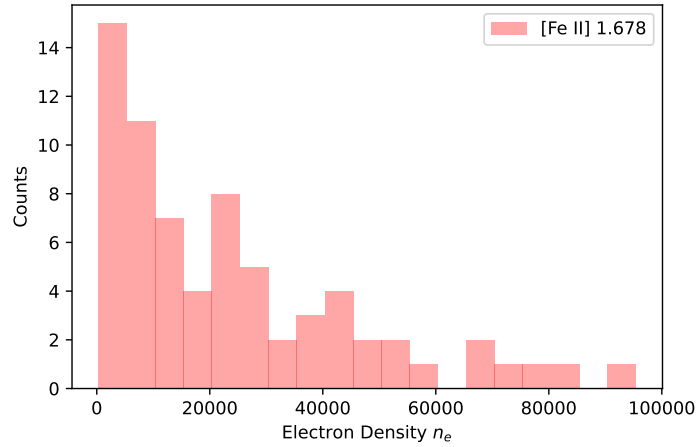
(a) Histogram of the density values in Figure A3.4a
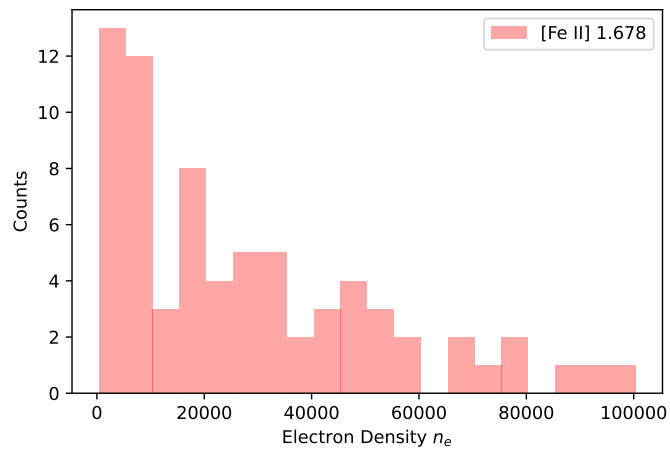
(b) Histogram of the density values in Figure A3.4b

Figure A3.7: Histogram plots for the blue component of the RW Jet. All electron density measurements are in units of cm^{-3}.
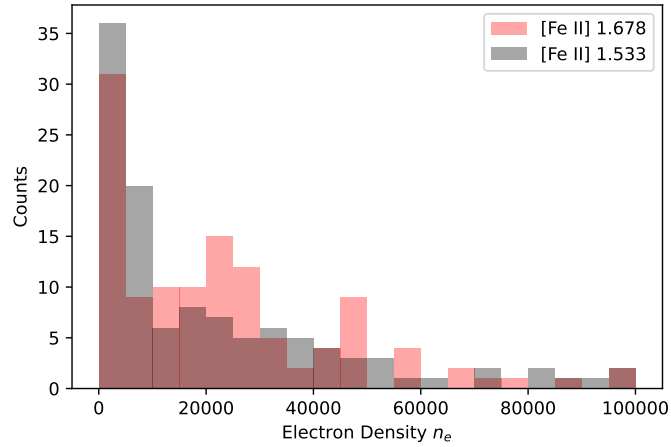
(a) Histogram of the density values in Figures A3.5a& A3.6a
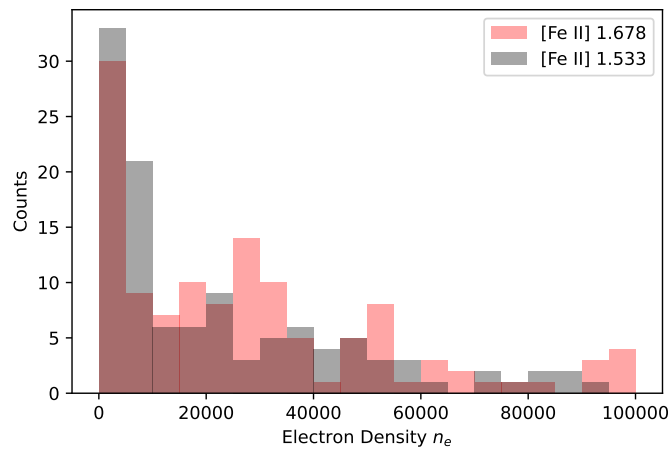
(b) Histogram of the density values in Figures A3.5b& A3.6b

Figure A3.8: Histogram plots for the blue component of the RW Jet. All electron density measurements are in units of cm^{-3}.

References

Agra-Amboage, V., Dougados, C., Cabrit, S. & Reunanen, J. (2011), 'Sub-arcsecond [Fe II] spectro-imaging of the DG Tauri jet-periodic bubbles and a dusty disk wind?', *Astronomy & Astrophysics* **532**, A59.

Akeson, R., Boden, A., Monnier, J., Millan-Gabet, R., Beichman, C., Beletic, J., Calvet, N., Hartmann, L., Hillenbrand, L., Koresko, C. et al. (2005), 'KECK interferometer observations of classical and weak-line T Tauri stars', *The Astrophysical Journal* **635**(2), 1173.

Alcalá, J., Manara, C., Natta, A., Frasca, A., Testi, L., Nisini, B., Stelzer, B., Williams, J., Antoniucci, S., Biazzo, K. et al. (2017), 'X-Shooter spectroscopy of young stellar objects in Lupus-Accretion properties of Class II and transitional objects', *Astronomy & Astrophysics* **600**, A20.

Alcalá, J., Natta, A., Manara, C., Spezzi, L., Stelzer, B., Frasca, A., Biazzo, K., Covino, E., Randich, S., Rigliaco, E. et al. (2014), 'X-Shooter spectroscopy of young stellar objects-IV. Accretion in low-mass stars and substellar objects in Lupus', *Astronomy & Astrophysics* **561**, A2.

Alencar, S., Basri, G., Hartmann, L. & Calvet, N. (2005), 'The extreme T Tauri star RW Aur: accretion and outflow variability', *Astronomy & Astrophysics* **440**(2), 595–608.

Alencar, S. H. (2007), 'Time variable funnel flows', *Proceedings of the International Astronomical Union* **3**(S243), 71–82.

Andre, P., Ward-Thompson, D. & Barsony, M. (1993), 'Submillimeter continuum observations of Rho Ophiuchi A-The candidate protostar VLL 1623 and prestellar clumps', *The Astrophysical Journal* **406**, 122–141.

Anglada, G., López, R., Estalella, R., Masegosa, J., Riera, A. & Raga, A. C. (2007), 'Proper motions of the jets in the region of HH 30 and HL/XZ Tau: Evidence for a binary exciting source of the HH 30 jet', *The Astronomical Journal* **133**(6), 2799.

Antipin, S., Belinski, A., Cherepashchuk, A., Cherjasov, D., Dodin, A., Gorbunov, I., Lamzin, S., Kornilov, M., Kornilov, V., Potanin, S. et al. (2014), 'Resolved photometry of the binary components of RW Aur', *arXiv preprint arXiv:1412.7661* .

Appenzeller, I. & Wolff, B. (1982), 'YY-Orionis Line Profiles in the spectrum of RW-Aurigae', *Astronomy and Astrophysics* **105**, 313.

Arribas, S., Carter, D., Cavaller-Marques, L., Del Burgo, C., Edwards, R., Fuentes, F. J., Garcia, A. A., Herreros, J., Jones, L. R., Mediavilla, E. et al. (1998), INTEGRAL: a

matrix optical fiber system for WYFFOS, *in* 'Optical Astronomical Instrumentation', Vol. 3355, International Society for Optics and Photonics, pp. 821–827.

Bacciotti, F. (2005), Protostellar Jets: A High Angular Resolution Perspective, *in* 'Cores to Clusters', Springer, pp. 67–76.

Bacciotti, F., Hirth, G. & Natta, A. (1996), 'The optical jet of RW Aurigae: excitation temperature and ionization state from long-slit spectra.', *Astronomy and Astrophysics* **310**, 309–314.

Bacciotti, F., Mundt, R., Ray, T. P., Eislöffel, J., Solf, J. & Camezind, M. (2000), 'Hubble Space Telescope stis spectroscopy of the optical outflow from DG Tauri: Structure and kinematics on subarcsecond scales', *The Astrophysical Journal Letters* **537**(1), L49.

Bacon, R., Adam, G., Baranne, A., Courtes, G., Dubet, D., Dubois, J., Emsellem, E., Ferruit, P., Georgelin, Y., Monnet, G. et al. (1995), '3D spectrography at high spatial resolution. I. Concept and realization of the integral field spectrograph TIGER.', *Astronomy and Astrophysics Supplement Series* **113**, 347.

Bary, J. S., Weintraub, D. A. & Kastner, J. H. (2003), 'Detections of rovibrational H2 emission from the disks of T Tauri stars', *The Astrophysical Journal* **586**(2), 1136.

Batalha, C., Batalha, N., Alencar, S., Lopes, D. & Duarte, E. (2002), 'Variability of southern T Tauri stars (vastt). III. the continuum flux changes of the TW Hydrae bright spot', *The Astrophysical Journal* **580**(1), 343.

Beck, T. L., Bary, J. S. & McGregor, P. J. (2010), 'Spatially extended brackett gamma emission in the environments of young stars', *The Astrophysical Journal* **722**(2), 1360.

Beck, T. L., McGregor, P. J., Takami, M. & Pyo, T.-S. (2008), 'Spatially resolved molecular hydrogen emission in the inner 200 au environments of classical T Tauri stars', *The Astrophysical Journal* **676**(1), 472.

Beck, T. L. & Simon, M. (2001), 'The Variability of T Tau, RY Tau and RW Aur from 1899 to 1952', *arXiv preprint astro-ph/0104268* .

Beckwith, S., Gatley, I., Matthews, K. & Neugebauer, G. (1978), 'Molecular hydrogen emission from T Tauri stars', *The Astrophysical Journal* **223**, L41–L43.

Berdnikov, L., Burlak, M., Vozyakova, O., Dodin, A., Lamzin, S. & Tatarnikov, A. (2017), 'On the jet of a young star RW Aur A and related problems', *Astrophysical Bulletin* **72**(3), 277–285.

Bertout, C., Siess, L. & Cabrit, S. (2007), 'The evolution of stars in the Taurus-Auriga T association', *Astronomy & Astrophysics* **473**(3), L21–L24.

Bontemps, S., André, P., Terebey, S. & Cabrit, S. (1996), Evolution of outflow activity around low mass embedded young stellar objects, *in* 'Disks and Outflows Around Young Stars', Springer, pp. 270–275.

Boss, A. P. & Yorke, H. W. (1990), 'Spectral and isophotal appearance of three-dimensional protostellar models', *The Astrophysical Journal* **353**, 236–244.

Bouvier, J. & Appenzeller, I. (n.d.), 'Measuring the physical conditions of accreting gas in T Tauri systems'.

Bozhinova, I., Scholz, A., Costigan, G., Lux, O., Davis, C., Ray, T., Boardman, N., Hay, K., Hewlett, T., Hodosán, G. et al. (2016), 'The disappearing act: a dusty wind eclipsing RW Aur', *Monthly Notices of the Royal Astronomical Society* **463**(4), 4459–4468.

Buckle, J., Hatchell, J. & Fuller, G. (1999), 'The bow shock and jet in L483', *Astronomy and Astrophysics* **348**, 584–593.

Bunker, P. (2012), *Molecular Symmetry and Spectroscopy*, Elsevier Science.
URL: *https://books.google.ie/books?id=0xxJQI8zOlYC*

Cabrit, S., Pety, J., Pesenti, N. & Dougados, C. (2006), 'Tidal stripping and disk kinematics in the RW Aurigae system', *Astronomy & Astrophysics* **452**(3), 897–906.

Calvet, N. & Gullbring, E. (1998), 'The structure and emission of the accretion shock in T Tauri stars', *The Astrophysical Journal* **509**(2), 802.

Calvet, N., Muzerolle, J., Briceno, C., Hernández, J., Hartmann, L., Saucedo, J. L. & Gordon, K. D. (2004), 'The mass accretion rates of intermediate-mass T Tauri stars', *The Astronomical Journal* **128**(3), 1294.

Caratti o Garatti, A., Giannini, T., Nisini, B. & Lorenzetti, D. (2006), 'H2 active jets in the near IR as a probe of protostellar evolution', *Astronomy & Astrophysics* **449**(3), 1077–1088.

Cardelli, J. A., Clayton, G. C. & Mathis, J. S. (1989), 'The relationship between infrared, optical, and ultraviolet extinction', *The Astrophysical Journal* **345**, 245–256.

Cazzoletti, P., Manara, C., Liu, H. B., Van Dishoeck, E., Facchini, S., Alcalà, J., Ansdell, M., Testi, L., Williams, J., Carrasco-González, C. et al. (2019), 'ALMA survey of Class II protoplanetary disks in corona australis: a young region with low disk masses', *Astronomy & Astrophysics* **626**, A11.

Chou, M.-Y., Takami, M., Manset, N., Beck, T., Pyo, T.-S., Chen, W.-P., Panwar, N., Karr, J. L., Shang, H. & Liu, H. B. (2013), 'Time variability of emission lines for

four active T Tauri stars. I. OCTOBER–DECEMBER in 2010', *The Astronomical Journal* **145**(4), 108.

Coffey, D., Bacciotti, F. & Podio, L. (2008), 'T Tauri jet physics resolved near the launching region with the Hubble Space Telescope', *The Astrophysical Journal* **689**(2), 1112.

Coffey, D., Bacciotti, F., Woitas, J., Ray, T. P. & Eislöffel, J. (2004), 'Rotation of jets from young stars: New clues from the Hubble Space Telescope imaging spectrograph', *The Astrophysical Journal* **604**(2), 758.

Coffey, D., Rigliaco, E., Bacciotti, F., Ray, T. P. & Eislöffel, J. (2012), 'Jet rotation investigated in the near-ultraviolet with the Hubble Space Telescope imaging spectrograph', *The Astrophysical Journal* **749**(2), 139.

Cohen, M., Wheaton, W. A. & Megeath, S. (2003), 'Spectral irradiance calibration in the infrared. XIV. the absolute calibration of 2MASS', *The Astronomical Journal* **126**(2), 1090.

Colzi, L. (2021), *Isotopic fractionation study towards massive star-forming regions across the Galaxy*, Firenze University Press.

Covey, K. R., Greene, T. P., Doppmann, G. W. & Lada, C. J. (2006), 'The radial velocity distribution of Class I and flat-spectrum protostars', *The Astronomical Journal* **131**(1), 512.

Dai, F., Facchini, S., Clarke, C. J. & Haworth, T. J. (2015), 'A tidal encounter caught in the act: modelling a star–disc fly-by in the young RW Aurigae system', *Monthly Notices of the Royal Astronomical Society* **449**(2), 1996–2009.

Davis, C., Froebrich, D., Stanke, T., Megeath, S., Kumar, M., Adamson, A., Eislöffel, J., Gredel, R., Khanzadyan, T., Lucas, P. et al. (2009), 'A census of molecular hydrogen outflows and their sources along the Orion A molecular ridge-characteristics and overall distribution', *Astronomy & Astrophysics* **496**(1), 153–176.

Davis, C. J., Cervantes, B., Nisini, B., Giannini, T., Takami, M., Whelan, E., Smith, M. D., Ray, T. P., Chrysostomou, A. & Pyo, T.-S. (2011), 'VLT integral field spectroscopy of embedded protostars: using near-infrared emission lines as tracers of accretion and outflow', *Astronomy & Astrophysics* **528**, A3.

Davis, C. J., Ray, T. P., Desroches, L. & Aspin, C. (2001), 'Near-infrared echelle spectroscopy of Class I protostars: molecular hydrogen emission-line (MHEL) regions revealed', *Monthly Notices of the Royal Astronomical Society* **326**(2), 524–538.

Davis, C., Whelan, E., Ray, T. & Chrysostomou, A. (2003), 'Near-IR echelle spectroscopy

of Class I protostars: Mapping forbidden emission-line (FEL) regions in [Fe II]', *Astronomy & Astrophysics* **397**(2), 693–710.

Dodin, A., Grankin, K., Lamzin, S., Nadjip, A., Safonov, B., Shakhovskoi, D., Shenavrin, V., Tatarnikov, A. & Vozyakova, O. (2019), 'Analysis of colour and polarimetric variability of RW Aur A in 2010–2018', *Monthly Notices of the Royal Astronomical Society* **482**(4), 5524–5541.

Doppmann, G., Greene, T., Covey, K. & Lada, C. (2005), 'The physical natures of Class I and flat-spectrum protostellar photospheres: a near-infrared spectroscopic study', *The Astronomical Journal* **130**(3), 1145.

Dougados, C., Cabrit, S. & Fouquet, C. L. (2002), 'Probing the origin of mass loss in T Tauri star', *Revista Mexicana de Astronomía y Astrofísica* **13**, 43–48.

Dougados, C., Cabrit, S., Lavalley, C. & Ménard, F. (2000), 'T Tauri stars microjets resolved by adaptive optics', *Astronomy and Astrophysics* **357**, L61–L64.

Dyda, S., Lovelace, R. V., Ustyugova, G. V., Lii, P. S., Romanova, M. M. & Koldoba, A. V. (2015), 'Asymmetric MHD outflows/jets from accreting T Tauri stars', *Monthly Notices of the Royal Astronomical Society* **450**(1), 481–493.

Edwards, S., Fischer, W., Hillenbrand, L. & Kwan, J. (2006), 'Probing T Tauri accretion and outflow with 1 micron spectroscopy', *The Astrophysical Journal* **646**(1), 319.

Edwards, S., Hartigan, P., Ghandour, L. & Andrulis, C. (1994), 'Spectroscopic evidence for magnetospheric accretion in classical T Tauri stars', *The Astronomical Journal* **108**.

Eisner, J. A., Hillenbrand, L., White, R., Bloom, J., Akeson, R. & Blake, C. (2007), 'Near-infrared interferometric, spectroscopic, and photometric monitoring of T Tauri inner disks', *The Astrophysical Journal* **669**(2), 1072.

Ellerbroek, L., Podio, L., Dougados, C., Cabrit, S., Sitko, M., Sana, H., Kaper, L., de Koter, A., Klaassen, P., Mulders, G. et al. (2014), 'Relating jet structure to photometric variability: the Herbig Ae star HD 163296', *Astronomy & Astrophysics* **563**, A87.

Erkal, J., Dougados, C., Coffey, D., Cabrit, S., Bacciotti, F., Garcia-Lopez, R., Fedele, D. & Chrysostomou, A. (2021), 'Launching the asymmetric bipolar jet of DO Tau', *Astronomy & Astrophysics* **650**, A46.

Erkal, J., Nisini, B., Coffey, D., Bacciotti, F., Hartigan, P., Antoniucci, S., Giannini, T., Eislöffel, J. & Manara, C. F. (2021), 'Probing jets from young embedded sources: clues from HST near-IR [Fe II] images', *The Astrophysical Journal* **919**(1), 23.

Facchini, S., Manara, C., Schneider, P., Clarke, C., Bouvier, J., Rosotti, G., Booth, R. & Haworth, T. (2016), 'Violent environment of the inner disk of RW Aurigae A probed by the 2010 and 2015 dimming events', *Astronomy & Astrophysics* **596**, A38.

Fang, M., Pascucci, I., Edwards, S., Gorti, U., Banzatti, A., Flock, M., Hartigan, P., Herczeg, G. J. & Dupree, A. K. (2018), 'A new look at T Tauri star forbidden lines: MHD-driven winds from the inner disk', *The Astrophysical Journal* **868**(1), 28.

Fedriani, R., o Garatti, A. C., Purser, S., Sanna, A., Tan, J., Garcia-Lopez, R., Ray, T., Coffey, D., Stecklum, B. & Hoare, M. (2019), 'Measuring the ionisation fraction in a jet from a massive protostar', *Nature communications* **10**(1), 1–9.

Fendt, C. (2009), 'Formation of protostellar jets as two-component outflows from star-disk magnetospheres', *The Astrophysical Journal* **692**(1), 346.

Frank, A., Ray, T., Cabrit, S., Hartigan, P. Acre, H., Bacciotti, F., Bally, J., Benisty, M., Eislöffel, J., Güdel, M., Lebedev, S., Nisini, B. & Raga, A. (2014), 'Jets and Outflows from Star to Cloud: Observations Confront Theory', *Protostars and planets VI* pp. 452–474.

Gahm, G. F. (1970), 'The Spectrum of RW Aurigae, 3250 to 4900 aa', *The Astrophysical Journal* **160**, 1117.

Gahm, G., Petrov, P., Duemmler, R., Gameiro, J. & Lago, M. (1999), 'RW Aur A, a close binary?', *Astronomy and Astrophysics* **352**, L95–L98.

Gargaud, M. (2011), *Encyclopedia of astrobiology*, 1 edn, Springer.

Garstang, R. (1962), 1 - Forbidden Transitions, *in* D. BATES, ed., 'Atomic and Molecular Processes', Vol. 13 of *Pure and Applied Physics*, Elsevier, pp. 1–46.
URL: *https://www.sciencedirect.com/science/article/pii/B9780120814503500059*

Gatti, T., Natta, A., Randich, S., Testi, L. & Sacco, G. (2008), 'Accretion properties of T Tauri stars in σ Orionis', *Astronomy & Astrophysics* **481**(2), 423–432.

Ghez, A., Neugebauer, G. & Matthews, K. (1993), 'The multiplicity of T Tauri stars in the star forming regions Taurus-Auriga and Ophiuchus-Scorpius: A 2.2 micron speckle imaging survey', *Astronomical Journal* **106**(5), 2005–2023.

Ghosh, P. & Lamb, F. (1979), 'Accretion by rotating magnetic neutron stars. III-accretion torques and period changes in pulsating x-ray sources', *The Astrophysical Journal* **234**, 296–316.

Giannini, T., Antoniucci, S., Nisini, B., Lorenzetti, D., Alcalá, J., Bacciotti, F., Bonito, R., Podio, L. & Stelzer, B. (2014), 'Empirical determination of Einstein A-coefficient ratios of bright [Fe II] lines', *The Astrophysical Journal* **798**(1), 33.

Giannini, T., Nisini, B., Antoniucci, S., Biazzo, K., Alcalá, J., Bacciotti, F., Fedele, D., Frasca, A., Harutyunyan, A., Munari, U. et al. (2019), 'GIARPS High-resolution Observations of T Tauri stars (GHOsT-I. Jet line emission', *Astronomy & Astrophysics* **631**, A44.

Glasby, J. S. (1974), *The nebular variables*, Vol. 69, Pergamon Press.
  URL: *https://books.google.ie/books?id=0xxJQI8zOlYC*

Grankin, K. (2016), 'T Tauri stars: Physical parameters and evolutionary status', *Astronomy Letters* **42**(5), 314–328.

Gredel, R. (1994), 'Near-infrared spectroscopy and imaging of Herbig-Haro objects', *Astronomy and Astrophysics* **292**, 580–592.

Gredel, R. & Dalgarno, A. (1995), 'Infrared response of H2 to X-Rays', *The Astrophysical Journal* **446**, 852.

Greene, T. P., Barsony, M. & Weintraub, D. A. (2010), 'Near-IR H2 Emission of Protostars: Probing Circumstellar Environments', *The Astrophysical Journal* **725**(1), 1100.

Grinin, V., Petrov, P. & Shakhovskaia, N. (1985), 'The results of spectroscopic and photometric patrol observations of RW Aurigae. i. variability of the balmer lines.', *Izvestiya Ordena Trudovogo Krasnogo Znameni Krymskoj Astrofizicheskoj Observatorii* **71**, 109–127.

Günther, H. M. (2013), 'Accretion, winds and outflows in young stars', *Astronomische Nachrichten* **334**(1-2), 67–72.

Günther, H. M., Birnstiel, T., Huenemoerder, D., Principe, D., Schneider, P., Wolk, S., Dubois, F., Logie, L., Rau, S. & Vanaverbeke, S. (2018), 'Optical dimming of RW Aur associated with an iron-rich corona and exceptionally high absorbing column density', *The Astronomical Journal* **156**(2), 56.

Günther, H. M., Espaillat, C., France, K., Li, Z.-Y., Dougados, C., Schneider, P. C., Fischer, W., Wolk, S. J., Beck, T. L., Güdel, M. et al. (2019), 'The fastest components in stellar jets', *arXiv preprint arXiv:1903.09540* .

Hartigan, P., Edwards, S. & Ghandour, L. (1995), 'Disk accretion and mass loss from young stars', *The Astrophysical Journal* **452**, 736.

Hartigan, P. & Morse, J. (2007), 'Collimation, proper motions, and physical conditions in the HH 30 jet from Hubble Space Telescope slitless spectroscopy', *The Astrophysical Journal* **660**(1), 426.

Hartmann, L. (1982), 'Line profiles of T Tauri stars-Clues to the nature of the mass flow', *The Astrophysical Journal Supplement Series* **48**, 109–126.

Hartmann, L., Calvet, N., Gullbring, E. & D'Alessio, P. (1998), 'Accretion and the evolution of T Tauri disks', *The Astrophysical Journal* **495**(1), 385.

Herbig, G. H. (1962), The properties and problems of T Tauri stars and related objects, *in* 'Advances in Astronomy and Astrophysics', Vol. 1, Elsevier, pp. 47–103.

Herbig, G. H. (1967), 'The youngest stars', *Scientific American* **217**(2), 30–37.

Herbig, G. H. & Bell, K. R. (1988), 'Third catalog of emission-line stars of the orion population: 3: 1988', *Third catalog of emission-line stars of the Orion population* .

Hirth, G. A., Mundt, R., Solf, J. & Ray, T. P. (1994), 'Asymmetries in bipolar jets from young stars', *The Astrophysical Journal* **427**, L99–L102.

Ingleby, L., Calvet, N., Herczeg, G., Blaty, A., Walter, F., Ardila, D., Alexander, R., Edwards, S., Espaillat, C., Gregory, S. G. et al. (2013), 'Accretion rates for T Tauri stars using nearly simultaneous ultraviolet and optical spectra', *The Astrophysical Journal* **767**(2), 112.

Johns-Krull, C. M., Greene, T. P., Doppmann, G. W. & Covey, K. R. (2009), 'First magnetic field detection on a Class I protostar', *The Astrophysical Journal* **700**(2), 1440.

Johnstone, C. P., Jardine, M., Gregory, S. G., Donati, J.-F. & Hussain, G. (2013), 'Classical T Tauri stars: magnetic fields, coronae and star–disc interactions', *Monthly Notices of the Royal Astronomical Society* **437**(4), 3202–3220.
URL: *http://dx.doi.org/10.1093/mnras/stt2107*

Kenyon, S. J., Gomez, M., Marzke, R. O. & Hartmann, L. (1994), 'New pre-main-sequence stars in the Taurus-Auriga molecular cloud', *The Astronomical Journal* **108**, 251–261.

Kenyon, S. J., Gomez, M. & Whitney, B. A. (2008), 'Low mass star formation in the Taurus-Auriga clouds', *arXiv preprint arXiv:0810.1298* .

Kirwan, A., Murphy, A., Schneider, P., Whelan, E., Dougados, C. & Eislöffel, J. (2022), 'The morphology of the HD 163296 jet as a window on its planetary system'.

Kitamura, Y., Momose, M., Yokogawa, S., Kawabe, R., Tamura, M. & Ida, S. (2002), 'Investigation of the physical properties of protoplanetary disks around T Tauri stars by a 1 arcsecond imaging survey: evolution and diversity of the disks in their accretion stage', *The Astrophysical Journal* **581**(1), 357.

Koenigl, A. (1991), 'Disk accretion onto magnetic T Tauri stars', *The Astrophysical Journal* **370**, L39–L43.

Koutoulaki, M., Facchini, S., Manara, C., Natta, A., Lopez, R. G., Fedriani, R., o Garatti, A. C., Coffey, D. & Ray, T. (2019), 'Exploring the dimming event of RW Aurigae a through multi-epoch VLT/X-Shooter spectroscopy', *Astronomy & Astrophysics* **625**, A49.

Kraus, A. L., Herczeg, G. J., Rizzuto, A. C., Mann, A. W., Slesnick, C. L., Carpenter, J. M., Hillenbrand, L. A. & Mamajek, E. E. (2017), 'The Greater Taurus–Auriga Ecosystem. I. There is a Distributed Older Population', *The Astrophysical Journal* **838**(2), 150.

Kuhi, L. (1966), 'T Tauri stars: A short review', *Journal of the Royal Astronomical Society of Canada* **60**, 1.

Lamzin, S., Cheryasov, D., Chuntonov, G., Dodin, A., Grankin, K., Malanchev, K., Nadzhip, A., Safonov, B., Shakhovskoy, D., Shenavrin, V. et al. (2017), 'Anomalous eclipses of the young star RW Aur A', *arXiv preprint arXiv:1707.09671* .

Larkin, J. E., Quirrenbach, A., Krabbe, A., Aliado, T., Barczys, M., Brims, G., Canfield, J., Gasaway, T. M., LaFreniere, D., Magnone, N. et al. (2003), OSIRIS: an infrared integral field spectrograph for the KECK adaptive optics system, *in* 'Instrument Design and Performance for Optical/Infrared Ground-based Telescopes', Vol. 4841, International Society for Optics and Photonics, pp. 1600–1610.

Lavalley-Fouquet, C., Cabrit, S. & Dougados, C. (2000), 'DG Tau: A shocking jet', *Astronomy and Astrophysics* **356**, L41–L44.

Lee, C.-F. (2020), 'Molecular jets from low-mass young protostellar objects', *The Astronomy and Astrophysics Review* **28**(1), 1–35.

Lee, C.-F., Hasegawa, T. I., Hirano, N., Palau, A., Shang, H., Ho, P. T. & Zhang, Q. (2010), 'The reflection-symmetric wiggle of the young protostellar jet HH 211', *The Astrophysical Journal* **713**(2), 731.

Lisse, C., Sitko, M., Wolk, S., Günther, H., Brittain, S., Green, J., Steckloff, J., Johnson, B., Espaillat, C., Koutoukali, M. et al. (2022), 'RW Aur a: SpeX Spectral Evidence for Differentiated Planetesimal Formation, Migration and Destruction in an 3 Myr Old Excited CTTS System', *arXiv preprint arXiv:2201.10465* .

Liu, C.-F. & Shang, H. (2012), 'RW Aur A from the X-Wind Point of View: General Features', *The Astrophysical Journal* **761**(2), 94.

Lockhart, K. E., Do, T., Larkin, J. E., Boehle, A., Campbell, R. D., Chappell, S., Chu, D., Ciurlo, A., Cosens, M., Fitzgerald, M. P., Ghez, A., Lu, J. R., Lyke, J. E., Mieda,

E., Rudy, A. R., Vayner, A., Walth, G. & Wright, S. A. (2019), 'Characterizing and Improving the Data Reduction Pipeline for the KECK OSIRIS Integral Field Spectrograph', **157**(2), 75.

López-Martín, L., Cabrit, S. & Dougados, C. (2003), 'Proper motions and velocity asymmetries in the RW Aur jet', *Astronomy & Astrophysics* **405**(1), L1–L4.

Lopez, R. G., o Garatti, A. C., Weigelt, G., Nisini, B. & Antoniucci, S. (2013), 'Spatially resolved H2 emission from a very low-mass star', *Astronomy & Astrophysics* **552**, L2.

Luhman, K., Allen, P., Espaillat, C., Hartmann, L. & Calvet, N. (2009), 'The disk population of the Taurus star-forming region', *The Astrophysical Journal Supplement Series* **186**(1), 111.

Luridiana, V., Morisset, C. & Shaw, R. (2013), 'Pyneb: Analysis of emission lines', *Astrophysics Source Code Library* pp. ascl–1304.

Lyke, J., Do, T., Boehle, A., Campbell, R., Chappell, S., Fitzgerald, M., Gasawy, T., Iserlohe, C., Krabbe, A., Larkin, J., Lockhart, K., Lu, J., Mieda, E., McElwain, M., Perrin, M., Rudy, A., Sitarski, B., Vayner, A., Walth, G., Weiss, J., Wizanski, T. & Wright, S. (2017), 'OSIRIS Toolbox: OH-Suppressing InfraRed Imaging Spectrograph pipeline'.

Mamajek, E. E. (2009), Initial conditions of planet formation: lifetimes of primordial disks, *in* 'AIP Conference Proceedings', Vol. 1158, American Institute of Physics, pp. 3–10.

Manara, C., Rosotti, G., Testi, L., Natta, A., Alcalá, J., Williams, J., Ansdell, M., Miotello, A., van der Marel, N., Tazzari, M. et al. (2016), 'Evidence for a correlation between mass accretion rates onto young stars and the mass of their protoplanetary disks', *Astronomy & Astrophysics* **591**, L3.

Masciadri, E. & Raga, A. (2002), 'Herbig-Haro jets from orbiting sources', *The Astrophysical Journal* **568**(2), 733.

Massi, F., Codella, C. & Brand, J. (2004), 'Discovery of [Fe II]-and H-emission from protostellar jets in the CB3 and CB230 globules', *Astronomy & Astrophysics* **419**(1), 241–247.

Matt, S. & Pudritz, R. E. (2005), 'Accretion-powered stellar winds as a solution to the stellar angular momentum problem', *The Astrophysical Journal* **632**(2), L135.

Melnikov, S. Y., Eislöffel, J., Bacciotti, F., Woitas, J. & Ray, T. P. (2009), 'HST/STIS observations of the RW Aurigae bipolar jet: mapping the physical parameters close to the source', *Astronomy & Astrophysics* **506**(2), 763–777.

Montmerle, T., Grosso, N., Tsuboi, Y. & Koyama, K. (2000), 'Rotation and x-ray emission from protostars', *The Astrophysical Journal* **532**(2), 1097.

Mooley, K., Hillenbrand, L., Rebull, L., Padgett, D. & Knapp, G. (2013), 'B-and A-type Stars in the Taurus-Auriga star-forming region', *The Astrophysical Journal* **771**(2), 110.

Mundt, R. & Giampapa, M. (1982), 'Observations of rapid line profile variability in the spectra of T Tauri stars', *The Astrophysical Journal* **256**, 156–167.

Murphy, A., Dougados, C., Whelan, E., Bacciotti, F., Coffey, D., Comerón, F., Eislöffel, J. & Ray, T. (2021), 'A MUSE Spectro-imaging Study of the Th 28 jet: Precession in the inner jet', *arXiv preprint arXiv:2107.08065* .

Muzerolle, J., Hartmann, L. & Calvet, N. (1998), 'A Brγ Probe of Disk Accretion in T Tauri stars and Embedded Young Stellar Objects', *The Astronomical Journal* **116**(6), 2965.

Najita, J., Carr, J. S. & Tokunaga, A. T. (1996), 'High-resolution spectroscopy of Br gamma emission in young stellar objects', *The Astrophysical Journal* **456**, 292.

Nisini, B., Antoniucci, S., Alcalá, J., Giannini, T., Manara, C., Natta, A., Fedele, D. & Biazzo, K. (2018), 'Connection between jets, winds and accretion in T Tauri stars-the X-Shooter view', *Astronomy & Astrophysics* **609**, A87.

Park, S. & Kenyon, S. J. (2002), 'Extended near-infrared emission from candidate protostars in the Taurus-Auriga molecular cloud', *The Astronomical Journal* **123**(6), 3370.

Pelletier, G. & Pudritz, R. E. (1992), 'Hydromagnetic disk winds in young stellar objects and active galactic nuclei', *The Astrophysical Journal* **394**, 117–138.

Percy, J. (2011), *Understanding Variable Stars*, Cambridge University Press.
URL: *https://books.google.ie/books?id=pqiAZwEACAAJ*

Pesenti, N., Dougados, C., Cabrit, S., O'Brien, D., Garcia, P. & Ferreira, J. (2003), 'Near-IR [Fe II] emission diagnostics applied to cold disk winds in young stars', *Astronomy & Astrophysics* **410**(1), 155–164.

Petrov, P., Gahm, G. F., Djupvik, A., Babina, E., Artemenko, S. & Grankin, K. (2015), 'Another deep dimming of the classical T Tauri star RW Aurigae A', *Astronomy & Astrophysics* **577**, A73.

Petrov, P., Gahm, G., Gameiro, J., Duemmler, R., Ilyin, I., Laakkonen, T., Lago, M. & Tuominen, I. (2001), 'Non-axisymmetric accretion on the classical TTS RW Aur A', *Astronomy & Astrophysics* **369**(3), 993–1008.

Petrov, P. & Kozack, B. (2007), 'The origin of the photometric and spectral variability of RW Aur', *Astronomy Reports* **51**(6), 500–511.

Prato, L., Lockhart, K., Johns-Krull, C. M. & Rayner, J. T. (2009), 'Stellar and circumstellar properties of Class I protostars', *The Astronomical Journal* **137**(4), 3931.

Pyo, T.-S., Hayashi, M., Kobayashi, N., Tokunaga, A. T., Terada, H., Takami, H., Takato, N., Davis, C. J., Takami, M., Hayashi, S. S. et al. (2006), 'Adaptive optics spectroscopy of the [Fe II] outflows from HL Tauri and RW Aurigae', *The Astrophysical Journal* **649**(2), 836.

Raga, A., Cantó, J. & Biro, S. (1993), 'Ballistic stellar jets from sources with a time-dependent ejection direction', *Monthly Notices of the Royal Astronomical Society* **260**(1), 163–170.

Raga, A., Esquivel, A., Velázquez, P., Cantó, J., Haro-Corzo, S., Riera, A. & Rodríguez-González, A. (2009), 'Mirror and point symmetries in a ballistic jet from a binary system', *The Astrophysical Journal* **707**(1), L6.

Reipurth, B. & Bally, J. (2001), 'Herbig-Haro flows: Probes of early stellar evolution', *Annual Review of Astronomy and Astrophysics* **39**(1), 403–455.

Rodriguez, J. E., Pepper, J., Stassun, K. G., Siverd, R. J., Cargile, P., Beatty, T. G. & Gaudi, B. S. (2013), 'Occultation of the T Tauri star RW Aurigae a by its tidally disrupted disk', *The Astronomical Journal* **146**(5), 112.

Rodriguez, J. E., Reed, P. A., Siverd, R. J., Pepper, J., Stassun, K. G., Gaudi, B. S., Weintraub, D. A., Beatty, T. G., Lund, M. B. & Stevens, D. J. (2016), 'Recurring occultations of RW Aurigae by coagulated dust in the tidally disrupted circumstellar disk', *The Astronomical Journal* **151**(2), 29.

Rousselot, P., Lidman, C., Cuby, J.-G., Moreels, G. & Monnet, G. (2000), 'Night-sky spectral atlas of OH emission lines in the near-infrared', *Astronomy and Astrophysics* **354**, 1134–1150.

Schneider, P., Günther, H., Robrade, J., Facchini, S., Hodapp, K., Manara, C., Perdelwitz, V., Schmitt, J., Skinner, S. & Wolk, S. (2015), 'The nature of the 2014–2015 dim state of RW Aurigae revealed by X-ray, optical, and near-IR observations', *Astronomy & Astrophysics* **584**, L9.

Shang, H., Li, Z.-Y. & Hirano, N. (2007), 'Jets and bipolar outflows from young stars: theory and observational tests', *Protostars and planets V* pp. 261–276.

Shenavrin, V., Petrov, P. & Grankin, K. (2015), 'Hot dust revealed during the dimming of the T Tauri star RW Aur A', *IBVS* **6143**, 1.

Shu, F., Najita, J., Ostriker, E., Wilkin, F., Ruden, S. & Lizano, S. (1994), 'Magnetocentrifugally driven flows from young stars and disks. 1: A generalized model', *The Astrophysical Journal* **429**, 781–796.

Smith, M., Alves, J. & McCaughrean, M. (2002), 'The Origins of Stars and Planets: The VLT view', *Alves & M. McCaughrean (ed.)* .

Stumpff, P. (1985), 'Rigorous treatment of the heliocentric motion of stars', *Astronomy and Astrophysics* **144**, 232–240.

Tafalla, M., Myers, P., Mardones, D. & Bachiller, R. (2000), 'L483: a protostar in transition from Class 0 to Class I', *arXiv preprint astro-ph/0005525* .

Takami, M., Beck, T. L., Schneider, P. C., Günther, H. M., White, M., Grankin, K., Karr, J. L., Ohyama, Y., Coffey, D., Liu, H. B. et al. (2020), 'Possible time correlation between jet ejection and mass accretion for RW Aur a', *The Astrophysical Journal* **901**(1), 24.

Telleschi, A., Güdel, M., Briggs, K. R., Audard, M. & Palla, F. (2007), 'X-ray emission from T Tauri stars and the role of accretion: inferences from the XMM-Newton extended survey of the Taurus molecular cloud', *Astronomy & Astrophysics* **468**(2), 425–442.

Tobin, J. J., Looney, L. W., Wilner, D. J., Kwon, W., Chandler, C. J., Bourke, T. L., Loinard, L., Chiang, H.-F., Schnee, S. & Chen, X. (2015), 'A sub-arcsecond survey toward Class 0 protostars in Perseus: Searching for signatures of protostellar disks', *The Astrophysical Journal* **805**(2), 125.

Vacca, W. D. & Sandell, G. (2011), 'Near-infrared spectroscopy of TW Hya: a revised spectral type and comparison with magnetospheric accretion models', *The Astrophysical Journal* **732**(1), 8.

Valenti, J. A., Basri, G. & Johns, C. M. (1993), 'T Tauri stars in blue', *The Astronomical Journal* **106**, 2024–2050.

Vernet, J., Dekker, H., d'Odorico, S., Kaper, L., Kjaergaard, P., Hammer, F., Randich, S., Zerbi, F., Groot, P., Hjorth, J. et al. (2011), 'X-Shooter, the new wide band intermediate resolution spectrograph at the ESO Very Large Telescope', *Astronomy & Astrophysics* **536**, A105.

Virtanen, P., Gommers, R., Oliphant, T. E., Haberland, M., Reddy, T., Cournapeau, D., Burovski, E., Peterson, P., Weckesser, W., Bright, J., van der Walt, S. J., Brett, M., Wilson, J., Millman, K. J., Mayorov, N., Nelson, A. R. J., Jones, E., Kern, R., Larson, E., Carey, C. J., Polat, İ., Feng, Y., Moore, E. W., VanderPlas, J., Laxalde, D., Perktold, J., Cimrman, R., Henriksen, I., Quintero, E. A., Harris, C. R., Archibald,

A. M., Ribeiro, A. H., Pedregosa, F., van Mulbregt, P. & SciPy 1.0 Contributors (2020), 'SciPy 1.0: Fundamental Algorithms for Scientific Computing in Python', *Nature Methods* **17**, 261–272.

Weitzel, L., Krabbe, A., Kroker, H., Thatte, N., Tacconi-Garman, L., Cameron, M. & Genzel, R. (1996), '3D: The next generation near-infrared imaging spectrometer', *Astronomy and Astrophysics Supplement Series* **119**(3), 531–546.

Whelan, E. (2014), 'Jets from young stars and brown dwarfs', *Astronomische Nachrichten* **335**(5), 537–542.

Whelan, E., Bonito, R., Antoniucci, S., Alcalá, J., Giannini, T., Nisini, B., Bacciotti, F., Podio, L., Stelzer, B. & Comerón, F. (2014), 'ESO-Hα 574 and Par-Lup 3-4 jets: Exploring the spectral, kinematical, and physical properties', *Astronomy & Astrophysics* **565**, A80.

Whelan, E., Huélamo, N., Alcalá, J., Lillo-Box, J., Bouy, H., Barrado, D., Bouvier, J. & Merín, B. (2015), 'Spectro-astrometry of LkCa 15 with X-Shooter: Searching for emission from LkCa 15b', *Astronomy & Astrophysics* **579**, A48.

Whelan, E., Pascucci, I., Gorti, U., Edwards, S., Alexander, R., Sterzik, M. & Melo, C. (2021), 'Evidence for an MHD Disk Wind via Optical Forbidden Line Spectroastrometry', *The Astrophysical Journal* **913**(1), 43.

Whelan, E. T., Ray, T. & Davis, C. (2004), 'Paschen beta emission as a tracer of outflow activity from T-Tauri stars, as compared to optical forbidden emission', *Astronomy & Astrophysics* **417**(1), 247–261.

White, R. & Ghez, A. (2001), 'Observational constraints on the formation and evolution of binary stars', *The Astrophysical Journal* **556**(1), 265.

White, R. J. & Hillenbrand, L. A. (2004), 'On the evolutionary status of Class I stars and Herbig-Haro energy sources in Taurus-Auriga', *The Astrophysical Journal* **616**(2), 998.

Wilking, B., Schwartz, R., Mundy, L. & Schultz, A. (1990), 'Shocked molecular hydrogen emission from Herbig-Haro objects and their exciting stars', *The Astronomical Journal* **99**, 344–352.

Woitas, J., Bacciotti, F., Ray, T. P., Marconi, A., Coffey, D. & Eislöffel, J. (2005), 'Jet rotation: Launching region, angular momentum balance and magnetic properties in the bipolar outflow from RW Aur', *Astronomy & Astrophysics* **432**(1), 149–160.

Woitas, J., Leinert, C. & Köhler, R. (2001), 'Mass ratios of the components in T Tauri binary systems and implications for multiple star formation', *Astronomy & Astrophysics* **376**(3), 982–996.

Woitas, J., Ray, T. P., Bacciotti, F., Davis, C. J. & Eislöffel, J. (2002), 'Hubble Space Telescope imaging spectrograph observations of the bipolar jet from RW Aurigae: tracing outflow asymmetries close to the source', *The Astrophysical Journal* **580**(1), 336.

Youngblood, A., France, K., Ginsburg, A., Hoadley, K. & Bally, J. (2018), 'The Orion Fingers: H2 temperatures and excitation in an explosive outflow', *The Astrophysical Journal* **857**(1), 7.